Fuel cell electrocatalsis : oxygen reduction on Pt-based nanoparticle catalysts

Vliet, D.F. van der

Fuel Cell Electrocatalysis

Oxygen Reduction on Pt-based Nanoparticle Catalysts

Proefschrift

ter verkrijging van
de graad van Doctor aan de Universiteit Leiden,
op gezag van Rector Magnificus Prof. Mr. P.F. van der Heijden,
volgens besluit van het College voor Promoties
te verdedigen op dinsdag 21 september 2010
klokke 16.15 Uur

door

Dennis Franciscus van der Vliet

geboren te Tilburg in 1981

Promotiecommissie:

Promotor:	Prof. Dr. M. T. M. Koper
Copromotor:	Dr. N. M. Markovič (Argonne National Lab, USA)
Overige Leden:	Prof. Dr. J. Brouwer
	Prof. Dr. B. E. Nieuwenhuys
	Prof. Dr. J. W. N. Frenken
	Prof. Dr. G. A. Attard (University of Cardiff, UK)
	Prof. Dr. J. A. R. van Veen (Shell)
	Dr. N. P. Lebedeva (ECN)

Table of Contents

Preface

This thesis was prepared in cooperation between Argonne National Laboratory (ANL) and Leiden University. The density functional theory calculations set forth in this thesis were performed by Jeff Greeley at the center for nanoscale materials at ANL and the Monte Carlo simulations were performed by Guofeng Wang at Indiana University-Purdue University.

The synthesis of the nanoparticles as described in chapters 3-5 was performed by Dr. Chao Wang at ANL

Chapter 1

Introduction

In this chapter a short introduction on Fuel cells will be given, starting with their history, continuing with their applications and finishing with the challenges. The aims of the thesis will be presented within this framework of challenges and opportunities.

1.1 History of Fuel Cells

For the past decade, oil prices have been climbing to incredible heights. The cost of petrol at the pump is, for most people, the most noticeable manifestation of the price we pay for our energy. When necessities get more expensive it usually sparks interest in alternative ways to obtain the same goal; in this case it renewed the interest in alternative energy conversion devices, such as fuel cells. [1]
Fuel cells were a direct result of the discovery of water electrolysis in 1789 by Adriaan Paets van Troostwijk and Jan Rudolph Deiman. The discovery of the fuel cell itself is usually attributed to Schönbein or Grove, depending on which reference one consults [2]. Regardless of to whom the actual invention can be ascribed to, their discoveries were published months after one another, which means that 1839 is the year in which the concept of the fuel cell was first published. Over the years interest in fuel cells has waned, especially due to the emergence of fossil fuels and the combustion engine. Starting with the oil crises in the 1970's, interest in fuel cells has increased again in recent years. Initially, fuel cells were especially of interest for situations where normal combustion engines (or, in a previous era, steam engines) could not operate, or remote areas which were not connected to the power grid [2; 3]. This includes submarine and space applications. In the last few decades, automotive applications for the general public have become attractive both for consumers to have an alternative to ever-increasing gas prices, and for governments to reduce carbon emissions and dependence on oil [4]. There is a preferred type of fuel cell for each application, with the Proton Exchange Membrane Fuel Cell (PEMFC) preferred for the use in automotive applications [3; 5]. The higher power density and quick start up due to the lower operating temperature make this fuel cell the first choice for commercial applications such as laptop power and cell phone batteries as well [5]. However, the fuel in these cells will differ depending on the proposed applications. For use in vehicles, hydrogen is preferred, due to its high power-density and higher operating potentials. The difficulty in storing this gas makes it less suitable for smaller applications like the previously mentioned laptops and cell phones. For those applications, liquid fuels such as methanol (direct methanol fuel cell DMFC), formic acid (direct formic acid fuel cell DFAFC) or ethanol (direct ethanol fuel cell DEFC) are preferred. The nomenclature of these fuel cells includes "direct" to stress that the respective fuels are used directly, and not reformed to hydrogen before use in the cell. Finally, for large stationary applications, Solid Oxide Fuel Cells [2; 6] are preferred, both

because they are easier to adapt to existing infrastructure [1] and can operate at higher current densities. [2]

1.2 Working principle of a Fuel Cell

The operation of a fuel cell is in essence very straightforward, see figure 1.1. Fuel (in the figure represented as hydrogen) is oxidized on the anode, separated by an electrolyte from the cathode, at which oxygen is reduced. The electrical current that will flow in the external circuit can then be used for power generation.

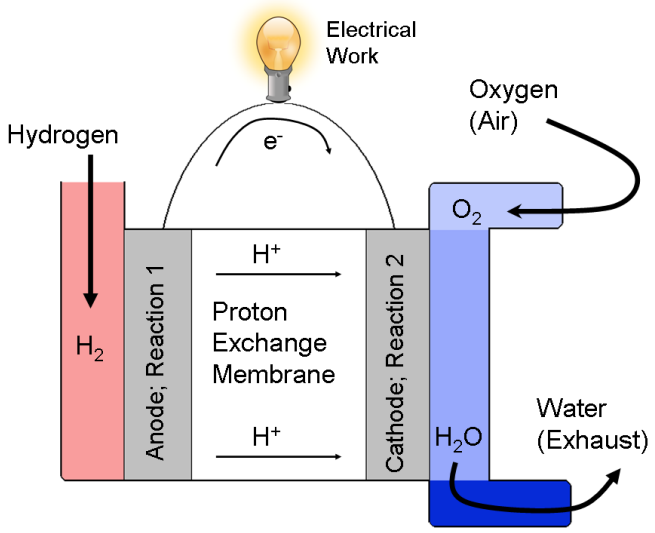

Figure 1.1. Schematic view of a hydrogen-fueled PEM fuel cell in operation.

The basic half-cell reactions for a hydrogen-powered fuel cell are:

$H_2 \leftrightharpoons 2H^+ + 2e^-$	**Reaction 1.1**	$E_0 =$	**0**	**V**
$O_2 + 4H^+ + 4e^- \leftrightharpoons 2H_2O$	**Reaction 1.2**	$E_0 =$	**1.23**	**V**

which combine to give the overall reaction:

$2H_2 + O_2 \leftrightharpoons 2H_2O$	**Reaction 1.3**	$\Delta E_0 =$	**1.23**	**V**

This is, of course, the reverse of water electrolysis.

Reaction 1 is the Hydrogen Oxidation reaction (HOR), which is the reverse of the Hydrogen Evolution Reaction (HER). Both the HOR and the HER have been investigated extensively [7-13], with platinum the most widely used catalyst. [14] The Oxygen Reduction Reaction (ORR) is shown by reaction 2 and has gained significant interest in the past decades as it is currently the efficiency-limiting reaction in a hydrogen-powered fuel cell [15-29]. The equilibrium potential of the HOR at a Pt electrode in the electrolyte is 0V by definition; this is the reversible hydrogen electrode (RHE). The equilibrium potential of the ORR on Pt is at 1.23 V versus the RHE. The pH-independent RHE scale is used throughout this thesis to avoid pH effects on the reference potential.

The difference between the respective equilibrium potentials of the anode (HOR) and cathode (ORR) reactions will be the maximum cell voltage. With multiple of these single cells stacked, the desired power output can be achieved, which is in the order of 100 kW for a fuel cell powered car [30]. The elegance in the operation lies in the absence of greenhouse gas emissions when clean hydrogen is used as fuel (with water as the only product, see figure 1.1 and reaction 1.3), as well as the theoretically high efficiency of a fuel cell [3-5]; gaining the most energy from the fuel. Hydrogen offered commercially at present is often obtained from steam reforming, and has small amounts of carbon monoxide present as contamination. This CO has a negative effect on the performance due to catalyst-poisoning and it will oxidize to CO_2, a greenhouse gas.

There are of course some engineering challenges for fuel cell development as well. The polymer electrolyte membrane has to be improved to reduce resistance and reactant crossover. [16; 31] The crossover current density originates from fuel passing unreacted through the membrane to react at the cathode. Reactant crossover is a major problem as it effectively short-circuits the cell (since Pt is active for both the oxidation and reduction reactions of the cell), reducing efficiency. Furthermore, in case of a DMFC, methanol crossover will poison the cathode. [32-35] Electrolyte resistance, due to the polymer membrane and ionomer content [16; 36], is usually compensated for in membrane electrode assemblies (MEAs) when screening for catalyst activity to verify that the effect observed is due to the catalyst and not to the resistance in the stack. In the operational fuel cell stack, however, resistances must be kept to a minimum, to avoid cell output losses due to resistance. [16; 37] A second problem lies in the carbon that is generally used to support the nanoparticles. The carbon support also causes resistance in a fuel cell [38-40], and particles supported on it are known to dissolute from the catalyst layer [40-42] or sinter into bigger particles, thereby losing their unique properties. [40; 43] One way

to avoid this trouble it to manufacture high surface area catalysts that do not rely on carbon supports, such as has been published by 3M [17; 43-45].

1.3 Towards better Fuel Cells

Pt and Pt alloys are currently the best catalysts for the ORR, but even with the best state-of-the-art catalysts there is still a large overpotential, which reduces the total fuel cell output. The overpotential is the potential difference between a thermodynamically determined equilibrium potential of a half reaction and the potential at which this half-reaction is experimentally observed. [46] The overpotential (η) for the ORR in fuel cell systems can be modeled by a Tafel-relation: $\eta = (70\ mV / decade) \cdot \log(i_{eff})$, where i_{eff} is the effective current density, defined by $i_{eff} = i + i_{crossover}$. [16] The cell loss due to the overpotential for the ORR is limiting the fuel cell efficiency, causing fuel cell stacks to require more individual cells to have the desired power output. With the most active catalyst being Pt, this means a fuel cell stack will become very expensive. One strategy to improve this situation is to find better catalysts, hereby reducing the platinum content in the catalyst, for example by alloying Pt with a second (or multiple) metal. [16; 18; 19; 47-54] Another option is to make better use of the platinum. With the surface of the metal active for catalysis, increasing the surface area to bulk ratio will increase the usage of Pt. Nanoparticles dispersed on high surface area carbon are therefore widely tested. [55-62] Finally, non-precious metal catalysts are of interest to eliminate the platinum availability and cost problem altogether. [18] An order of magnitude increase in the activity versus state-of-the-art carbon-supported nanoparticulate ORR catalysts, and an approximately 5-fold reduction in Pt content is required to meet the cost requirements for large scale automotive applications [51].

1.4 Outline of this thesis

Work for this thesis started at Argonne National Laboratory, in the group of Dr. Markovic, which specializes in oxygen reduction. Chapters 3 through 8 have been prepared there, while experiments for chapter 2 were also performed at Argonne. In

the final year, the preparation of chapters 2, 6 and 7, experiments for chapter 8 as well as the assembling of this thesis has been performed at Leiden University.

The testing of catalysts in the actual assembled fuel cell is a time-consuming process [63-65]; therefore bench-top lab testing has been developed by means of the Rotating Disc Electrode in an electrochemical cell. This method, first developed by Schmidt *et al.* [64], is used in this thesis in Chapters 3-7 for nanoparticle electrochemistry. To summarize the process, the catalyst particles are first suspended in water, and then pipetted onto a conductive glassy carbon (GC) disc, which then can be used in the RDE. An added advantage of this setup is that a single half-reaction can be studied in detail, rather than the fuel cell as a whole.

Identical to MEAs, solution resistance will also play a role in measurements in an electrochemical cell, as will be discussed in chapter 2. This chapter also deals with adsorption processes, which are present during the reduction of oxygen in the RDE method. This leads to a superposition of the current due to these adsorption processes on the measured ORR curve. In chapter 2 suggestions for proper compensation for these two RDE-related issues will be given.

In order to contribute to meeting the challenges set out in section 1.3, novel nanoparticulate electrocatalysts were synthesized and measured for their activity towards oxygen reduction. These efforts are illustrated in chapters 3 and 4, where the effects of preparation method and pretreatment on particle size, distribution and segregation profile are shown for solvothermally synthesized Pt_3Co nanoparticles. The Pt_3Co alloy was chosen as this alloy is shown to have increased activity for the ORR in the bulk polycristalline material. [66]

Furthermore, a novel gold core-Pt_3Fe shell catalyst was synthesized in an effort to diminish particle agglomeration, which is discussed in chapter 5. This catalyst has proven to have both increased activity and stability, setting up a way forward to meeting the objectives set out by the United States Department of Energy (DOE) [17].

The nanostructured thin film (NSTF) catalysts from 3M, mentioned before in section 1.2, have shown increased activity and stability for the ORR, and will feature in chapters 6 and 7 of this thesis. The original NSTF, as received from 3M, is a high surface area Pt-based catalyst, which is not supported on carbon. Because it is not carbon-supported, the NSTF catalyst has an increased stability when compared to supported nanocatalysts. [67] In chapter 6, proper catalyst loadings and preparations are determined and a range of NSTFs are measured. From these experiments, PtNi NSTF emerged as the most active catalyst for the ORR. A

pretreatment method, which increases both the specific and mass activity of this catalyst, will be discussed in chapter 7.

Due to the fact that the ORR is active at higher potentials in alkaline media than in acid media, alkaline electrolytes are of interest. [68-70] This shows itself in both fuel cells with Alkaline Anion Exchange Membranes (AAEMs) [67; 71; 72] and RDE experiments in alkaline electrolyte. [73] Combining the interest in alkaline media with the finding of chapter 7, where it was shown that the pretreatment method of a catalyst is of importance, chapter 8 deals with the influence of the preparation method on the surface state and electrochemical behavior of Pt (100) in alkaline media. It is shown that the pretreatment has a significant impact on the catalytic activity of the surface. Likewise, the alkali-metal cations, as well as adsorbing anions are shown to have a significant influence on the catalysis by Pt(100).

References

[1] J.W. Gosselink, International Journal of Hydrogen Energy 27 (2002) 1125-1129.

[2] J.M. Andujar, F. Segura, Renewable & Sustainable Energy Reviews 13 (2009) 2309-2322.

[3] H.J. Neef, Energy 34 (2009) 327-333.

[4] W. Vielstich, A. Lamm, H.A. Gasteiger (Eds.), Handbook of Fuel Cells: Fundamentals, Technology, Applications, Wiley, 2003.

[5] A. Kirubakaran, S. Jain, R.K. Nema, Renewable & Sustainable Energy Reviews 13 (2009) 2430-2440.

[6] J. Malzbender, R.W. Steinbrech, L. Singheiser, Fuel Cells 9 (2009) 785-793.

[7] D. Strmcnik, D. Tripkovic, D. van der Vliet, V. Stamenkovic, N.M. Markovic, Electrochemistry Communications 10 (2008) 1602-1605.

[8] B.E. Conway, B.V. Tilak, Electrochimica Acta 47 (2002) 3571-3594.

[9] K. Domke, E. Herrero, A. Rodes, J.M. Feliu, Journal of Electroanalytical Chemistry 552 (2003) 115-128.

[10] S.L. Chen, A. Kucernak, Journal of Physical Chemistry B 108 (2004) 13984-13994.

[11] N.M. Markovic, S.T. Sarraf, H.A. Gasteiger, P.N. Ross, Journal of the Chemical Society-Faraday Transactions 92 (1996) 3719-3725.

[12] N.M. Markovic, B.N. Grgur, P.N. Ross, Journal of Physical Chemistry B 101 (1997) 5405-5413.

[13] A.F. Innocente, A.C.D. Angelo, Journal of Power Sources 162 (2006) 151-159.

[14] H.A. Gasteiger, N.M. Markovic, P.N. Ross, Journal of Physical Chemistry 99 (1995) 8290-8301.

[15] V.R. Stamenkovic, B. Fowler, B.S. Mun, G.F. Wang, P.N. Ross, C.A. Lucas, N.M. Markovic, Science 315 (2007) 493-497.

[16] H.A. Gasteiger, M.F. Mathias, in: M. Murthy, T.F. Fuller, J.W. Van Zee, S. Gottesfeld (Eds.), Proton conducting membrane fuel cells III: proceedings of The Electrochemical Society, Pennington, New Jersey, 2005, pp. 1-24.
[17] K.E. Martin, J.P. Kopasz, M. K.W., in, Fuel Cell Chemistry and Operation, Chapter 1, 2010, pp. 1-13.
[18] H.A. Gasteiger, S.S. Kocha, B. Sompalli, F.T. Wagner, Applied Catalysis B-Environmental 56 (2005) 9-35.
[19] H.A. Gasteiger, J.E. Panels, S.G. Yan, Journal of Power Sources 127 (2004) 162-171.
[20] K.J.J. Mayrhofer, B.B. Blizanac, M. Arenz, V.R. Stamenkovic, P.N. Ross, N.M. Markovic, Journal of Physical Chemistry B 109 (2005) 14433-14440.
[21] J.X. Wang, N.M. Markovic, R.R. Adzic, Journal of Physical Chemistry B 108 (2004) 4127-4133.
[22] L. Xiao, L. Zhuang, Y. Liu, J.T. Lu, H.D. Abruna, Journal of the American Chemical Society 131 (2009) 602-608.
[23] J. Hernandez, J. Solla-Gullon, E. Herrero, A. Aldaz, J.M. Feliu, Journal of Physical Chemistry C 111 (2007) 14078-14083.
[24] L.G.R.A. Santos, K.S. Freitas, E.A. Ticianelli, Electrochimica Acta 54 (2009) 5246-5251.
[25] A.S. Arico, P. Bruce, B. Scrosati, J.M. Tarascon, W. Van Schalkwijk, Nature Materials 4 (2005) 366-377.
[26] A. Atkinson, S. Barnett, R.J. Gorte, J.T.S. Irvine, A.J. Mcevoy, M. Mogensen, S.C. Singhal, J. Vohs, Nature Materials 3 (2004) 17-27.
[27] P. Strasser, *et al.*, Nature Chemistry Published online: 25 April 2010 | doi:10.1038/nchem.623 (2010).
[28] K.J.J. Mayrhofer, M. Arenz, Nature Chemistry 1 (2009) 518-519.
[29] J. Greeley, I.E.L. Stephens, A.S. Bondarenko, T.P. Johansson, H.A. Hansen, T.F. Jaramillo, J. Rossmeisl, I. Chorkendorff, J.K. Norskov, Nature Chemistry 1 (2009) 552-556.
[30] Honda, Honda FCX Clarity Specifications, http://world.honda.com/FCXClarity/specifications/index.html, 2010.
[31] S.A. Vilekar, R. Datta, Journal of Power Sources 195 (2010) 2241-2247.
[32] K. Scott, W.M. Taama, P. Argyropoulos, K. Sundmacher, Journal of Power Sources 83 (1999) 204-216.
[33] C.Y. Du, T.S. Zhao, W.W. Yang, Electrochimica Acta 52 (2007) 5266-5271.
[34] S. Hikita, K. Yamane, Y. Nakajima, Jsae Review 22 (2001) 151-156.
[35] S. Hikita, K. Yamane, Y. Nakajima, Jsae Review 23 (2002) 133-135.
[36] K.H. Kim, K.Y. Lee, H.J. Kim, E. Cho, S.Y. Lee, T.H. Lim, S.P. Yoon, I.C. Hwang, J.H. Jang, International Journal of Hydrogen Energy 35 (2010) 2119-2126.
[37] S.S. Zhang, X.Z. Yuan, H.J. Wang, W. Merida, H. Zhu, J. Shen, S.H. Wu, J.J. Zhang, International Journal of Hydrogen Energy 34 (2009) 388-404.
[38] V. Komanicky, K.C. Chang, A. Menzel, N.M. Markovic, H. You, X. Wang, D. Myers, Journal of the Electrochemical Society 153 (2006) B446-B451.
[39] Y.Y. Shao, J. Wang, R. Kou, M. Engelhard, J. Liu, Y. Wang, Y.H. Lin, Electrochimica Acta 54 (2009) 3109-3114.
[40] S.S. Zhang, X.Z. Yuan, J.N.C. Hin, H.J. Wang, K.A. Friedrich, M. Schulze, Journal of Power Sources 194 (2009) 588-600.
[41] K. Kinoshita, J. Lundquist, P. Stonehart, Journal of Electroanalytical Chemistry 48 (1973) 157-166.

[42] K.J.J. Mayrhofer, S.J. Ashton, J.C. Meier, G.K.H. Wiberg, M. Hanzlik, M. Arenz, Journal of Power Sources 185 (2008) 734-739.
[43] M.K. Debe, A.K. Schmoeckel, G.D. Vernstrorn, R. Atanasoski, Journal of Power Sources 161 (2006) 1002-1011.
[44] M.K. Debe, A.R. Drube, Journal of Vacuum Science & Technology B 13 (1995) 1236-1241.
[45] M.K. Debe, R.J. Poirier, Journal of Vacuum Science & Technology a-Vacuum Surfaces and Films 12 (1994) 2017-2022.
[46] A.J. Bard, L.R. Faulkner, Electrochemical Methods, New York, J. Wiley & Sons, 1980.
[47] F.J. Lai, L.S. Sarma, H.L. Chou, D.G. Liu, C.A. Hsieh, J.F. Lee, B.J. Hwang, Journal of Physical Chemistry C 113 (2009) 12674-12681.
[48] P. Mani, R. Srivastava, P. Strasser, Journal of Physical Chemistry C 112 (2008) 2770-2778.
[49] Y. Tamura, K. Taneda, M. Ueda, T. Ohtsuka, Corrosion Science 51 (2009) 1560-1564.
[50] F.H.B. Lima, J.F.R. de Castro, L.G.R.A. Santos, E.A. Ticianelli, Journal of Power Sources 190 (2009) 293-300.
[51] K.J.J. Mayrhofer, D. Strmcnik, B.B. Blizanac, V. Stamenkovic, M. Arenz, N.M. Markovic, Electrochimica Acta 53 (2008) 3181-3188.
[52] S. Mukerjee, S. Srinivasan, M.P. Soriaga, J. Mcbreen, Journal of the Electrochemical Society 142 (1995) 1409-1422.
[53] S. Mukerjee, S. Srinivasan, M.P. Soriaga, J. Mcbreen, Journal of Physical Chemistry 99 (1995) 4577-4589.
[54] U.A. Paulus, A. Wokaun, G.G. Scherer, T.J. Schmidt, V. Stamenkovic, V. Radmilovic, N.M. Markovic, P.N. Ross, Journal of Physical Chemistry B 106 (2002) 4181-4191.
[55] D. Susac, A. Sode, L. Zhu, P.C. Wong, M. Teo, D. Bizzotto, K.A.R. Mitchell, R.R. Parsons, S.A. Campbell, Journal of Physical Chemistry B 110 (2006) 10762-10770.
[56] D. Susac, L. Zhu, M. Teo, A. Sode, K.C. Wong, P.C. Wong, R.R. Parsons, D. Bizzotto, K.A.R. Mitchell, S.A. Campbell, Journal of Physical Chemistry C 111 (2007) 18715-18723.
[57] S. Gupta, D. Tryk, I. Bae, W. Aldred, E. Yeager, Journal of Applied Electrochemistry 19 (1989) 19-27.
[58] S.L. Gupta, D. Tryk, W. Aldred, I.T. Bae, E. Yeager, Journal of the Electrochemical Society 134 (1987) C129-C129.
[59] M. Lefevre, E. Proietti, F. Jaouen, J.P. Dodelet, Science 324 (2009) 71-74.
[60] F. Jaouen, *et al.*, Acs Applied Materials & Interfaces 1 (2009) 1623-1639.
[61] R. Kothandaraman, V. Nallathambi, K. Artyushkova, S.C. Barton, Applied Catalysis B-Environmental 92 (2009) 209-216.
[62] K. Kendall, Nature Materials 1 (2002) 211-212.
[63] F. Gloaguen, F. Andolfatto, R. Durand, P. Ozil, Journal of Applied Electrochemistry 24 (1994) 863-869.
[64] T.J. Schmidt, M. Noeske, H.A. Gasteiger, R.J. Behm, P. Britz, H. Bonnemann, Journal of the Electrochemical Society 145 (1998) 925-931.
[65] T.J. Schmidt, N.M. Markovic, V. Stamenkovic, P.N. Ross, G.A. Attard, D.J. Watson, Langmuir 18 (2002) 6969-6975.

[66] V.R. Stamenkovic, B.S. Mun, M. Arenz, K.J.J. Mayrhofer, C.A. Lucas, G.F. Wang, P.N. Ross, N.M. Markovic, Nature Materials 6 (2007) 241-247.
[67] T.J. Schmidt, V. Stamenkovic, M. Arenz, N.M. Markovic, P.N. Ross, Electrochimica Acta 47 (2002) 3765-3776.
[68] S.D. Poynton, J.P. Kizewski, R.C.T. Slade, J.R. Varcoe, Solid State Ionics 181 (2010) 219-222.
[69] J.R. Varcoe, J.P. Kizewski, D.M. Halepoto, S.D. Poynton, R.C.T. Slade, F. Zhao, in, Encyclopedia of Electrochemical Power Sources, Amsterdam, 2009, pp. 329-343.
[70] E. Agel, J. Bouet, J.F. Fauvarque, Journal of Power Sources 105 (2002) 87-87.
[71] L. Genies, R. Faure, R. Durand, Electrochimica Acta 44 (1998) 1317-1327.
[72] L.H. Jiang, A. Hsu, D. Chu, R.R. Chen, Journal of Electroanalytical Chemistry 629 (2009) 87-93.
[73] W. Jin, H. Du, S.L. Zheng, H.B. Xu, Y. Zhang, Journal of Physical Chemistry B 114 (2010) 6542-6548.

Chapter 2

On the Importance of Correcting for the Uncompensated Ohmic Resistance in Model Experiments of the Oxygen Reduction Reaction

When measuring the current due to the oxygen reduction reaction (ORR) and hydrogen oxidation reaction (HOR) on Pt and Pt alloys in aqueous electrolyte, it is important to take care of two major sources of error that are relatively easy to correct for. First, when measuring ORR voltammetry, adsorption processes are superimposed on the current. Second, the system resistance causes an Ohmic drop that may have a profound effect on the measured curves, especially at the higher currents close to the diffusion limiting current. More importantly, we show that it also influences the kinetic part of the potential curve in such a way that the Tafel slope may be determined incorrectly when failing to correct for Ohmic drop. Finally, because electrolyte resistance lowers with increasing temperature, failure to compensate for Ohmic drop may lead to erroneous conclusions about the temperature-dependent activity of a catalyst as well as the corresponding activation energies.

The contents of this chapter have been published: D. van der Vliet, D.S. Strmcnik, C. Wang, V.R. Stamenkovic, N.M. Markovic and M.T.M. Koper, *J. Electroanal. Chem. 647* **(2010)** 29

2.1 Introduction

With development of renewable energy and cleaner transportation high on the world's priority list, significant amount of work has been invested in the development of low-temperature polymer electrolyte fuel cells [1]. In order to find better catalysts for these cells, various groups are using the Rotating Disk Electrode (RDE) method to investigate Hydrogen Oxidation (HOR) [2] and Oxygen Reduction (ORR) reactions [3-8], as rotating disk electrodes allow control of the contribution of diffusion limitation to the current [9]. In order to compare the RDE measurements with actual membrane electrode assembly (MEA) fuel cell stack testing, one needs to be aware of all effects that can influence RDE results. This includes the effect of active surface area determination, as explained in [10], adsorbing anions, capacitive currents and solution resistance. In MEA tests it is common practice to compensate the measured ORR activity for IR-drop, but in model RDE experiments it is usually assumed that the electrolyte is sufficiently conductive, and that the currents measured are low enough, to make the contribution of solution resistance negligible.

The effect of the cell geometry on the uncompensated Ohmic drop due to solution resistance has been studied extensively in the past. (See [11-27] and references therein) It is clear from these reports that the geometry and placing of the Luggin-Haber capillary [28] is crucial in reducing measurement errors due to the inhomogeneous current density distribution, Ohmic resistance and shielding of the electrode by the capillary. Since Haber's introduction of the Luggin-Haber capillary, it is well known that the capillary introduces a small, often negligible, Ohmic drop [28]. The classic work of Pontarelli et al [14-17] focuses on the capillary's geometry and placing. They derived that the optimal position of the capillary is through the middle of the electrode from behind [14], but that location is impractical in current cell designs, especially those for single crystal work and rotating disk electrodes. As a good alternative they suggested a closed-top capillary pressed firmly to the electrode, with a tiny opening to the side close to the electrode [14, 15]. Again, this geometry is impractical in RDE experiments, due to the friction it would generate between disk and capillary. This geometry may also disturb diffusion and flow patterns, shielding part of the electrode. Barnartt describes in detail the open Luggin-Haber capillary placed in front of the electrode, at a preferred distance of at least 4 times the capillaries' radius, provided

corrections are made for IR-drop in case of low conductivity or high current densities [18]. This also implies that, ideally, the outer diameter of the capillary is as thin as possible, as wide capillaries are useful only at relatively low current densities in solutions of high conductivity [19]. Furthermore, he notes that in situations of forced convection (such as with a RDE) the capillary tip may alter the hydrodynamic flow. J.E.Harrar et al determined that the optimal position of the capillary is on the line of minimum separation between working and counter electrodes [12].

In this communication, we will show that under rather standard conditions using a popular commercial RDE setup, failure to correct for the Ohmic resistance can impact substantially on the interpretation of kinetic measurements of the ORR. In rotating ring-disk electrodes (RRDE) there will also be an effect of coupling of the potential fields of ring and disk [29], where the individual potential fields of disk and ring are superpositioned thereby causing a coupling resistance. Only disc electrodes were used in this work, so the potential field coupling could not be verified, and will not be further discussed; the interested reader is referred to the detailed work of Dörfel *et al.* [29].

2.2 Experimental

All measurements were performed in $HClO_4$ solutions, prepared by diluting concentrated perchloric acid (70%, JT Baker Ultrex II) with ultrapure water (Milli-Q gradient; 18.2 MΩ resistivity; 4 ppb total oxidisable carbon) to obtain the desired concentration. Concentrations used are 0.1M, 0.5M and 1.0M $HClO_4$. The potentiostat used was a computer-controlled Autolab PGSTAT 30 with ECD, Scan Gen, FI20 and FRA (impedance) modules. The electrode assembly consisted of a Pine AFASR rotator with matching Pine electrode shaft. The electrode tips are custom made with disk inserts of Pt and Glassy Carbon of 6 mm diameter. GC disks were polished (Buehler microcloth) to a shiny finish with 0.05µm as finishing polish prior to depositing nanocatalysts.

The 5 nm Pt/C (supplied by TKK, Tokyo, Japan) is deposited by depositing a drop of a sonicated, catalyst-containing suspension onto the GC disk assembled in the collet. In a slow Ar-flow (Airgas, UHP 99.995%) the drop of water is allowed to evaporate, leaving the catalyst deposited on the GC disk. The suspension is made in such a way that 22 µl of the suspension deposited on a 6 mm GC disk gives a

loading of 18 μg_{Pt} cm_{disk}^{-2}. Polycrystalline Pt disks are annealed by inductive heating before insertion in the collet. The induction heater setup was used to anneal the crystal for 10 minutes at ~1900 K in an Ar/H_2 atmosphere (Linde Gas, 4.82% hydrogen, high purity).

All cells are of in-house design. A salt bridge connects the main compartment of the cell through the Luggin-Haber Capillary with the reference electrode. A Ag/AgCl reference was used for all experiments; the potentials in this paper are all reported versus the reversible hydrogen electrode (RHE). The position of the Luggin-Haber capillary, with an outer diameter of 2 mm, is as close to the working electrode as possible without generating a shielding effect. This shielding effect appears when the capillary is placed closer to the electrode than 2 times the capillary's outer diameter [18], but for practical purposes can be assumed minor until the distance approaches 1 time the outer diameter of the capillary [15]. Therefore, in our cell, the distance of the Luggin-Haber capillary to the working electrode was typically on the order of 5 to 10 mm, perpendicular to the exposed surface of the working electrode. This is a common location of the capillary in a standard electrochemical cell used by numerous groups [2, 5, 6, 10, 30-35]. The counter electrode was placed in a separate compartment as well, with the opening to the compartment 1 cm to the side of the Luggin-Haber capillary.

Initial blank cyclic voltammetry was measured with the electrode immersed in deoxygenated electrolyte. (Argon; Airgas, research grade plus; 99.9999%) Prior to measuring the oxygen reduction reaction the cell was saturated with oxygen (Airgas, research grade, 99.999%). ORR measurements are recorded with the electrode rotating at 1600 rpm. IR correction during the measurement was done by positive feedback [13, 24]; i.e. the resistance was determined by impedance at a potential which just exhibited diffusion limiting current for the ORR, and was assumed constant during the measurement. A correction voltage proportional to the current was applied during the measurement. Overcompensation for resistance during the measurement of cyclic voltammetry can be quickly noted as the potential will start to oscillate.

2.3 Results and discussion

2.3.1 IR-Drop

The uncompensated resistance can be determined by measuring the high-frequency impedance at operating conditions. Popkirov reported that the uncompensated

resistance can vary during an experiment [24], and may even become a function of the current, *e.g.* through a passivating intermediate that can temporarily increase electrode resistance[24]. This issue can become important especially when research moves away from noble metals as catalysts [4]. Similarly, the resistance can increase in dilute solutions as the diffusion limiting current is approached, due to depletion of charge carriers [23]. In current ORR research, electrolyte concentration usually is 0.1M or higher, with non-passivating (Pt based) catalysts, so the Ohmic resistance is not expected to change during a measurement.

The insert in figure 2.1A shows the Nyquist plot of an impedance measurement on a Pt disk in our assembly. The mean potential was chosen to be within the diffusion limiting regime for the ORR in an oxygen saturated electrolyte to include any resistance induced by the measurement of the ORR. A potential amplitude of 10 mV was applied with frequencies starting at 10kHz and ending with 1 Hz on a logarithmic scale. The figure shows a vertical plot with a minimum in the imaginary part at 2500 Hz. From the real component value of the impedance at the minimum of the Nyquist plot, the Ohmic resistance of the system can be deduced to be 28.5 Ω., with a possible error of about 0.2 Ω. The value of this resistance is virtually independent of the type of catalyst we use (it deviates by up to 4 Ohm in any given experiment of this kind) and thus is a good representation of a typical value for the solution resistance. Carbon supported nanocatalysts exhibit slightly higher values (an average 34 Ω compared to 28 Ω for polycrystalline Pt) of the resistance due to a small contact resistance in the catalyst layer. Hanging meniscus experiments [34, 35], as generally used for single-crystals, usually have a higher resistance as well due to the longer distance between capillary and electrode. Higher resistance for bead-type single crystals usually does not induce a higher Ohmic drop, unless the surface area of these crystals and the corresponding currents become large, such as with single-crystal disks of 5 [35] mm,6 mm [30, 36] or larger in diameter.

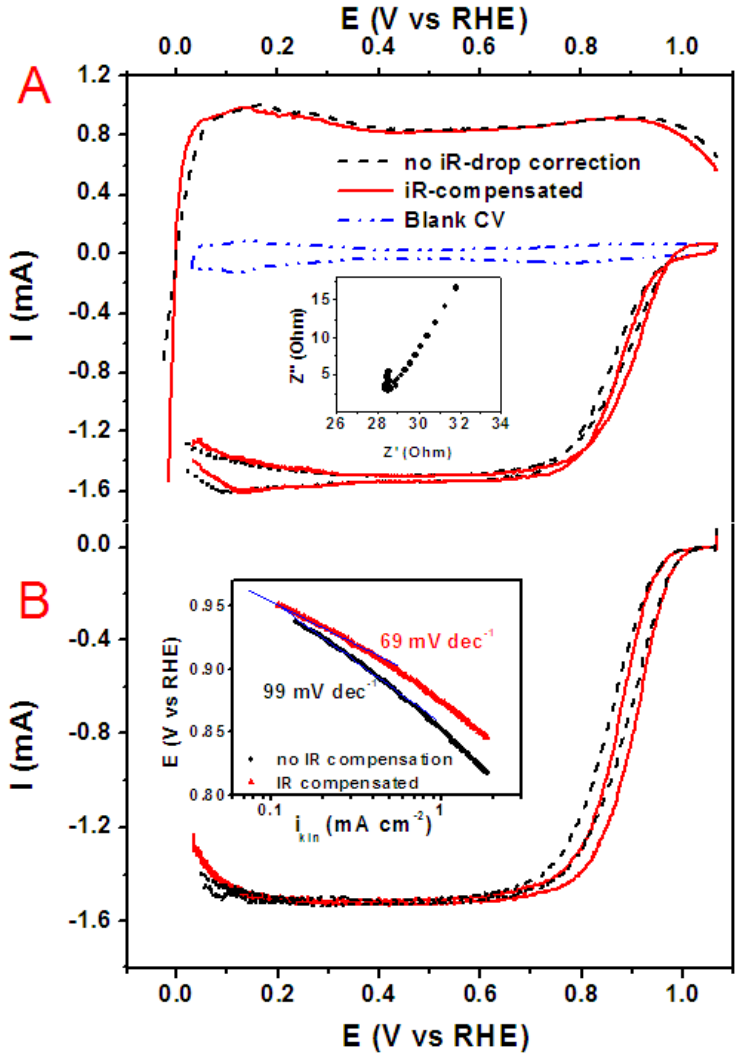

Figure 2.1 A shows the effect of both the resistance and the capacitive currents on the measurement of the HOR and ORR. The black graph shows the measured current as obtained from an experiment without IR drop correction. The red graph shows the current obtained with IR-compensation during the measurement. The blue graph is the blank cyclic voltammogram (no rotation) for this sample. Experimental conditions: Pt/C 5nm, room temperature, 0.1 M $HClO_4$. Scan rate 20 mV s^{-1}, 1600 rpm for HOR and ORR curves; no rotation for the blank CV.The insert shows the impedance measurement at 0.68V vs. RHE in oxygen-saturated 0.1M $HClO_4$ at room temperature. Amplitude 0.01 V. Range 1 Hz through 10kHz in a logarithmic scale. Rotation 1600 rpm.
Part B shows the effect of IR-compensation on the ORR curves corrected for capacitive-current. The insert shows the effect of IR-drop on the measured Tafel slope. Measured in oxygen-saturated 0.1M $HClO_4$ at room temperature with 1600 rpm rotation.

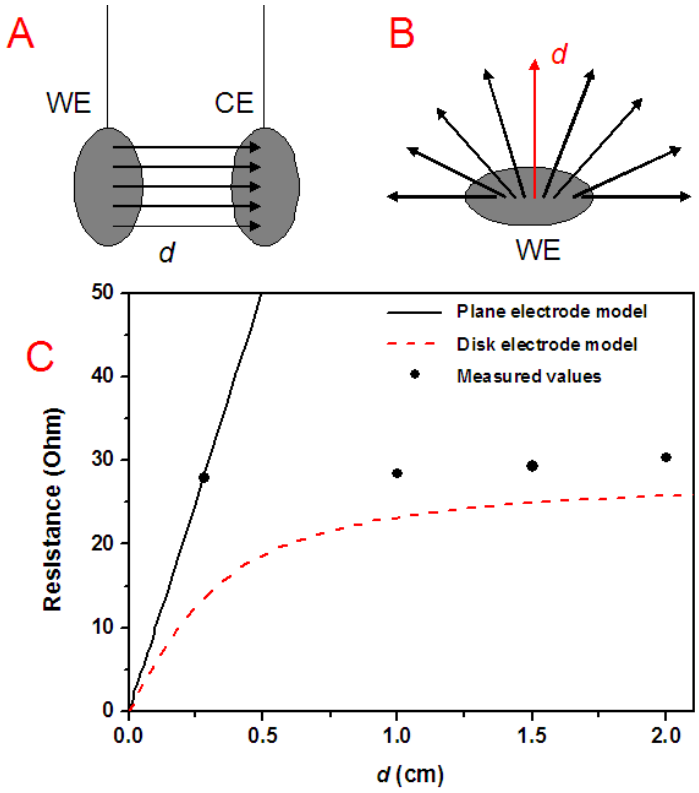

Figure 2.2, A and B show the geometry of the plane electrode model and disk electrode model, respectively. In the plane model the counter electrode is of the same shape and size of the working electrode separated by a finite distance *d*. The diameter of the disk was chosen to be 6 mm; the planar electrodes were calculated with the same surface area as the disk. The disk model of Newman [11] assumes the counter electrode is at infinity. The arrows in both graphs represent the field lines. Part C shows the apparent resistances predicted by both models and the values retrieved from our experiments in 0.1M $HClO_4$, equations are listed in the text.

Solution resistance is caused by a combination of low electrolyte concentration and temperature as well as the distance of the Luggin capillary to the surface of the working electrode. However, even if the capillary is brought close to the disk, we find that a significant Ohmic resistance remains, as illustrated in table 2.1. This effect has been observed and calculated before [11, 15, 37], concluding the potential drop increases rapidly until the capillary is brought to about 0.5 mm from the electrode, after which it remains essentially constant. Newman's model [11] shows clearly that, for a 0.1 M copper sulfate solution, even when the probe of the

reference electrode is only half a millimeter from the surface of the electrode, the resistance is by no means negligible. The electrode and cell geometry cause a spherical distribution of current and potential lines, leading to an increase in the apparent resistance which levels off at large distances, as illustrated in figure 2.2. At infinite distance, Newman's geometry gives a resistance of

$$R = 1/(4a\kappa)$$

where a is the radius of the disk and κ is the electrolyte conductivity. For intermediate distances d, the resistance can be estimated according to the procedure outlined by Newman [11]. From his equations for a three dimensional system, a model equation can be derived where the Luggin capillary is placed exactly in line with the electrode surface:

$$R = (2/\kappa\pi) \tan^{-1} (d / a)$$

Figure 2.2 compares, for a 0.1 M $HClO_4$ solution with an estimated conductivity of κ=0.035 (ohm cm)$^{-1}$,[38] the resistance calculated from Newman's model with the resistance between two equally sized disk electrodes:

$$R = d/(\kappa A)$$

where d is the distance between the electrodes and A is their area. This planar model was chosen to mimic the situation where the counter electrode would be small, and the reference measurement placed directly at this counter electrode. From this figure it can be concluded that Newman's model agrees with our experimental situation remarkably well, especially when compared to the planar electrode model. The higher values obtained from experiments can be explained in several ways, such as slightly lower concentration of the electrolyte, lower actual temperature in the cell, shielding effects by the Luggin-Haber capillary at very short distances, or contact resistances in the disk assembly setup. The reason for the discrepancy between model and experiments at short distances of the Luggin capillary is not known precisely, but is assumed to relate to non-distance related resistances, such as contact resistance. As is illustrated in table 2.1 and 2.2, the uncompensated resistance decreases with both increasing temperature and base electrolyte concentration. However, when the concentration is increased from 0.5 to 1.0 M, this does not seem to affect the measured resistance very much; both values are equal

within their standard deviation. Likely the supporting electrolyte is sufficiently abundant that the reduction in resistance due to increased conductivity is very small compared to the residual uncompensated resistive contributions, the exact origin(s) of which remains somewhat elusive. Still, in a model experiment using electrodes of standard size (6 mm diameter), even at such high concentrations and temperatures the contribution of the Ohmic drop needs to be taken into account because the values of resistance will lead to a significant potential drop at the diffusion limiting current for the ORR. For a 28.5 Ω resistance the half-wave potential measured with diffusion limiting current of 1.6 mA is 23 mV lower than the actual potential on the disk, while for a lower IR-drop of 11 Ω it is still a significant shift of 9 mV. These shifts have to be taken into account since they cause a considerable error in the measurement, as will be shown in the next section.

Table 2.1, dependence of Ohmic resistance as measured with impedance on distance of the Luggin capillary from the surface of the electrode. Standard deviations are listed as errors. Electrolyte used was 0.1M $HClO_4$, impedance spectroscopy was measured at 1600 rpm in oxygen-saturated electrolyte and the solution resistance determined from the minimum in the Nyquist plot.

Distance (mm)	Resistance at 293 K (Ω)	Resistance at 330K (Ω)
2	28.1 ± 1.0	15.5 ± 0.8
10	28.5 ± 0.2	16.5 ± 0.2
15	29.4 ± 0.2	18.4 ± 0.3
20	30.4 ± 0.8	

Table 2.2, Resistance measured in Impedance measurements for different concentrations of electrolyte. Standard deviations are listed as errors. Impedance spectroscopy was measured at 1600 rpm in oxygen-saturated electrolyte and the solution resistance determined from the minimum in the Nyquist plot.

Concentration $HClO_4$ (M)	Resistance at 293 K (Ω)	Resistance at 330K (Ω)
0.1	28.5 ± 0.2	16.5 ± 0.2
0.5	11 ± 1.0	5.5 ± 0.6
1	11.5 ± 1.2	7.0 ± 1.3

2.3.2 Consequences on data interpretation

2.3.2.1 Influence of adsorption processes

The first source of error in determining the activity of a high surface area catalyst for the Oxygen Reduction Reaction (ORR) comes from the current due to adsorption processes at the electrode. Underpotential deposited hydrogen (H_{upd}) and oxide formation processes are taking place during the measurement of the ORR and their current contributions are superimposed on the ORR curve [39]. This is illustrated in figure 2.1A. The figure shows the curve for a high surface area Pt/C-catalyst, deposited on Glassy Carbon (GC) in black, as measured in an oxygen-saturated solution at 1600 rpm with a scan rate of 20 millivolts per second. Also shown in this graph, in blue, is the blank cyclic voltammetry of this sample. The H_{upd} features at potentials lower than 0.4 V are clearly visible in the ORR curve. The oxide plateau at potentials higher than 0.8 V is less obvious, but the oxide reduction peak is again clearly visible at 0.75V in the cathodic sweep. When the scan rate is lowered, the influence of this capacitive current is reduced, but the influence of impurities is simultaneously increased. It is then obvious a more accurate curve will be obtained if the ORR curve can be corrected for the capacitive current from adsorption processes while keeping the scan rate high enough to minimize the effect of impurities. The HOR curves shown in the figure are measured on a similar catalyst and exhibit clear H_{upd} features. The contribution of adsorption on the curve can be neglected if the active surface area is small enough, in case of single crystals for example (see *e.g.* in [40] where such adsorption features are absent). However, for nanocatalysts, high surface area is an intrinsic property of the catalyst and cannot be avoided. Therefore, proper corrections must be applied to eliminate the error induced by adsorption processes. The average contribution to the ORR current from adsorption processes is a function of the surface area and oxide adsorption, ranging from 0.6% for a Pt(111) electrode to 30-50% for high surface area Pt nanoparticles as determined from our experiments. A second way to deal with capacitive currents on high surface area catalysts has been proposed before [41], in which the scan rate can be substantially lowered (to 5 mV s^{-1}) to minimize the contribution of capacitive current. However, this leads to lower activity values due to possible contamination and the hysteresis in the adsorbtion of oxide containing species.

2.3.2.2 Influence of Ohmic drop

At high current such as the diffusion limiting current in the ORR, the voltammetric features are shifted on the potential axis compared to the blank CV due to Ohmic drop caused by system resistance. This misalignment causes the ORR curve to be distorted when the blank CV is subtracted from the measured ORR curve. A second, more worrying consequence of the Ohmic drop is the significant shift in the steepness of the curve for the ORR. These effects are also illustrated in figure 2.1A: the red curve shows the ORR current as measured with iR compensation, to be compared with the uncompensated curve in black. At low currents the two graphs overlap as the potential shift is negligible there. At high currents however, the compensated curve reflects the true potential as existing at the disk. The adsorption features now line up much better with the blank CV and indeed when the blank CV is subtracted from this curve the resulting ORR curve (figure 2.1B) has a more properly flat diffusion limiting current. The area of interest for studying the oxygen reduction reaction in the potential range of 0.85V to 1.0V exhibits a much steeper curve in case the Ohmic drop is compensated for. This is reflected in the Tafel slope as well. The insert in figure 2.1B shows the effect of iR compensation on the Tafel slope. There is a significant difference in slope between the compensated (69 mV dec^{-1}) and the uncompensated curve (99 mV dec^{-1}). As the Tafel slope is used to obtain information on the reaction kinetics, measuring the wrong slope can lead to wrong conclusions. The dependence of the HOR on Ohmic drop is shown in figure 2.1A. The steepness of the curve changes dramatically with iR drop correction. This again causes Tafel slopes to be inaccurate. Perhaps the most striking example of this is the comparison of the measured Tafel slopes with measurements in the membrane electrode assembly (MEA) [41], where the Tafel slope is found to be straight, due to the fact that in MEA's the Ohmic drop is compensated for, the mass transport is much faster, and there is no influence of capacitive currents as the current densities are measured in steady-state rather than sweeps. Furthermore, the absolute value of the kinetic current (i_{kin}), often used as an indication of the catalysts activity increases significantly when Ohmic drop is applied appropriately; see table 2.3. Thus in order to be able to compare data from different research groups it is important to compensate for Ohmic drop, lest the resistance is compared rather than the activity.

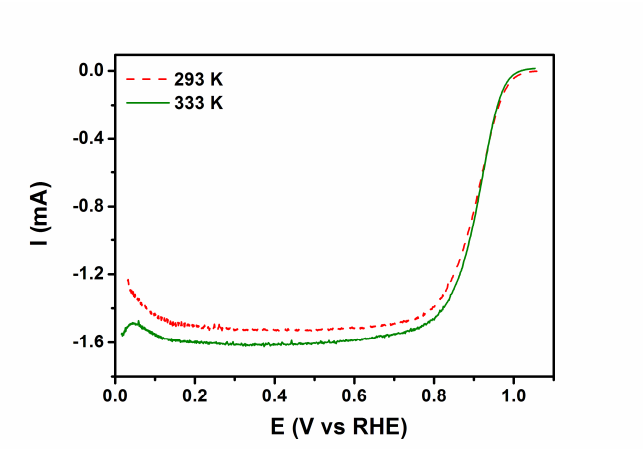

Figure 2.3. ORR dependence on temperature for the measurement with IR-drop compensation. The red curve shows the measurement at 293K; the green one shows the measurement at 333K. Experimental Conditions: Pt/C 5 nm, 0.1 M $HClO_4$, scan rate 20 mV s^{-1}, rotation 1600 rpm.

Another unfortunate side effect of solution resistance is its dependence on the temperature. Table 2.2 shows that when the temperature of the cell is increased from room temperature to 330K the measured iR drop almost halves compared to the value at 293K. Figure 2.3 shows the iR compensated curves for an ORR measurement on the Pt/C high surface area catalyst. When the results for the ORR activity of these catalysts are together analyzed, the results of which are given in table 2.3 and 2.4, one concludes that when iR compensation is not applied, the difference between $E_{1/2}$ of the room temperature experiment and the measurement at elevated temperatures is smaller than when iR compensation is properly applied (table 2.4). The kinetic current values in table 2.3 are given in mA per cm^2 electrochemical surface area. This area was determined in the same way as reported before by Mayrhofer *et al.* [10] The uncompensated data in table 2.3 matches our group's previous data [10, 42], the reported activities by other groups [7, 43, 44] and previously published benchmarks [41] almost perfectly Also, as can be seen from the value of the kinetic current at 925 mV, it is easy to draw wrong conclusions about which temperature has the highest activity for the ORR. In the uncorrected data, the elevated temperatures seem to be more active, whereas with proper correction the data shows that such is not the case. This observation also means that when we are looking in literature for data on ORR measurements with temperature dependence, we have to be very careful with interpreting such data

when it is obtained without Ohmic drop compensation. Small apparent activation of catalysts at elevated temperatures in those data may be not much more than an observation of the lower cell resistance. In addition to this, measurements of activation energies with bigger electrodes have to be very carefully compensated for Ohmic drop. As the resistance decreases with increasing temperature it will change the slope of an Arrhenius plot (log current versus the reciprocal of the absolute temperature), and thus it will cause the measured apparent activation energy to be unrepresentative of the kinetic process one is trying to measure.

Table 2.3. Kinetic current density values for the ORR of a Pt/C 5 nm nanocatalyst. The kinetic current densities were obtained from the positive-going ORR curve, which was first corrected for capacitive currents, and consecutively corrected for mass transport.

	No IR-drop correction		IR-compensated	
Potential (mV vs. RHE)	I_{kin} at 293K (mA cm_{Pt}^{-2})	I_{kin} at 333K (mA cm_{Pt}^{-2})	I_{kin} at 293K (mA cm_{Pt}^{-2})	I_{kin} at 333K (mA cm_{Pt}^{-2})
900	0.37	0.45	0.54	0.6
925	0.20	0.22	0.27	0.27
950	0.097	0.095	0.115	0.105

Table 2.4, half-wave potential ($E_{1/2}$) dependence on the Ohmic drop.

	$E_{1/2}$ at 293K (mV)	$E_{1/2}$ at 333K (mV)
No IR-drop correction	889	897
IR-compensated	905	906

2.4 Conclusion and Recommendations

In this paper, we have argued that without proper correction for 1) adsorption processes and 2) IR compensation, the values for kinetic currents of model electrocatalysts in model experimental setups may be incorrect and may lead to misleading results in the comparison of catalysts. Although we realize that this conclusion appears "old news", the examples given in this paper illustrate the dramatic influence of proper IR compensation, especially for temperature dependent measurements, that is nevertheless often disregarded.

Especially on high surface area catalysts the contribution from the oxide adsorption process at potentials of 0.8V and higher will be significant (up to 50%) and failing to correct for this makes comparisons between catalysts with different surface areas or different shapes of said oxide plateau impossible.
Ohmic drop compensation is even more important as the resistance of the solution will not always be exactly the same, especially when comparing between different setups and electrolyte concentrations and temperatures. In order to make a meaningful comparison between ORR catalysts measured in different environments, indeed even different research groups, one needs to be sure the actual reaction activity is compared and not the difference in iR drop between the different measurements.
Positive feedback is a relatively easy way of correcting for most of the resistance problem. This correction will not only make comparisons between catalysts more meaningful, it will simultaneously ensure that Tafel slopes are correct. Finally, another important advantage of properly correcting for Ohmic drop lies in the fact that conclusions derived from measurements at different temperatures will actually represent the influence of temperature on reaction kinetics, rather than on changed electrolyte conductivity. This includes proper determination of temperature dependence of the kinetic activity for the ORR, as well as apparent activation energies measured and calculated for a plethora of different reactions.
Summarizing, the problem of Ohmic drop is clearly nothing new, but is still often overlooked, or often assumed negligible, even though it is of significant influence. We recommend scrutinizing very carefully what influence this IR drop as well as adsorption processes have in an experiment, and to duly compensate for them to ensure a valid evaluation of catalysts in electrocatalysis.

References

[1] W. Vielstich, A. Lamm, and H. A. Gasteiger, eds., Handbook of Fuel Cells: Fundamentals, Technology, Applications, Wiley, 2003.
[2] H. A. Gasteiger, N. M. Markovic, and P. N. Ross, Journal of Physical Chemistry. 99 (1995) 8290.
[3] F. Gloaguen, F. Andolfatto, R. Durand, and P. Ozil, Journal of Applied Electrochemistry. 24 (1994) 863.
[4] D. Susac, A. Sode, L. Zhu, P. C. Wong, M. Teo, D. Bizzotto, K. A. R. Mitchell, R. R. Parsons, and S. A. Campbell, Journal of Physical Chemistry B. 110 (2006) 10762.
[5] W. Chen, J. M. Kim, S. H. Sun, and S. W. Chen, Journal of Physical Chemistry C. 112 (2008) 3891.

[6] A. Sode, W. Li, Y. G. Yang, P. C. Wong, E. Gyenge, K. A. R. Mitchell, and D. Bizzotto, Journal of Physical Chemistry B. 110 (2006) 8715.
[7] S. Koh and P. Strasser, Journal of the American Chemical Society. 129 (2007) 12624.
[8] N. M. Markovic, H. A. Gasteiger, and P. N. Ross, Journal of Physical Chemistry. 99 (1995) 3411.
[9] Z. Galus, C. Olson, H. Y. Lee, and R. N. Adams, Analytical Chemistry. 34 (1962) 164.
[10] K. J. J. Mayrhofer, D. Strmcnik, B. B. Blizanac, V. Stamenkovic, M. Arenz, and N. M. Markovic, Electrochimica Acta. 53 (2008) 3181.
[11] J. Newman, Journal of the Electrochemical Society. 113 (1966) 501.
[12] J. E. Harrar and I. Shain, Analytical Chemistry. 38 (1966) 1148.
[13] P. X. He and L. R. Faulkner, Analytical Chemistry. 58 (1986) 517.
[14] R. Piontelli, G. Bianchi, and R. Aletti, Zeitschrift Fur Elektrochemie. 56 (1952) 84.
[15] R. Piontelli, G. Bianchi, U. Bertocci, C. Guerci, and B. Rivolta, Zeitschrift Fur Elektrochemie. 58 (1954) 54.
[16] R. Piontelli, U. Bertocci, G. Bianchi, C. Guerci, and G. Poli, Zeitschrift Fur Elektrochemie. 58 (1954) 86.
[17] R. Piontelli, B. Rivolta, and G. Montanelli, Zeitschrift Fur Elektrochemie. 59 (1955) 64.
[18] S. Barnartt, Journal of the Electrochemical Society. 99 (1952) 549.
[19] S. Barnartt, Journal of the Electrochemical Society. 108 (1961) 102.
[20] G. L. Booman and W. B. Holbrook, Analytical Chemistry. 35 (1963) 1793.
[21] W. B. Schaap and P. S. Mckinney, Analytical Chemistry. 36 (1964) 1251.
[22] W. T. De Vries and E. Van Dalen, Journal of Electroanalytical Chemistry. 12 (1966) 9.
[23] M. Hayes, A. T. Kuhn, and W. Patefield, Journal of Power Sources. 2 (1977) 121.
[24] G. S. Popkirov, Journal of Electroanalytical Chemistry. 359 (1993) 97.
[25] J. C. Myland and K. B. Oldham, Journal of Electroanalytical Chemistry. 347 (1993) 49.
[26] J. O. Bockris, Chemical Reviews. 43 (1948) 525.
[27] R. S. Nicholson, Analytical Chemistry. 37 (1965) 667.
[28] F. Haber, Zeitschrift Für Physikalische Chemie. 32 (1900) 193.
[29] C. Dorfel, D. Rahner, and W. Forker, Journal of Electroanalytical Chemistry. 107 (1980) 257.
[30] V. R. Stamenkovic, B. Fowler, B. S. Mun, G. F. Wang, P. N. Ross, C. A. Lucas, and N. M. Markovic, Science. 315 (2007) 493.
[31] S. Koh, M. F. Toney, and P. Strasser, Electrochimica Acta. 52 (2007) 2765.
[32] A. Bonakdarpour, K. Stevens, G. D. Vernstrom, R. Atanasoski, A. K. Schmoeckel, M. K. Debe, and J. R. Dahn, Electrochimica Acta. 53 (2007) 688.
[33] T. Toda, H. Igarashi, and M. Watanabe, Journal of Electroanalytical Chemistry. 460 (1999) 258.
[34] J. Barber, S. Morin, and B. E. Conway, Journal of Electroanalytical Chemistry. 446 (1998) 125.
[35] J. Perez, H. M. Villullas, and E. R. Gonzalez, Journal of Electroanalytical Chemistry. 435 (1997) 179.
[36] T. J. Schmidt, P. N. Ross, and N. M. Markovic, Journal of Electroanalytical Chemistry. 524-525 (2002) 252.

[37] J. O. Bockris and A. M. Azzam, Transactions of the Faraday Society. 48 (1952) 145.
[38] R. C. Weast and M. J. Astle, eds., CRC Handbook of Chemistry and Physics, CRC Press Inc., Boca Raton, FL, USA, 1982-1983.
[39] D. S. Strmcnik, P. Rebec, M. Gaberscek, D. Tripkovic, V. Stamenkovic, C. Lucas, and N. M. Markovic, Journal of Physical Chemistry C. 111 (2007) 18672.
[40] D. Strmcnik, D. Tripkovic, D. van der Vliet, V. Stamenkovic, and N. M. Markovic, Electrochemistry Communications. 10 (2008) 1602.
[41] H. A. Gasteiger, S. S. Kocha, B. Sompalli, and F. T. Wagner, Applied Catalysis B-Environmental. 56 (2005) 9.
[42] K. J. J. Mayrhofer, B. B. Blizanac, M. Arenz, V. R. Stamenkovic, P. N. Ross, and N. M. Markovic, Journal of Physical Chemistry B. 109 (2005) 14433.
[43] J. B. Wu, J. L. Zhang, Z. M. Peng, S. C. Yang, F. T. Wagner, and H. Yang, Journal of the American Chemical Society. 132 (2010) 4984.
[44] S. Chen, P. J. Ferreira, W. C. Sheng, N. Yabuuchi, L. F. Allard, and Y. Shao-Horn, Journal of the American Chemical Society. 130 (2008) 13818.

Chapter 3

Monodisperse Pt_3Co Nanoparticles as a Catalyst for the Oxygen Reduction Reaction: Size-Dependent Activity

Monodisperse Pt_3Co nanoparticles with size controlled from 3 to 9 nm have been synthesized through an organic solvothermal approach and applied as electrocatalysts for the oxygen reduction reaction. Electrochemical study shows that the Pt_3Co nanoparticles are highly active for the oxygen reduction reaction and the activity is size-dependent. The optimal size for maximal mass activity was established to be around 4.5 nm by balancing the electrochemically active surface area and specific activity.

The contents of this chapter have been published: C. Wang, D. van der Vliet, K.C. Chang, H. You, D. Strmcnik, J. Schlueter, N.M. Markovic and V.R. Stamenkovic, *J. Phys. Chem. C.*, 113 **(2009)** 19365

3.1 Introduction

Alloy nanoparticles (NPs) have attracted increasing interest due to their superior performance in magnetic [1-5], optical [6-9] and catalytic [10-14] applications. Particularly, Pt alloys with transition metals (MPt with M = Fe, Co, Ni, etc.) have been found to be highly active for oxygen reduction, the troubled cathode reaction in fuel cells. [15, 16] This has initiated a lot of efforts in synthesis of Pt-based alloy catalysts, which are usually in the form of Pt_3M NPs dispersed in a high surface area carbon matrix. The approaches mostly include co-precipitation of metal salts in aqueous solution [17, 18], impregnation of transition metals into Pt/carbon catalyst [19, 20], and electrodeposition. [21] Despite the progress in preparing various types of alloy catalyst, synthesis of catalysts with monodisperse and size-controlled alloy NPs is yet challenging in the literature. On the other hand, the particle size effect is known to play an important role in catalysis, particularly in the case of electrocatalysts comprising NPs. Not only the activity but also the reaction mechanism and selectivity have been reported to be dependent on the catalyst size. [22-27] Contrary to the extensive study on conventional Pt/carbon catalysts, size-dependent activity has not been well investigated for Pt alloy catalysts [28, 29], which yet requires monodisperse alloy NPs of controlled size, composition, structure and uniform shape. [25]

3.2 Experimental

We use Pt_3Co as an example for systematic studies of size-dependent catalytic activity for the oxygen reduction reaction (ORR). Monodisperse Pt_3Co NPs were synthesized through an organic solvothermal approach modified from previous publications [30, 31], which has been demonstrated as a robust method for preparing monodisperse alloy NPs with size control and homogeneous compositions. [1-13, 32]. Electrochemical properties were compared to the commercially available state-of-the-art Pt/carbon catalyst supplied by Tanaka. Platinum acetylacetonate, $Pt(acac)_2$, was reduced by 1,2-tetradecanediol in the presence of 1-adamantanecarboxylic acid (ACA) and a large excess of oleylamine, while Co was introduced by thermal decomposition of cobalt carbonyl, $Co_2(CO)_8$ (figure 3.1a and section 3.5). Adding $Co_2(CO)_8$ at different temperatures gave $CoPt_3$

NPs of various sizes. Figure 3.1b–e show representative transmission electron microscopy (TEM) images of $CoPt_3$ NPs of 3, 4.5, 6 and 9 nm obtained by adding $Co_2(CO)_8$ at 225, 200, 170 and 145 ^oC, respectively. The control of size in this case has been reported to be due to a balance between the rates of nucleation and growth. [31] Energy-dispersive X-ray spectroscopy (EDX) analysis of the NPs shows the atomic ratio between Co and Pt is equal to 1:3 (figure 3.5). More experimental details are given in section 3.5.

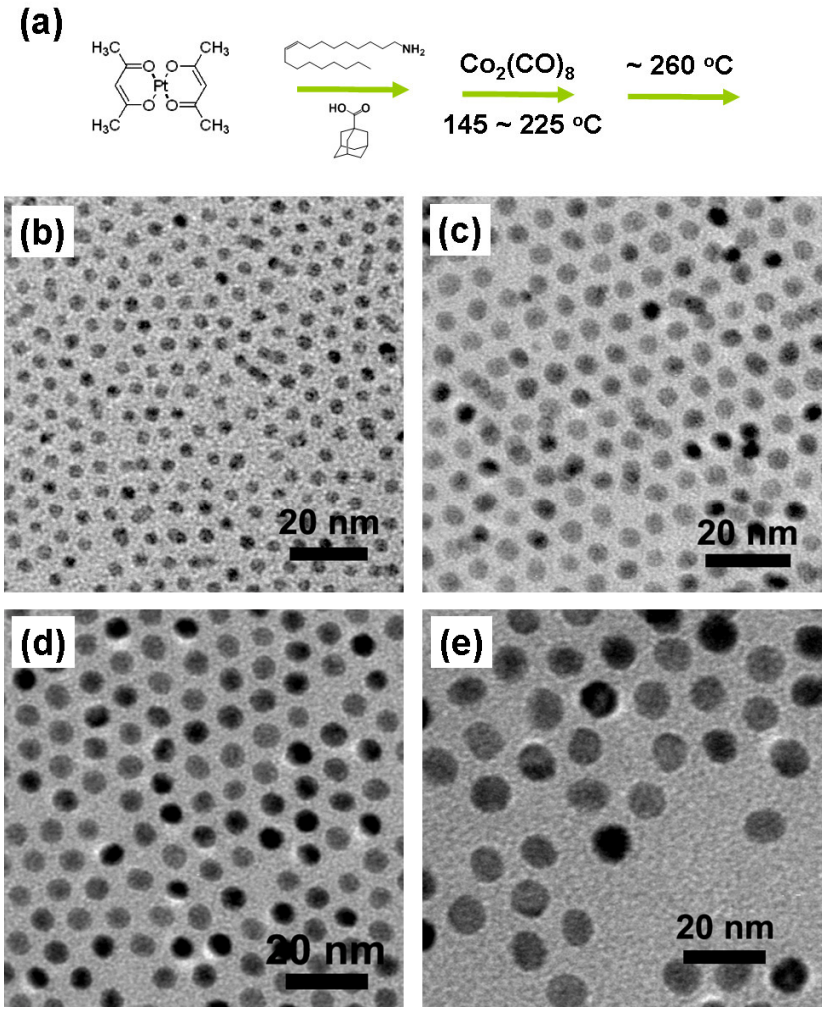

Figure 3.1. (a) Schematic illustration of the synthetic route for monodisperse $CoPt_3$ NPs. (b) - (e) TEM images of as-synthesized 3, 4.5, 6 and 9 nm $CoPt_3$ NPs.

3.3 Results and Discussion

Figure 3.2a shows X-ray diffraction (XRD) patterns of the as-synthesized $CoPt_3$ NPs. All the XRD patterns correspond to a face-centered cubic (fcc) $CoPt_3$ crystal. [30, 31] As the NP size increases, the XRD peaks become sharper; indicating the increase of crystalline size in the NPs. Crystalline sizes can further be calculated from the XRD patterns according to the Scherrer Equation, as shown in figure 3.2b. These sizes are quite close to those observed by TEM, implying the single-crystalline nature of individual NPs, which is also consistent with the high resolution TEM image analysis in the previous reports. [30, 31]

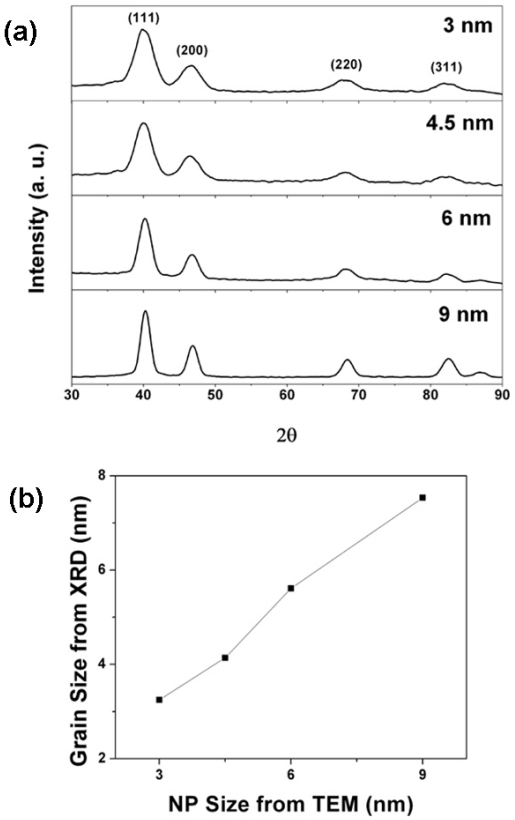

Figure 3.2. (a) XRD patterns of $CoPt_3$ NPs of various sizes showing the typical peaks of $CoPt_3$ crystals in fcc phase. (b) Crystalline sizes of $CoPt_3$ NPs as calculated from the XRD patterns according to the Scherrer Equation.

The as-synthesized NPs were supported on carbon black (Tanaka, ~ 900 m^2/g) via a colloidal-deposition approach [33] by mixing the NPs and carbon in chloroform suspension, followed by sonication. Organic surfactants were removed by heat treatment of the NPs/carbon mixture in an oxygen-containing atmosphere at 185°C. [34] The obtained catalyst was then dispersed in deionized water by vigorous sonication, and the formed suspension was pipetted on a glassy carbon (GC) electrode (6 mm in diameter). The ratio of Pt in the catalyst was tuned to 28%, and the loading of Pt on the GC electrode was controlled at 9 $\mu g/cm^2_{disk}$, with the exception of 9 nm particles, which had a loading of 12 $\mu g/cm^2_{disk}$ in order to reach the appropriate diffusion limiting current based on the disk geometry. After drying under a flow of argon, the GC electrode was immersed into 0.1 M $HClO_4$ for electrocatalytic measurements, which was carried out in a three compartment electrochemical cell with a Pt wire as counter and an Ag/AgCl as reference electrode. All potentials in this report are given versus reversible hydrogen electrode (RHE), and readout currents are corrected for the ohmic iR drop. [35, 40] The cyclic voltammogram (CV) was collected in Ar saturated solutions with a scan rate of 50 mV/s at 20°C, and ORR activity was measured by rotating disk electrode (RDE) method with a scan rate of 20 mV/s at 60°C. The electrochemical surface area of the catalyst was evaluated from the charge of under potentially deposited hydrogen (H_{upd}) and CO stripping (figure 3.6 and 3.7), and used to normalize the measured electrode current for the calculation of specific activity, which is given as the kinetic current density at 0.9 V (figure 3.8).

Figure 3.3a shows the voltammograms of $CoPt_3$/carbon NPs of various sizes. As the size of NPs increases from 3 nm to 9 nm, the H_{upd} region (0.05 V < E < 0.4 V vs. RHE) shrinks, resulting in the decrease of specific surface area from 692 to 277 cm^2/mg_{Pt} (figure 3.3b). Specific activities (at 0.9 V vs. RHE) measured with a rotation rate of 1600 rpm and a scan rate of 20 mV/s are also depicted in figure 3.3b, showing an ascending trend as the NP size increases. The specific activity of 9 nm $CoPt_3$/carbon is over two times higher than measured for 3 nm $CoPt_3$/carbon NPs. The two opposite trends in specific surface area and specific activity lead to a volcano-shape behavior in size-dependent mass activities, as shown in figure 3.3c, and therefore, the maximum mass activity has been observed for 4.5 nm Pt_3Co NPs.

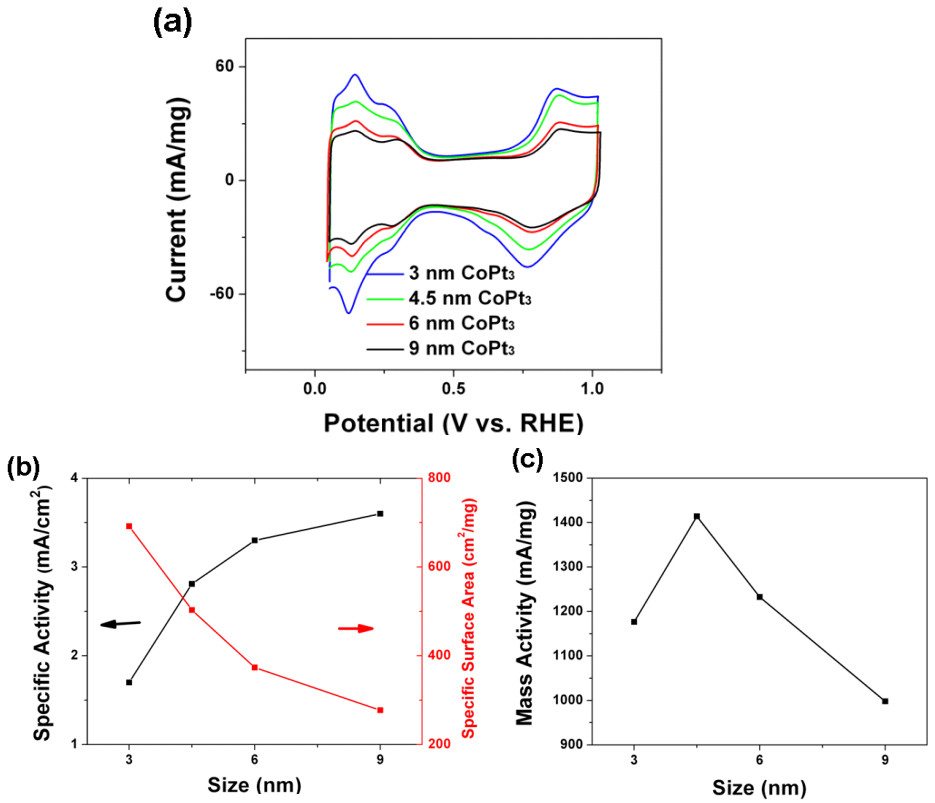

Figure 3.3. (a) CVs of $CoPt_3$ NPs of different sizes. (b) Specific activities at 0.9 V vs. RHE are measured with a scan rate of 20 mV/s and rotation rate of 1600 rpm (black); and specific surface areas (red) of $CoPt_3$/carbon catalysts. The error of specific activities was estimated to be in ±10% according to 3 measurements for each sample. (c) Mass activities of $CoPt_3$/carbon catalysts.

Even though particle size effect for the Pt catalyst has been well documented in literature [22-27], and explained in terms of the surface geometry and associated electronic properties, disputations yet exist. For example, Watanabe *et al.* claim no size effect observed in their combinational electrochemical and ^{195}Pt EC-NMR study. [36] Despite a lack of consensus, it is generally accepted that the mechanism of the Pt size effect is fulfilled through enhanced adsorption of oxygenated species (O^- and OH_{ads}, etc.) in smaller particles, due to the decrease of average coordination number [26], and consequently more pronounced oxophilic behavior. Oxygenated species adsorbed on low-coordinated Pt surface sites (steps, edges, kinks) inhibit the ORR. [23] The first systematic study of bimetallic alloy particles presented here shows that particle size effect is also reflected in the case of $CoPt_3$ NPs. A careful

analysis of the voltammograms presented in figure 3.3a shows that both the oxidation peak (~ 0.9 V) in the anodic scan and the reduction peak (~ 0.8 V) in the cathodic scan exhibit a negative shift of ~30 mV from 9 to 3 nm $CoPt_3$. Our experiments indicate that the smaller NPs are oxidized at lower potential, which corresponds to enhanced adsorption of oxygenated species and thus decreased ORR activity.

The results presented here show about 3-fold enhancement in the ORR (figure 3.4 and table 3.1) between synthesized $CoPt_3$/carbon (6 nm) and commercially available Pt/carbon (6 nm) catalysts. The enhancement has been ascribed to the modification of the Pt surface electronic structure by alloying with 3*d* transition metals. [37-39] The improvement factor is in line with that observed for extended surfaces, [13] implying that the synthetic approach and treatment procedures developed here do produce a homogeneous alloy and highly active monodisperse catalysts with controllable size. Compared with Pt alloy catalysts prepared by conventional approaches such as impregnation and co-precipitation [15-19, 24], the improved activity for Pt-bimetallic NPs developed here is due to the unique chemical solution synthesis, which generates alloy nanoparticles with more homogeneous elemental distribution and better mixing of alloying components, which was found to be crucial in determining the electronic/adsorption/catalytic properties. [12, 13]

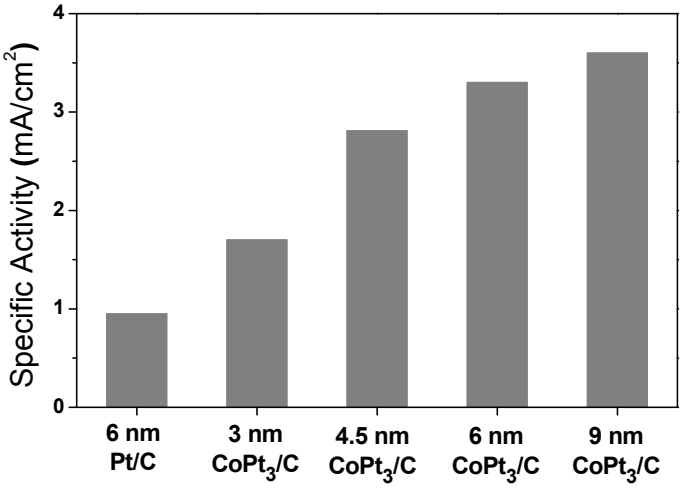

Figure 3.4. Specific activity at 0.9 V vs. RHE, 60^{o}C and 1600 rpm for $CoPt_3$/carbon catalysts compared to 6 nm Pt/carbon catalysts.

3.4 Conclusion

In summary, we have synthesized size controlled monodisperse $CoPt_3$ nanoparticles ranging from 3 nm to 9 nm, and applied them as electrocatalysts for the oxygen reduction reaction. The organic solvothermal approach has proven to be a powerful method for synthesis of high-quality alloy nanoparticles with superior performance in catalyzing the cathodic fuel cell reaction. Systematic study of the Pt-bimetallic alloy catalysts comprising nanoparticles of various sizes reveals that the ORR activity of $CoPt_3$ is size-dependent and decreases with the particle size. By balancing the specific surface area and activity, the optimal size for the maximum in mass activity was established to be around 4.5 nm. In a quest to control the size, shape, and composition of nanoparticles, the strategy and trends reported in this study may be generalized to other systems and utilized to guide the future development of advanced functional nanomaterials.

3.5 Appendix

3.5.1 Synthesis of Pt_3Co nanoparticles

In a typical synthesis of 4.5 nm Pt_3Co NPs, 0.16 mmol $Pt(acac)_2$ was dissolved in 10 ml oleylamine and 5 ml benzyl ether, in the presence of 1 mmol 1-tetradecanediol, 2.8 mmol 1-adamantanecarboxylic acid. The formed solution was heated to 200 ^oC under Ar flow. 0.25 mmol cobalt carbonyl dissolved in 1 ml dichlorobenzene was added into this hot solution under the Ar atmosphere. After 30 minutes, the solution temperature was raised to 260 ^oC and kept in reflux for 30 minutes. After the reaction, the solution was cooled down to room temperature. 40 ml iso-propanol and 20 ml ethanol were added to precipitate NPs, followed by centrifuge (6500 rpm, 6 minutes). The collected product was dispersed in 10 ml hexane for further applications. Electrochemical properties of synthesized NPs were compared to the commercially available state-of-the-art Pt/carbon catalyst supplied by Tanaka.

3.5.2 Characterization

The TEM images (figure 3.1) and EDX spectrum (figure 3.5) were collected on a Philips CM 30 TEM equipped with EDX functionality. The EDX analysis covered a large area of the nanoparticle assembly (> 1 μm × 1μm, over thousands of particles). XRD patterns (figure 3.2) were collected on a Rigaku RTP 300 RC machine. Crystalline size in the NPs were calculated by the Scherrer equation for the (111) peak after background correction of the spectrum (0.94 was used for the Scherrer constant).

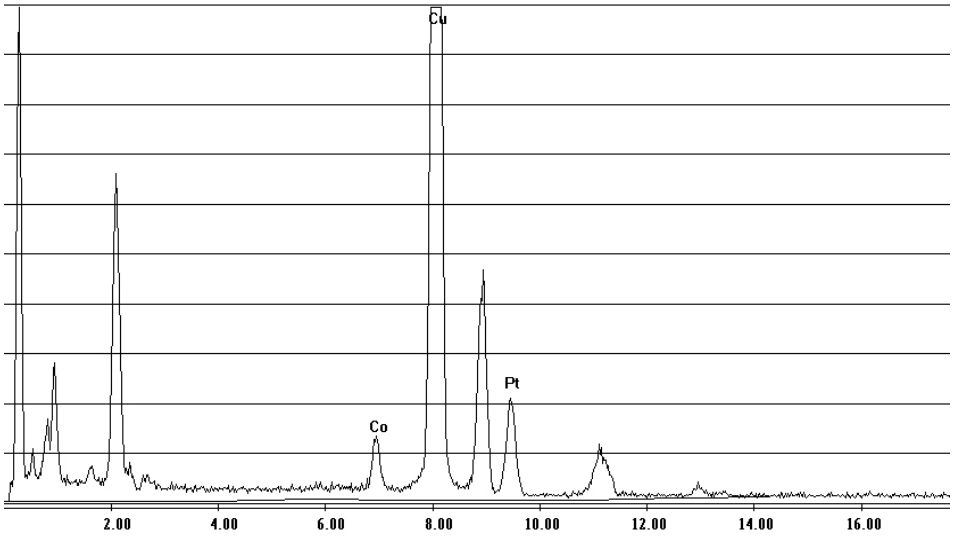

Figure 3.5. EDX spectrum of Pt3Co NPs confirming the atomic ratio between Co and Pt is equal to 1:3.

3.5.3 Electrochemical Measurements

The electrochemical measurements were conducted in a three-compartment electrochemical cell with a rotating disc electrode setup (Pine) and potentiostat (Ecochemie Autolab 302). A saturated Ag/AgCl electrode and a Pt wire were used as reference and counter electrodes, respectively. 0.1 M $HClO_4$ was used as electrolyte. Details about sample preparation and loading were presented in the text.

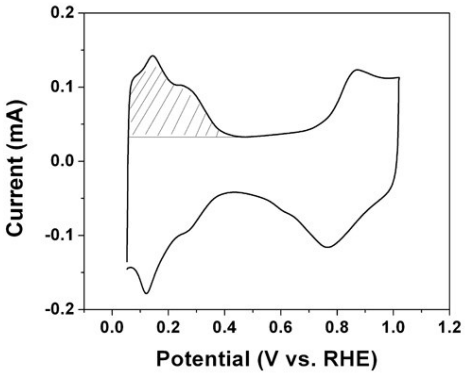

Figure 3.6. CV of 3 nm Pt_3Co/carbon catalyst measured at 50 mV s^{-1}. The electrochemically active surface area of the catalyst can be obtained by $S = \frac{Q_s}{200 \ \ \mu C \cdot cm^{-2}}$, where Qs is the surface charge that can be calculated from the area under the Hupd peak by $Q_s = \frac{\int I \cdot dE}{\nu}$, where *ν* is the scan rate.

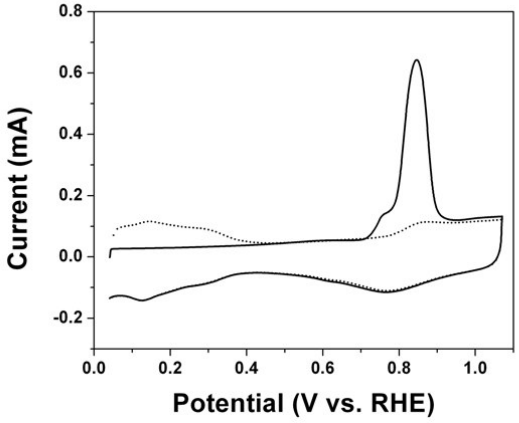

Figure 3.7. CO stripping of 3 nm Pt_3Co/carbon catalyst measured at 50 mV s^{-1}. The dashed curve is the blank CV recorded right after CO stripping. The coverage of CO calculated by $\Theta_{CO} = \frac{\frac{1}{2}Q_{CO}}{Q_{H_{upd}}}$ is 94%.

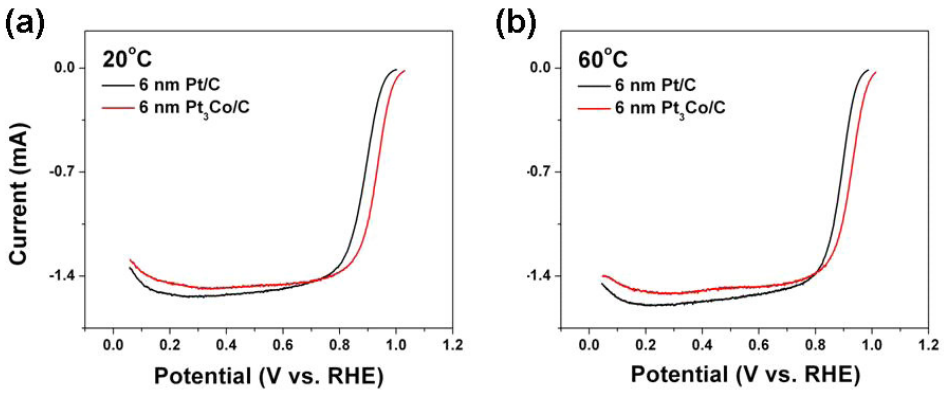

Figure 3.8. Polarization curves for 6 nm Pt and Pt_3Co/carbon catalysts measured at (a) 20°C and (b) 60°C with 20 mV s^{-1} at 1600 rpm. Kinetic current density was obtained by $\frac{1}{I} = \frac{1}{I_k} + \frac{1}{I_{diff}}$. $J_k = \frac{I_k}{surface\ \ area}$**,where the *surface area* was obtained from the CV as shown in figure 3.6 and CO stripping curve in figure 3.7.**

Table 3.1. Summary of electrochemical measurements for Pt and Pt_3Co/carbon catalysts.

NPs	Loading ($\mu g_{Pt}/cm^2_{disk}$)	Surface Area (cm^2)	Specific Activity at 0.9 V vs. RHE (mA/cm^2)	Mass Activity at 0.9 V vs. RHE (mA/mg_{Pt})
3 nm Pt_3Co	9	1.848	1.62	1176
4.5 nm Pt_3Co	9	1.344	2.68	1414
6 nm Pt_3Co	9	0.998	3.14	1233
9 nm Pt_3Co	12	0.987	3.43	998
6 nm Pt	9	0.981	0.97	374

References

[1] S. H. Sun, C. B. Murray, D. Weller, L. Folks, and A. Moser, Science 287 (2000) 1989.

[2] C. Desvaux, C. Amiens, P. Fejes, P. Renaud, M. Respaud, P. Lecante, E. Snoeck, and B. Chaudret, Nature Materials 4 (2005) 750.

[3] S. D. Bader, Reviews of Modern Physics 78 (2006) 1.

[4] W. S. Seo, J. H. Lee, X. M. Sun, Y. Suzuki, D. Mann, Z. Liu, M. Terashima, P. C. Yang, M. V. McConnell, D. G. Nishimura, and H. J. Dai, Nature Materials 5 (2006) 971.

[5] C. Wang, S. Peng, L. M. Lacroix, and S. H. Sun, Nano Research 2:380 (2009).

[6] S. Link, Z. L. Wang, and M. A. El-Sayed, Journal of Physical Chemistry B 103 (1999) 3529.

[7] E. Cottancin, J. Lerme, M. Gaudry, M. Pellarin, J. L. Vialle, M. Broyer, B. Prevel, M. Treilleux, and P. Melinon, Physical Review B 62 (2000) 5179.

[8] Y. G. Sun, B. Wiley, Z. Y. Li, and Y. N. Xia, Journal of the American Chemical Society 126 (2004) 9399.

[9] C. Wang, S. Peng, R. Chan, and S. H. Sun, Small 5 (2009) 567.

[10] T. Toda, H. Igarashi, H. Uchida, and M. Watanabe, Journal of the Electrochemical Society 146 (1999) 3750.

[11] J. Greeley and M. Mavrikakis, Nature Materials 3 (2004) 810.

[12] V. R. Stamenkovic, B. Fowler, B. S. Mun, G. F. Wang, P. N. Ross, C. A. Lucas, and N. M. Markovic, Science 315 (2007) 493.

[13] V. R. Stamenkovic, B. S. Mun, M. Arenz, K. J. J. Mayrhofer, C. A. Lucas, G. F. Wang, P. N. Ross, and N. M. Markovic, Nature Materials 6 (2007) 241.

[14] C. Wang, H. G. Yin, R. Chan, S. Peng, S. Dai, and S. H. Sun, Chemistry of Materials 21 (2009) 433.

[15] E. Blomsma, J. A. Martens, and P. A. Jacobs, Journal of Catalysis 165 (1997) 241.

[16] J. R. C. Salgado, E. Antolini, and E. R. Gonzalez, Journal of Power Sources 141 (2005) 13.

[17] Y. D. Qian, W. Wen, P. A. Adcock, Z. Jiang, N. Hakim, M. S. Saha, and S. Mukerjee, Journal of Physical Chemistry C 112 (2008) 1146.

[18] N. H. H. Abu Bakar, M. M. Bettahar, M. Abu Bakar, S. Monteverdi, J. Ismail, and M. Alnot, Journal of Molecular Catalysis a-Chemical 308 (2009) 87.

[19] M. Neergat, A. K. Shukla, and K. S. Gandhi, Journal of Applied Electrochemistry 31 (2001) 373.

[20] J. N. Soderberg, A. H. C. Sirk, S. A. Campbell, and V. I. Birss, Journal of the Electrochemical Society 152 (2005) A2017.

[21] M. A. García-Contreras, S. M. Fernández-Valverde, and J. R. Vargas-García, Journal of Alloys and Compounds 434-435 (2007) 522.

[22] K. Kinoshita, Journal of the Electrochemical Society 137 (1990) 845.

[23] K. J. J. Mayrhofer, B. B. Blizanac, M. Arenz, V. R. Stamenkovic, P. N. Ross, and N. M. Markovic, Journal of Physical Chemistry B 109 (2005) 14433.

[24] H. A. Gasteiger, S. S. Kocha, B. Sompalli, and F. T. Wagner, Applied Catalysis B-Environmental 56 (2005) 9.

[25] C. Wang, H. Daimon, T. Onodera, T. Koda, and S. H. Sun, Angewandte Chemie-International Edition 47 (2008) 3588.

[26] B. C. Han, C. R. Miranda, and G. Ceder, Physical Review B 77 (2008) 075410.

[27] C. K. Tsung, J. N. Kuhn, W. Y. Huang, C. Aliaga, L. I. Hung, G. A. Somorjai, and P. D. Yang, Journal of the American Chemical Society 131 (2009) 5816.
[28] M. K. Min, J. H. Cho, K. W. Cho, and H. Kim, Electrochimica Acta 45 (2000) 4211.
[29] Q. S. Liu, Z. Yan, N. L. Henderson, J. C. Bauer, D. W. Goodman, J. D. Batteas, and R. E. Schaak, Journal of the American Chemical Society 131 (2009) 5720.
[30] E. V. Shevchenko, D. V. Talapin, A. L. Rogach, A. Kornowski, M. Haase, and H. Weller, Journal of the American Chemical Society 124 (2002) 11480.
[31] E. V. Shevchenko, D. V. Talapin, H. Schnablegger, A. Kornowski, O. Festin, P. Svedlindh, M. Haase, and H. Weller, Journal of the American Chemical Society 125 (2003) 9090.
[32] B. L. Cushing, V. L. Kolesnichenko, and C. J. O'Connor, Chemical Reviews 104 (2004) 3893.
[33] H. F. Yin, C. Wang, H. G. Zhu, S. H. Overbury, S. H. Sun, and S. Dai, Chemical Communications (2008) 4357.
[34] Z. F. Liu, M. Shamsuzzoha, E. T. Ada, W. M. Reichert, and D. E. Nikles, Journal of Power Sources 164 (2007) 472.
[35] J. Newman, Journal of the Electrochemical Society 113 (1966) 501.
[36] H. Yano, J. Inukai, H. Uchida, M. Watanabe, P. K. Babu, T. Kobayashi, J. H. Chung, E. Oldfield, and A. Wieckowski, Physical Chemistry Chemical Physics 8 (2006) 4932.
[37] J. Greeley, J. K. Norskov, and M. Mavrikakis, Annual Review of Physical Chemistry 53 (2002) 319.
[38] J. L. Zhang, M. B. Vukmirovic, Y. Xu, M. Mavrikakis, and R. R. Adzic, Angewandte Chemie-International Edition 44 (2005) 2132.
[39] V. Stamenkovic, B. S. Mun, K. J. J. Mayrhofer, P. N. Ross, N. M. Markovic, J. Rossmeisl, J. Greeley, and J. K. Norskov, Angewandte Chemie-International Edition 45 (2006) 2897.
[40] Chapter 2 of this thesis.

Chapter 4

Monodisperse Pt_3Co Nanoparticles as Electrocatalysts: the effects of Particle Size and Pretreatment on Electrocatalytic Reduction of Oxygen

Monodisperse Pt_3Co nanoparticles have been synthesized with size control via an organic solvothermal approach. The obtained nanoparticles were incorporated into a carbon matrix and applied as electrocatalysts for the oxygen reduction reaction to investigate the effects of particle size and pretreatment on their catalytic performance. It has been found that the optimal conditions for maximum mass activity were with particles of 4.5 nm and a mild annealing temperature of about 500 ^{o}C. While the particle size effect can be correlated to the average surface coordination number, Monte Carlo simulations have been used to depict the nanoparticle structure and segregation profile, which revealed that the annealing temperature has a direct influence on the particle surface relaxation, segregation and adsorption/catalytic properties. The fundamental understanding of activity enhancement in Pt-bimetallic alloy catalysts could be utilized to guide the development of advanced nanomaterials for catalytic applications.

The contents of this chapter have been based on the article: C. Wang, G.Wang, D. van der Vliet, K.C. Chang, N.M. Markovic and V.R. Stamenkovic, *Phys. Chem. Chem. Phys.*, 12 **(2010)**, 6877

4.1 Introduction

Alloy nanoparticles (NPs) have attracted increasing interest due to their superior performance in magnetic [1-5], optical [6-8] and catalytic [9-13] applications. Particularly, Pt bimetallic alloys with transition metals (PtM with M = Fe, Co, Ni, etc.) have been found to be highly active for oxygen reduction, the troubled cathode reaction in fuel cells. [12-15] The enhancement factors for specific activity were found to be up to 3 times those on extended polycrystalline surfaces. [12] This has initiated a lot of efforts to synthesise Pt-based alloy nanoscale catalysts, which are usually in the form of PtM NPs dispersed in a high surface area carbon matrix (PtM/C). The approaches mostly include co-precipitation of metal salts in aqueous solution [16], impregnation of transition metals into Pt/carbon catalyst [17], and electrodeposition. [18, 19] Previous electrocatalytic studies for the nanocatalysts prepared via these conventional approaches under proton-exchange membrane fuel cell (PEMFC) conditions, however, failed to achieve the same level of catalytic activity as in the case of extended surfaces, *i.e.*, the specific activity at 0.9V of the nanoscale catalyst is about one order of magnitude lower than that of the extended surface of the corresponding material.[12, 14, 20-23] Nevertheless, Mukerjee *et al.* reported specific activity enhancement factors of 2–3 when using Pt–Co/C, Pt–Ni/C or Pt–Cr/C versus Pt/ C. [20, 21] Gasteiger *et al.* observed a 3-fold enhancement in specific activity for multiply-leached PtCo/C versus Pt/C in their benchmark study of oxygen reduction reaction (ORR) electrocatalysts. [14] Rotating disk electrode (RDE) studies of carbon supported alloy catalysts of similar sizes by Paulus *et al.* also showed an specific activity improvement of *ca.* 1.5 for $Pt_{0.75}Co_{0.25}$/C and $Pt_{0.75}Ni_{0.25}$/C, and a more significant enhancement of *ca.* 42 for $Pt_{0.5}Co_{0.5}$/C in comparison with Pt/C. [22, 23] These studies revealed that the alloy nanocatalysts prepared by the conventional approaches are falling behind the activities obtained on extended surfaces, and there is still much to be done to improve the quality of alloy NPs.

Meanwhile, the particle size effect is also known to play a key role in catalysis, affecting not only the activity but also the reaction mechanism, selectivity and catalyst stability. [24-26] In spite of the efforts in preparing various types of alloy catalyst, however, size-dependent activity has rarely been investigated for Pt alloy catalysts [26] compared to the extensive study in conventional Pt/C catalysts. The

challenge may lie in the size-controlled synthesis of bimetallic catalysts with monodisperse NPs of uniform composition and shape.

A promising approach toward high-quality nanomaterials for catalytic applications is the organic solution synthesis. This method has already been widely applied for synthesis of various types of nanocrystals. Not only can size be tuned from 1 nm to several hundred nanometres, but also morphology can be well controlled. [27-29] Nanomaterials from organic solution synthesis have been reported to exhibit superior functional performance in various applications. [1, 3, 30, 31] Particularly, it may be advantageous in preparation of monodisperse alloy NPs with homogeneous element distributions for catalysis. [4, 29]

The synthesis of monodisperse Pt_3Co NPs by an organic solvothermal approach is described in chapter 3. The temperature at which the Co precursor (Cobalt carbonyl, $Co_2(CO)_8$)was added, was adjusted to control the particle size from 3 to 9 nm. This has enabled the study of the particle size effect by applying these NPs as catalysts in electrocatalysis, *e.g.* the oxygen reduction reaction (ORR). Our results show that the ORR specific activity of Pt_3Co increases with the particle size, and the maximum in mass activity can be achieved with NPs of about 4.5 nm by balancing the specific surface area and specific activity. Regardless of the observed high activity and size related trends established in the previous work, other conditions of the catalyst synthesis including pretreatments have not been investigated and optimized yet. Also a deep insight into the mechanism underlying the size-dependent activity is desired for guiding further study and design of advanced catalysts. In this study, we first examine the size-dependent activity of Pt_3Co NPs for ORR and postulate the particle size effect through the change of the average coordination number of surface atoms with the particle size. We then specifically focus on the 4.5 nm Pt_3Co NPs, which have shown the highest mass activity, to study the effect of pretreatment conditions. The NPs deposited on carbon black are annealed at different temperatures and electrochemical studies are applied to clarify the effect of annealing temperature on their catalytic performance. Finally, theoretical modeling based on Monte Carlo simulation is performed for better understanding of the experimental observations.

4.2 Experimental

4.2.1 NP synthesis

The Pt_3Co NPs were synthesized through an organic solvothermal approach modified from previous publications. [32] In a typical synthesis of 4.5 nm Pt_3Co NPs, 0.16 mmol $Pt(acac)_2$ was dissolved in 10 ml oleylamine and 5 ml benzyl ether, in the presence of 1 mmol 1-tetradecanediol, 2.8 mmol 1-adamantanecarboxylic acid (ACA). The formed solution was heated to 200 ^oC under Ar flow and 0.25 mmol $Co_2(CO)_8$ dissolved in 1 ml dichlorobenzene was injected into this hot solution in Ar atmosphere. After 30 min, the solution temperature was raised to 260 ^oC and kept there for 30 min. The solution was then cooled down to room temperature and 40 ml iso-propanol and 20 ml ethanol were added to precipitate NPs, followed by centrifuging. The collected product was dispersed in 10 ml hexane for further applications. Introducing $Co_2(CO)_8$ at 225, 170 and 145 ^oC gave Pt_3Co NPs of 3, 6 and 9 nm, respectively.

4.2.2 Characterizations

TEM images and EDX spectra were collected on a Philips CM 30 TEM equipped with EDX functionality. The EDX analysis covered a large area of nanoparticle assembly(1 mm; over thousands of particles).

4.2.3 Electrochemical measurements

The Pt_3Co NPs of various sizes were supported on carbon black (Tanaka TKK, Tokyo: ~900 $m^2 g^{-1}$) *via* a colloidal deposition method. [26] Organic surfactants were removed by heat treatment of the NP/carbon mixture in oxygen-rich atmosphere at 185 ^oC. [33] The obtained catalyst was then dispersed in deionized water by vigorous sonication, and the formed suspension was pipetted on the surface of a glassy carbon (GC) electrode (6 mm in diameter). The ratio of Pt in the catalyst was tuned to 28 wt-%, and the loading of Pt on GC electrode was set at 9 $\mu g\ cm^2_{disk}$, with the exception of 12 $\mu g\ cm^2_{disk}$ for 9 nm particles in order to reach proper diffusion limiting current based on the geometry of the disk. After drying under argon flow, the GC electrode was immersed into electrolyte. The

electrochemical measurements were conducted in a three-compartment electrochemical cell in a rotating disc electrode (RDE) setup. A saturated Ag/AgCl electrode and a Pt wire were used as reference and counter electrodes, respectively in 0.1 M $HClO_4$ electrolyte. Cyclic voltammogram (CV) was collected under Ar saturation with scanning rates of 20 and 50 mV s^{-1} at 20 ^oC, and ORR activity was measured by RDE method with scan rate of 20 mV s^{-1} at 60 ^oC. All potentials in this report are given versus reversible hydrogen electrode (RHE, calibrated by the H_2 oxidation reaction after each measurement), and readout currents are corrected for the ohmic iR drop. [34] The specific activity was represented as the kinetic current density (j_k) at 0.9 V vs. RHE.

4.2.4 Simulation

Monte Carlo (MC) simulation was employed in this work to derive the equilibrium surface composition of the Pt_3Co alloy NPs. In our simulation, we applied canonical ensemble statistical mechanics. Starting from an initial configuration of Pt_3Co particle with randomly distributed Pt and Co atoms, a series of configuration transformations are performed to reach the thermodynamically equilibrated states of the simulated system. At each MC step, two randomly selected atoms with different element types exchange their positions and the energy change ΔE associated with this change was then calculated using a modified embedded atom method. [35, 36] If the energy decreases ($\Delta E < 0$), we always proceed with the new configuration; while the energy increases ($\Delta E > 0$), the new configuration is retained with a probability P given by $P = \exp(\Delta E/k_BT)$. Here, k_B is the Boltzmann constant and T is the temperature. Similar approach has been successfully applied before to predict the surface segregation in Pt–Ni, [37] Pt–Re, [38] and Pt–Mo [39] NPs.

4.3 Results and discussion

The synthesized monodisperse Pt_3Co NPs with sizes controlled from 3 to 9 nm were incorporated into carbon black and applied as electrocatalysts for the ORR to study the size effect on their catalytic performance. Pretreatment conditions were also investigated by annealing the catalyst at different temperatures before the electrochemical measurements of the ORR activity. A theoretical explanation of the

observed phenomena was established based on Monte Carlo simulation of the element distribution in the NPs exposed to different treatment procedures.

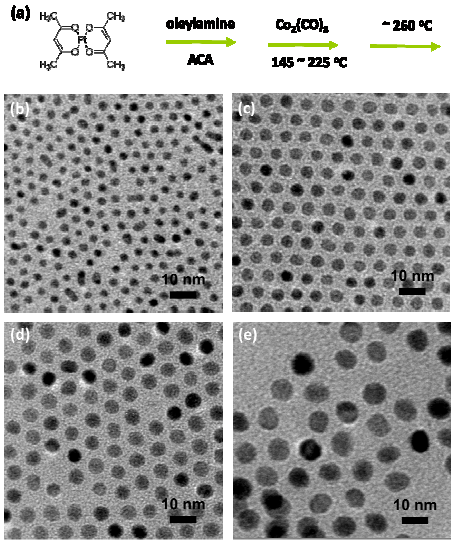

Figure 4.1 (a) Schematic illustration of the synthesis of Pt_3Co NPs via an organic solvothermal approach. (b)–(e) TEM images of 3, 4.5, 6and 9 nm Pt_3Co NPs respectively. The contrast difference among the NPs is not caused by compositional variance, but instead by the different crystalline alignment against the electron beam in imaging.

4.3.1 Size controlled synthesis of Pt_3Co NPs

Figure 4.1a illustrates the scheme of the synthesis. The platinum precursor, $Pt(acac)_2$, was dissolved in an high-boiling-point organic solvent (benzyl ether, phenyl ether, octyl ether, etc.) with the assistance of surfactants, oleylamine and ACA. Diol was added as reducing agent. The obtained mixture was heated up in an inert atmosphere (N_2 or Ar) to an elevated temperature (145–225 ^oC), where reduction of Pt salt started and generated Pt^0 species. The injection of $Co_2(CO)_8$ induced an immediate change of the solution color from transparent light yellow to black, due to the fast decomposition of $Co_2(CO)_8$ and nucleation of Co with Pt. The formed nuclei were further grown into NPs by raising the temperature to 260 ^oC (due to the large volume ratio of oleylamine, the solution cannot be heated to reflux within the Ar saturated flask). Figure 1b–e show the representative TEM imagesof 3,4.5,6 and 9 nm Pt_3Co NPs obtained by adding Co precursor at 225, 200, 170 and 145 ^oC. The size of the obtained NPs could be controlled by the amount of

precursor left after the instantaneous nucleation after $Co_2(CO)_8$ was injected. For introduction of Co at a low temperature (*e.g.*, 145 ^oC), the nucleation rate was rather slow and thus the number of nuclei formed was small. Plenty of precursors were left for further growth, allowing the NPs to grow into big size (9 nm). In contrast, at a high injection temperature (*e.g.*, 200 ^oC), most of the precursor was consumed by the boosted nucleation and a large number of nuclei formed, and therefore, only NPs of small size (3 nm) can be obtained. [10] A similar mechanism has also been applied to explain the size control of other NPs growing in organic solution. [40, 41]

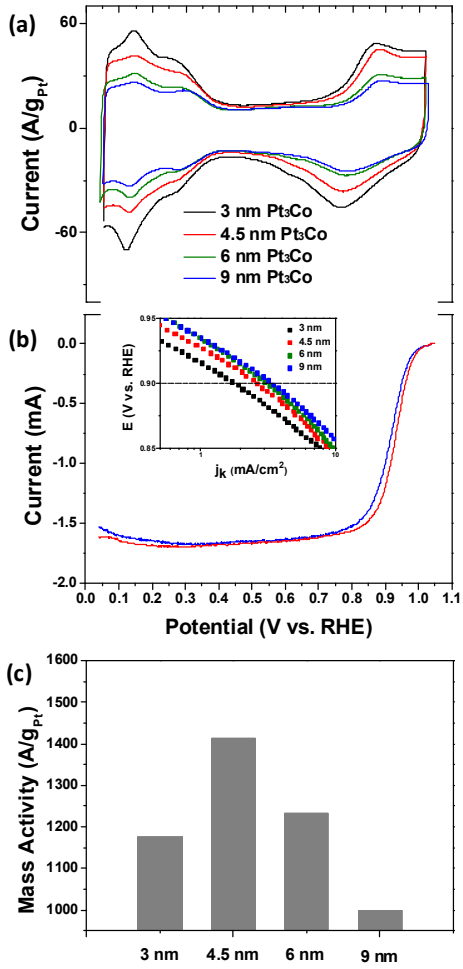

Figure 4.2 (a) Voltammograms and (b) polarization curves recorded for Pt_3Co NP catalysts of various sizes, with the inset showing the corresponding Tafel plots. (c) The summary of mass activity vs. particle size.

4.3.2 Size-dependent activity

The particle size effect for a Pt catalyst has been well known from the literature. [24, 25] Though disputations still exist, [42] it is generally accepted that the mechanism of Pt-size effect is due to enhanced adsorption of oxygenated species (OH_{ad} formed from oxidation of water) on smaller particles with decreased average coordination numbers [25], and consequently more pronounced oxophilic behavior. It is shown here that the particle size effect also exists in Pt bimetallic alloy catalysts. From the voltammograms depicted in figure 4.2a, it is found that the H_{upd} region (0.05 V < E < 0.4 V vs. RHE) shrinks as the size of the NPs increases from 3 to 9 nm, indicating a reduced specific surface area owing to the increase of particle size. The specific activities measured by RDE increase in the following trend: 3 < 4.5 < 6 < 9 nm (figure 4.2b), with the activity of 9 nm being twice that for 3 nm Pt_3Co NPs. It should be noted that, during operation in a low pH environment such as PEMFC, all of the surface Co atoms would be dissolved immediately resulting in skeleton type of surface morphology with low coordinated Pt topmost atoms. [12] The level of catalytic enhancement is thus likely to depend on the Co concentration in the subsurface layers and the extent of surface Pt coordination. By balancing these two opposite trends, i.e. smaller surface area and higher specific activity as particle size increases, the maximum mass activity has been achieved with 4.5 nm Pt_3Co NPs (figure 4.2c). The catalyst with this size was hence in the focus of the following studies.

4.3.3 Annealing temperature

Pretreatment of the catalyst by annealing is an important procedure in alloy catalyst preparation. This is usually carried out in vacuum or a reducing atmosphere (H_2, CO, etc.) and the general purpose is to homogenize the alloy composition. However, annealing always comes together with sintering of NPs. Lack of control over size, alloy homogeneity and crystal structure of catalyst particles has made it ambiguous in previous studies for annealing effect. [21, 43, 44] The monodisperse and homogeneous Pt_3Co NPs prepared here, however, have enabled a systematic study of the annealing effect on catalytic performance for bimetallic alloy nanoscale catalyst. Based on the established activity dependence versus particle size, we were

able to distinguish the effect of annealing from size and thus to rule out the intrinsic contribution of the pretreatment on activity enhancement.

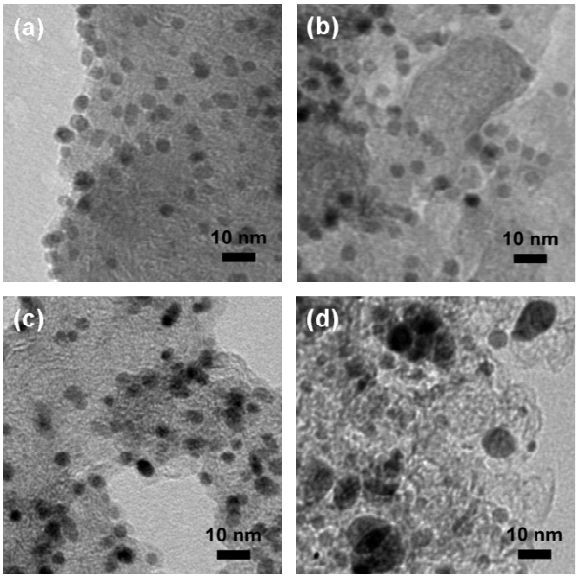

Figure 4.3, TEM images of (a) as prepared, and (b) 400 ^oC, (c) 500 ^oC, (d) 800 ^oC annealed 4.5 nm Pt_3Co/C catalysts.

The as-prepared (figure 4.3a) 4.5 nm Pt_3Co/C catalyst was treated for annealing procedures at various temperatures ranging from 300 to 800 ^oC (in Ar + 5% H_2). No obvious size or morphology change was observed for the catalysts annealed up to 400 ^oC (figure 4.3b). Particle sintering appeared for the catalyst annealed at temperatures higher than 500 ^oC, yet was not significant at this temperature (figure 4.3c) but evident at 800 ^oC (figure 4.3d). In the latter case, agglomeration of particles with sizes over 20 nm has been observed. The observed trend of size change was verified by XRD analysis. Figure 4.4a shows the XRD patterns recorded for as prepared and various annealed catalysts. All the patterns show characteristic peaks of Pt_3Co crystal in disordered fcc phase. [26, 44] According to the Scherrer equation, crystalline size in the catalyst can be calculated from the peak width in the XRD pattern. The results corresponding to the calculation for (111) peak were depicted in figure 4.4b. Consistent with the observation from TEM, the size enlargement was insignificant for annealing up to 500 ^oC, while the average particle size increased to ~6 nm for 600 ^oC and ~13 nm for 800 ^oC annealing. Unlike the report by Schulenburg *et al.* [44], our catalysts show single crystal phase

under annealing, conforming the homogeneous alloy composition in the fcc Pt_3Co NPs. The exclusion of crystal phase alteration in addition thus allows exploration of the intrinsic effect of annealing on the catalytic performance of the catalyst.

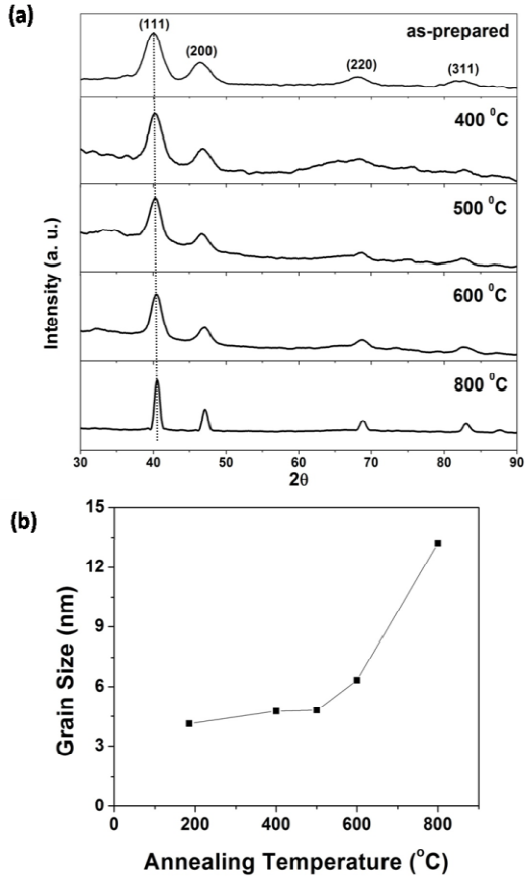

Figure 4.4 (a) XRD patterns of the 4.5 nm Pt_3Co/C catalysts at various treatment stages. (b) Crystal grain size corresponding to the patterns shown in (a), calculated based on Sherrer equation.

Figure 4.5a shows the voltammograms of the as-prepared and various annealed catalysts. The H_{upd} regions shrank as the annealing temperature increased, indicating the reduction of electrochemical surface area (figure 4.5b). The change in surface area however is not exactly corresponding to the size change observed by TEM and XRD, where it is shown that the particle size was not significantly enlarged after annealing at 500 ^{o}C, but the surface area decrease started for

annealing down to 300 °C. The divergence could be clarified, assuming that the annealing at moderate temperatures (≤ 500 °C) would not induce massive particle sintering, but can still reduce surface roughness of the particles compared to non-annealed NPs. The latter effect is not only to be reflected by the change of surface area, but more prominent in activity improvement since it diminishes surface defects, relaxes low-coordinated surface sites, lowers the oxophilicity and enhance the stability of the surface. In addition, at the moderate temperatures (400–500 °C) the compositional profile of NPs in the near surface region could be changed due to Pt segregation, which will be detailed in the next section.

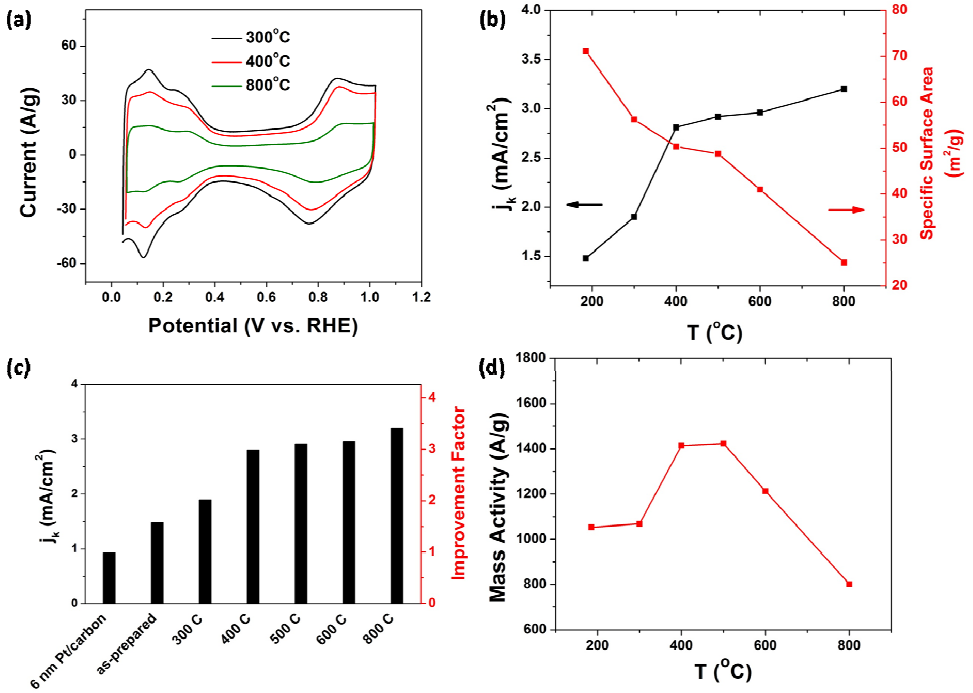

Figure 4.5 (a) Voltammograms recorded for Pt_3Co NP catalysts annealed at different temperatures. (b) The plots of specific activity and specific surface area versus annealing temperature. (c) The summary of specific activities and corresponding improvement factors against the Pt/C catalyst. (d) The plot of mass activity versus the annealing temperature.

Another important finding is related to the position of the oxidation peak (~0.9 V in the anodic scan) and the reduction peak (~0.8V in the cathodic scan). For the Pt_3Co/C annealed at 400 °C and higher temperatures these peaks exhibit a small yet still visible positive shift versus the as-prepared and 300 °C annealed catalyst, with the extent of shift slightly ascending as the annealing temperature increases. This

indicates reduced adsorption of blocking oxygenated species on those annealed catalysts, which has a direct impact on the ORR reaction kinetics as given by the pre-exponential factor of the conventional transition-state-theory rate expression. [45] It is evidenced by the trend in specific activities recorded for differently treated Pt_3Co/C NPs, as shown by the black curve in figure 4.5b. All of the annealed catalysts have ORR activities higher than the as-prepared one. While raising the annealing temperature leads to precipitous activity enhancement for the low-temperature region, the improvement trend significantly slows down for T > 400 ^{o}C.Aspecific activity boost of almost 1 mA cm^{2} was obtained for temperature elevation from 300 to 400 ^{o}C, implying that surface segregation may have happened. Compared to a state-of-the-art Pt/C catalyst with relatively large particle size (5 nm Pt, Tanaka), the as-prepared Pt_3Co/C shows an enhancement factor of about 1.5 times, while a moderate annealing temperature (400–500 ^{o}C) can give a total ORR activity enhancement up to 3 times larger (figure 4.5c) without inducing significant particle sintering.

The descending trend in specific surface area for different annealing temperatures is followed by an ascending trend in specific activities, generating volcano shape in the dependence of mass activity on annealing temperature (figure 4.5c). The optimal treating conditions to obtain the maximal mass activity were thus found to be in the range of 400–500 ^{o}C in this case (figure 4.5d).

It is important to point out that the activities presented here are much higher than those reported in the literature for PtCo alloy catalysts prepared by conventional co-precipitation or impregnation methods, and also higher than the values we measured for commercial PtCo/C. [14, 46] This suggests that the NPs obtained from organic solution synthesis may have a more homogeneous alloy composition than those prepared by the conventional methods.

4.3.4 Modeling and mechanisms

Further insight into the effects of particle size and annealing on the ORR activity was provided by modeling the nanostructure evolution depending on the size and annealing temperatures. Previous work on extended surfaces has demonstrated that element segregation in PtM bimetallic alloys can generate surface structures with Pt-skin layer and transition metal enriched subsurface layer. [12, 13] Since then many attempts have been dedicated to achieve the structure architecture at nanoscale. Chen *et al.* [46] treated the commercial Pt_3Co/C catalyst in a controlled

manner with acid leaching and high-temperature annealing(~1000 K) sequentially, and claimed the observation of ‘‘sandwich-segregation’’ structures with Pt-rich surface and Co-rich subsurface layer which was, however, associated with the particle aggregation and size increase after the annealing. An ORR activity enhancement of ~4 times was observed and ascribed to the surface segregation in this report. Mayrhofer *et al.* [47] applied CO annealing to induce surface segregation for Pt_xCo_y/Pt core/shell NPs. Though an activity improvement factor of ~2.5 was reported, the required potential cycling in an alkaline electrolyte complicates the catalyst preparation procedures and limits the potential of scaling up this approach. Nonetheless, a correlation of the pretreatment conditions of Pt-bimetallic catalysts with their catalytic performance is yet ambiguous and challenging, while its significance has been well recognized for development and synthesis of advanced catalysts for fuel-cell reactions.

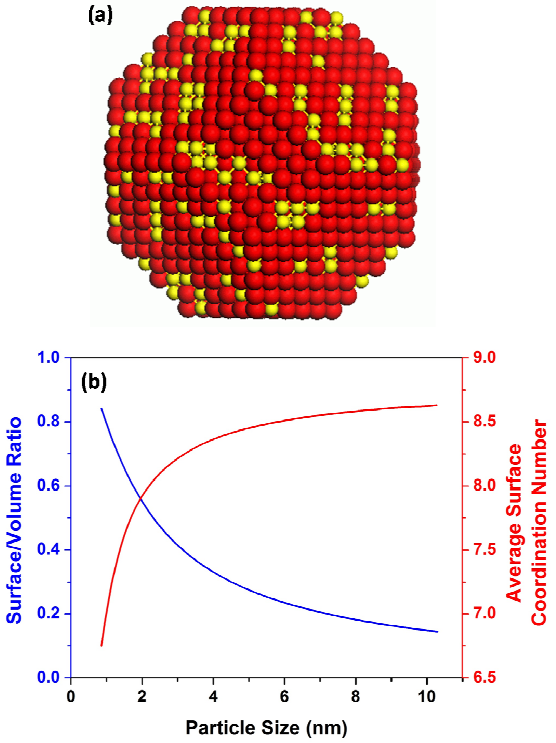

Figure 4.6 (a) Atomic model of a cubo-octahedral Pt_3Co. Red spheres illustrate the position of Pt atoms; yellow spheres depict the Co atoms. NP of fcc phase. (b) The statistical results of the ratio between the number of atoms on the surface and that of the whole particle (left axis), and the average coordination number of surface atoms (right axis) as functions of the particle size.

In order to pave the way toward a fundamental understanding of the electrochemical results depicted above, we first set up an atomic model of the Pt_3Co NPs. figure 4.6a shows a cubo-octahedral Pt_3Co NP with fcc lattice. The lattice constant adopts a value of 3.831 Å. [48] As the number of atoms in the particle enlarges, the particle size increases, and the ratio of surface atoms in the particle (surface/volume ratio, figure 4.6b) decreases, corresponding to reduced specific surface area (figure 4.2c). Another consequence of the size dependence is the average surface coordination number of the particle increases with the particle size. While a 3 nm Pt_3Co NP has an average surface coordination number of ~8.2, a 9 nm particle has a number of over 8.6. Such differences in coordination might have a substantial influence on the surface adsorption properties, as revealed by the voltammograms and ORR activities of Pt_3Co NPs of different sizes (figure 4.2). While the particle size effect can be resolved clearly and quantitatively, it is not that straightforward to identify the correlation between annealing temperature and ORR activity. The possibility of crystal phase divergence, as reported by Schulenburg *et al.* [44] has been excluded by the XRD analyses of the catalysts after annealing (figure 4.4), which also show that 1 the particle size effect is unlikely to contribute the observed activity enhancement for annealing at and below 500 ^{o}C. Therefore, the nanostructure, composition profile and element segregation seem to be dominant in this case. To investigate this we have carried out simulations of element segregation in the NPs with and without low-coordinated surface sites. Starting from a 4.3 nm Pt_3Co NP of perfect cubo-octahedral shape and with randomly distributed Pt and Co atoms, figure 4.7a and b show the structure of a single NP after a sequential 2 million steps of Monte Carlo simulation at 400 ^{o}C. The resultant Pt concentrations are 99 at.% in the outermost surface layer, 44 at.% in the second sub-surface layer, and 92 at.% in the third sub-surface layer. On the contrary, for a particle of the same shape and size but with the outermost surface layer to be amorphous, the simulation resulted in Pt ratios of 70 at.% in the outermost surface layer, 80 at.% in the sub-surface layer, and 71 at.% in the third sub-surface layer (figure 4.7c and d). The presence of Co on the surface for NPs with an amorphous outermost atomic layer thus implies that the surface segregation should happen after the surface relaxation stage.

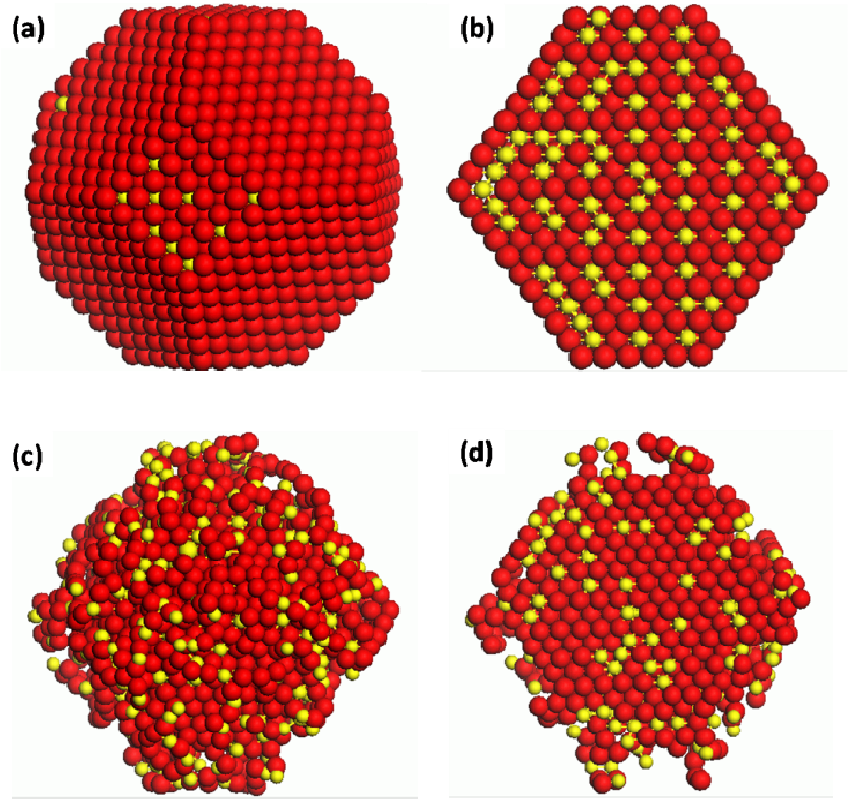

Figure 4.7 Monte Carlo simulation results of surface segregation for the Pt_3Co particle: (a), (b) without surface defect; (c), (d) with the first atomic layer amorphous. Here the right-side images are cross-section views of the particles represented in 3D on the left.

Therefore, we propose that the annealing-temperature-dependent ORR performance can be interpreted in a sequential stage mechanism. Upon annealing, the first response of the bimetallic NPs could be surface relaxation, diminishing low-coordinated surface sites. This process can be initiated at rather low temperatures (*e.g.*,<300 ^{o}C) and prevailing the activity enhancement in this temperature range. As the temperature is raised(~400 ^{o}C), bulk atomic diffusion is accelerated and element segregation alternates the particle concentration profile to be with surface enriched in Pt and subsurface in Co, providing the activity boost that originates from the modification of surface electronic structure and adsorption properties by the subsurface transition metal atoms, as well as protection of Co dissolution. [13] Further specific activity enhancement at rather high temperatures (>500 ^{o}C) can be ascribed to particle size increase caused by catalyst aggregation and sintering.

4.4 Summary

We have prepared Pt_3Co nanoparticle catalysts with size control, and investigated the effects of particle size and annealing temperature on their catalytic properties toward the oxygen reduction reaction. Based on the Monte Carlo simulation of the nanoparticle structure and element segregation, we have been able to correlate the particle size effect with the average surface coordination number, as well as the pretreatment annealing temperature with the particle surface relaxation and segregation. The developed strategies and proposed mechanisms thus shed a light on the fundamental understanding of activity enhancement in Pt-bimetallic alloy catalysts, which could also be generalized to the synthesis of advanced catalysts for other applications.

References

[1] S. D. Bader, Reviews of Modern Physics. 78 (2006) 1.
[2] C. Desvaux, C. Amiens, P. Fejes, P. Renaud, M. Respaud, P. Lecante, E. Snoeck, and B. Chaudret, Nature Materials. 4 (2005) 750.
[3] W. S. Seo, J. H. Lee, X. M. Sun, Y. Suzuki, D. Mann, Z. Liu, M. Terashima, P. C. Yang, M. V. McConnell, D. G. Nishimura, and H. J. Dai, Nature Materials. 5 (2006) 971.
[4] S. H. Sun, C. B. Murray, D. Weller, L. Folks, and A. Moser, Science. 287 (2000) 1989.
[5] C. Wang, Y. L. Hou, J. M. Kim, and S. H. Sun, Angewandte Chemie-International Edition. 46 (2007) 6333.
[6] S. Link, Z. L. Wang, and M. A. El-Sayed, Journal of Physical Chemistry B. 103 (1999) 3529.
[7] Y. G. Sun, B. Wiley, Z. Y. Li, and Y. N. Xia, Journal of the American Chemical Society. 126 (2004) 9399.
[8] C. Wang, S. Peng, R. Chan, and S. H. Sun, Small. 5 (2009) 567.
[9] C. Wang, H. G. Yin, R. Chan, S. Peng, S. Dai, and S. H. Sun, Chemistry of Materials. 21 (2009) 433.
[10] T. Toda, H. Igarashi, H. Uchida, and M. Watanabe, Journal of the Electrochemical Society. 146 (1999) 3750.
[11] J. Greeley and M. Mavrikakis, Nature Materials. 3 (2004) 810.
[12] V. R. Stamenkovic, B. S. Mun, M. Arenz, K. J. J. Mayrhofer, C. A. Lucas, G. F. Wang, P. N. Ross, and N. M. Markovic, Nature Materials. 6 (2007) 241.
[13] V. R. Stamenkovic, B. Fowler, B. S. Mun, G. F. Wang, P. N. Ross, C. A. Lucas, and N. M. Markovic, Science. 315 (2007) 493.
[14] H. A. Gasteiger, S. S. Kocha, B. Sompalli, and F. T. Wagner, Applied Catalysis B-Environmental. 56 (2005) 9.

[15] P. J. Ferreira, G. J. la O', Y. Shao-Horn, D. Morgan, R. Makharia, S. Kocha, and H. A. Gasteiger, Journal of the Electrochemical Society. 152 (2005) A2256.
[16] Y. D. Qian, W. Wen, P. A. Adcock, Z. Jiang, N. Hakim, M. S. Saha, and S. Mukerjee, Journal of Physical Chemistry C. 112 (2008) 1146.
[17] J. N. Soderberg, A. H. C. Sirk, S. A. Campbell, and V. I. Birss, Journal of the Electrochemical Society. 152 (2005) A2017.
[18] S. Tominaka, T. Momma, and T. Osaka, Electrochimica Acta. 53 (2008) 4679.
[19] Y. Saejeng and N. Tantavichet, Journal of Applied Electrochemistry. 39 (2009) 123.
[20] S. Mukerjee and S. Srinivasan, Journal of Electroanalytical Chemistry. 357 (1993) 201.
[21] S. Mukerjee, S. Srinivasan, M. P. Soriaga, and J. Mcbreen, Journal of Physical Chemistry. 99 (1995) 4577.
[22] U. A. Paulus, A. Wokaun, G. G. Scherer, T. J. Schmidt, V. Stamenkovic, N. M. Markovic, and P. N. Ross, Electrochimica Acta. 47 (2002) 3787.
[23] U. A. Paulus, A. Wokaun, G. G. Scherer, T. J. Schmidt, V. Stamenkovic, V. Radmilovic, N. M. Markovic, and P. N. Ross, Journal of Physical Chemistry B. 106 (2002) 4181.
[24] K. Kinoshita, Journal of the Electrochemical Society. 137 (1990) 845.
[25] K. J. J. Mayrhofer, B. B. Blizanac, M. Arenz, V. R. Stamenkovic, P. N. Ross, and N. M. Markovic, Journal of Physical Chemistry B. 109 (2005) 14433.
[26] Chapter 3 of this Thesis
[27] Y. W. Jun, J. S. Choi, and J. Cheon, Angewandte Chemie-International Edition. 45 (2006) 3414.
[28] C. B. Murray, C. R. Kagan, and M. G. Bawendi, Annual Review of Materials Science. 30 (2000) 545.
[29] B. L. Cushing, V. L. Kolesnichenko, and C. J. O'Connor, Chemical Reviews. 104 (2004) 3893.
[30] C. Burda, X. B. Chen, R. Narayanan, and M. A. El-Sayed, Chemical Reviews. 105 (2005) 1025.
[31] R. Ferrando, J. Jellinek, and R. L. Johnston, Chemical Reviews. 108 (2008) 845.
[32] E. V. Shevchenko, D. V. Talapin, A. L. Rogach, A. Kornowski, M. Haase, and H. Weller, Journal of the American Chemical Society. 124 (2002) 11480.
[33] Z. F. Liu, M. Shamsuzzoha, E. T. Ada, W. M. Reichert, and D. E. Nikles, Journal of Power Sources. 164 (2007) 472.
[34] Chapter 2 of this Thesis.
[35] M. I. Baskes, Physical Review B. 46 (1992) 2727.
[36] M. I. Baskes and R. A. Johnson, Modelling and Simulation in Materials Science and Engineering. 2 (1994) 147.
[37] G. F. Wang, M. A. Van Hove, P. N. Ross, and M. I. Baskes, Journal of Chemical Physics. 122 (2005).
[38] G. F. Wang, M. A. Van Hove, P. N. Ross, and M. I. Baskes, Journal of Chemical Physics. 121 (2004) 5410.
[39] G. F. Wang, M. A. Van Hove, P. N. Ross, and M. I. Baskes, Journal of Physical Chemistry B. 109 (2005) 11683.
[40] J. T. Ren and R. D. Tilley, Journal of the American Chemical Society. 129 (2007) 3287.
[41] C. Wang, H. Daimon, T. Onodera, T. Koda, and S. H. Sun, Angewandte Chemie-International Edition. 47 (2008) 3588.

[42] H. Yano, J. Inukai, H. Uchida, M. Watanabe, P. K. Babu, T. Kobayashi, J. H. Chung, E. Oldfield, and A. Wieckowski, Physical Chemistry Chemical Physics. 8 (2006) 4932.
[43] H. Liu, W. Li, and A. Manthiram, Applied Catalysis B-Environmental. 90 (2009) 184.
[44] H. Schulenburg, E. Muller, G. Khelashvili, T. Roser, H. Bonnemann, A. Wokaun, and G. G. Scherer, Journal of Physical Chemistry C. 113 (2009) 4069.
[45] N. M. Markovic, H. A. Gasteiger, B. N. Grgur, and P. N. Ross, Journal of Electroanalytical Chemistry. 467 (1999) 157.
[46] S. Chen, P. J. Ferreira, W. C. Sheng, N. Yabuuchi, L. F. Allard, and Y. Shao-Horn, Journal of the American Chemical Society. 130 (2008) 13818.
[47] K. J. J. Mayrhofer, V. Juhart, K. Hartl, M. Hanzlik, and M. Arenz, Angewandte Chemie-International Edition. 48 (2009) 3529.
[48] P. Villars and L. D. Calvert, Pearson's Handbook of Crystallographic Data for Intermetallic Phases, ASM International, Materials Park, OH, 1991.

Chapter 5

Multimetallic Au/$FePt_3$ Nanoparticles as Highly Durable Electrocatalyst

We report the design and synthesis of multimetallic Au/Pt-bimetallic nanoparticles as a highly durable electrocatalyst for the oxygen reduction reaction (ORR) in proton exchange membrane fuel cells (PEMFCs). This system was first of all studied on well-defined Pt and FePt thin films deposited on a Au(111) surface, which has guided the development of novel synthetic routes toward shape-controlled Au nanoparticles, coated with a Pt-bimetallic alloy. It has been demonstrated that these multimetallic Au/$FePt_3$ nanoparticles possess both the high catalytic activity of Pt-bimetallic alloys and the superior durability of the tailored morphology and composition profile, with mass-activity enhancement of more than one order of magnitude over Pt catalysts. The reported synergy between well-defined surfaces and nanoparticle synthesis offers a persuasive approach toward nanomaterials with advanced functionality.

The contents of this chapter have been submitted: C. Wang, D. van der Vliet, K.L. More, N.J. Zaluzec, S. Peng, S. Sun, H. Daimon, G. Wang, J. Greeley, J. Pearson, A.P. Paulikas, G. Karapetrov, D. Strmcnik, N.M. Markovic and V. R. Stamenkovic, *Nano Lett.*, **(2010)**

5.1 Introduction

Fuel cell technology is believed to be the next generation of energy solutions for powering stationary systems, portable electronic devices and vehicles. [1] With hydrogen as a fuel, this technology is environmentally friendly, as it generates electricity from the hydrogen oxidation reaction at the anode and oxygen reduction reaction (ORR) at the cathode, producing water as the only by-product. Platinum in the form of nanoparticles dispersed on a high surface area carbon matrix is considered to be the catalyst of choice for these two reactions. [2] However, Pt that is in general chemically inert becomes unstable when exposed to the hostile electrochemical environments where Pt surface atoms dissolve and migrate, resulting in aggregation of nanoparticles and loss of surface area, activity and power density. [3] Specifically, the instability of Pt at the cathode side represents one of the major limitations for commercialization of this technology.

Numerous research efforts have indicated that the activity of Pt catalysts can be improved by alloying Pt with transition metals such as Fe, Co or Ni. [4-13] In recent studies we examined the extended surfaces of these alloys, and reported that the high activity originated from the modified electronic structures of Pt, which altered the adsorption of spectator species from the electrolyte and the binding energies of key reaction intermediates, and thus improved the reaction kinetics. [12-15] Despite the quest for more active systems, the stability of catalysts is less well investigated, with the exception of a few studies that have offered some promising directions. [3, 16, 17] It has also been reported that Pt surface sites with low coordination numbers, such as step edges, corners, kinks, and adatoms, are more vulnerable to dissolution than the atoms arranged in the long-range ordered (111) or (100) facets [18], as confirmed by scanning tunnelling microscopy (STM) studies combined with electrochemical and infrared characterizations of Pt single crystal surfaces covered with adsorbed CO. [19] In all cases it has been found that the adsorption of surface oxides takes place first on the low-coordinated Pt sites. Once formed, the rather strong Pt-oxide interaction induces substantial morphological changes of the topmost Pt layer, triggering the decay in fuel cell performance. Therefore, it becomes necessary to study the catalytically active materials on a more fundamental level in order to develop advanced catalysts with not only high activity, but also superior durability.

Considering that Pt-bimetallic materials have been extensively investigated it is plausible to propose that multimetallic systems could offer unprecedented benefits in catalysis by bringing together, in a controlled manner, highly diverse constituents that might be utilized to alter and tune not only catalytic properties, but the durability of the catalyst as well. Here we present an advanced catalyst based on multimetallic Au/FePt nanoparticles (NPs), which is catalytically active and highly durable for the ORR. The choice of elements was partially based on the recent reports of composite nanostructures for catalytic applications [20, 21], but more on our earlier studies of monodisperse Au NPs [22], Au single crystals modified with Pd thin films [23], and Pt-bimetallic alloys. [12, 13] The initial experiments were carried out on well-defined surfaces of binary Au(111)-Pt and ternary Au(111)-FePt systems. The obtained fundamental insight into the synergy between these materials has enabled us to resolve, define and utilize the exact role of each constituent in a ternary system. This has guided the synthesis of tailored NPs possessing favorable coordination of surface active sites, distribution of elements and amount of Pt in the system.

5.2 Results

Thin films of bimetallic $FePt_3$ (and/or Pt) were deposited in vacuum over a Au(111) substrate. The film thickness was chosen to be approximately five atomic layers in order to mimic the advanced catalytic properties of the nanosegregated concentration profile previously established for bulk Pt-bimetallic alloys. [12]
Figure 5.1 summarizes the results from the rotating disk electrode (RDE) measurements obtained for these thin films and demonstrates that, in accordance with the electrochemical properties of individual elements, addition of each of these metals induces extra functionality in the catalyst: ***i)*** Au is chemically stable in acidic electrolyte and electrochemically inactive for the ORR ($E > 0.6$ V). Au is also inert towards the adsorption/desorption processes of underpotentially deposited hydrogen H_{upd} (region I) and surface oxides OH_{ad} (region III, the potential range of interest for the ORR), although the latter is evident in region IV between $1.2 < E < 1.6$ V; ***ii)*** Pt is the only metal in this system that adsorbs underpotentially deposited hydrogen (H_{upd}) (region I) and is active for the ORR with respectable, but not satisfactory stability; ***iii)*** addition of Fe atoms in an alloy with Pt is known to induce catalytic enhancements for the ORR. [13]

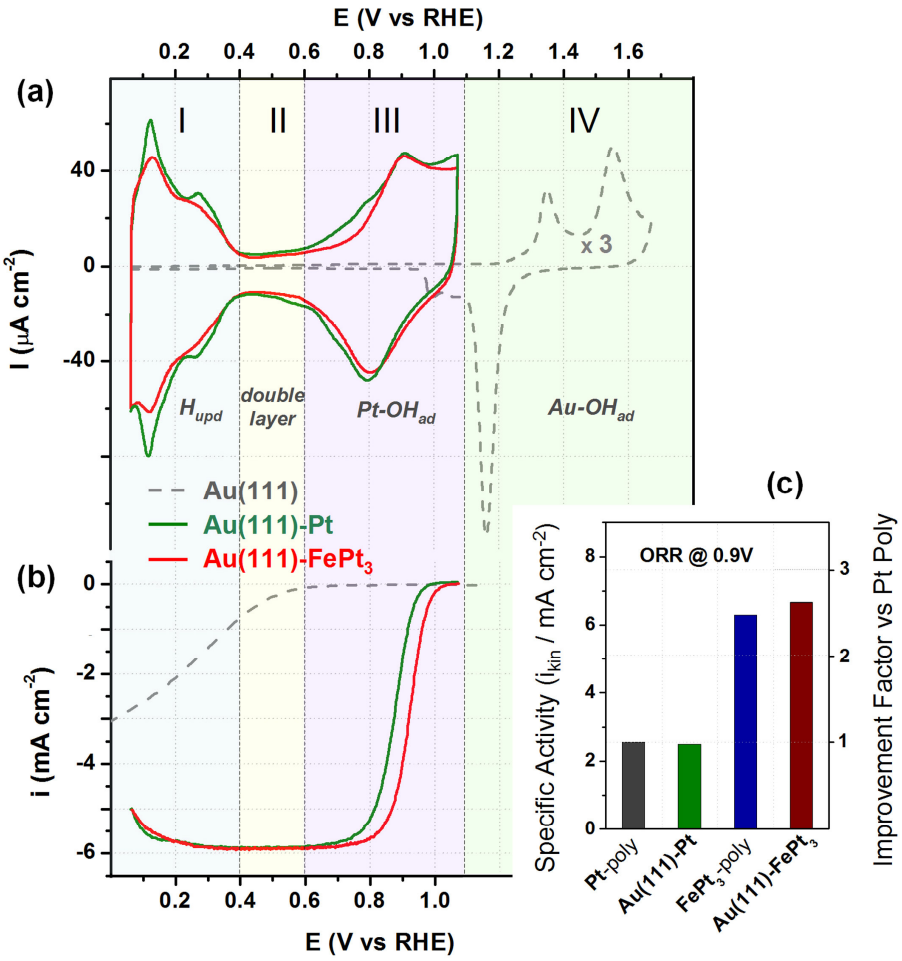

Figure 5.1. Electrochemical RDE characterization of Au(111) surface (gray) and Pt (green), $FePt_3$ (red) thin film surfaces supported on Au(111) substrate in 0.1M $HClO_4$: (a) cyclic voltammetries show that the onset of oxide adsorption on Au is positively shifted by more than 600 mV vs. Pt, indicating that Pt is much more oxophilic than Au; (b) polarization curves for the ORR at 1600 rpm and (c) summary of specific activities for the ORR@0.9 V vs. RHE, at 60°C with 1600 rpm with a sweep rate of 50 mV/s.

The voltammetries depicted in Figure 5.1a reveal that Pt is much more oxophilic than Au, which is clearly visible from the difference in the onset potential of oxide adsorption (a positive shift by 600 mV on Au vs. Pt demonstrates that Au is more difficult to be oxidized than Pt). The same figure also shows Pt-like behavior of the Au(111)-Pt and Au(111)-$FePt_3$ thin film surfaces with pronounced Pt-like H_{upd}

peaks (region I) as well as Pt-oxide adsorption/desorption peaks in the potential region III $0.6 < E < 1.1$ V. Moreover, the differences in voltammetry between Pt and $FePt_3$ thin film surfaces are clearly visible, *i.e.*, suppressed H_{upd} region and positive potential shift of the onset of surface oxide formation for Au(111)-$FePt_3$. [12, 13] Consequently, this is reflected by a considerably improved (~2.5 fold) specific catalytic activity for the ORR measured on the Au(111)-$FePt_3$ surface. There was no change in activity between Pt-poly and Au(111)-Pt electrodes, implying that the Au substrate does not alter the adsorption/electronic/catalytic properties of the outermost Pt atoms (figure 5.1b and 5.1c).

In addition to the improvement in activity, it was also found that the ternary system exhibited high stability during the electrochemical experiments (see section 5.7, figures 5.14-5.17). Prolonged electrochemical characterizations and measurements at extremely high overpotentials relevant for the oxygen evolution reaction have indicated the absence of Au atoms on the surface (Figure 5.18 and 5.19). Regardless of the temperature range (20 to 60^{o}C) or potential limit (which was as high as ~1.7 V versus the reversible hydrogen electrode, RHE), the surface did not suffer any change in composition. Based on the fundamental properties of Au and Pt, it is always expected to have diffusion of Au bulk atoms toward and over Pt surface atoms due to the difference in surface segregation energies. [24] However, this was not the case for Pt or Pt-bimetallic thin films on the Au substrate. These results provide important insights and show that the multimetallic system, comprised of a Pt/Pt-bimetallic surface layer over a Au substrate, is highly stable, despite the standard thermodynamic arguments mentioned above.

Several essential findings were obtained from the well-defined extended ternary systems such as: ***i*)** the multilayered Pt-bimetallic thin film could govern the catalytic properties to the same extent as in the case of bulk Pt-bimetallic systems; ***ii)*** the Au substrate could replace buried non-functional Pt atoms; ***iii*)** an electrochemically more inert Au substrate could facilitate the stabilization of the topmost Pt atoms. These findings were used as a guide in designing and synthesizing an advanced nanoscale electrocatalyst. In order to synthesize multimetallic NPs with the preferred surface coordination and concentration profile, we aimed toward shape-controlled Au NPs coated with a Pt-bimetallic alloy. [25-27]

5.3 Core shell particle synthesis and analysis

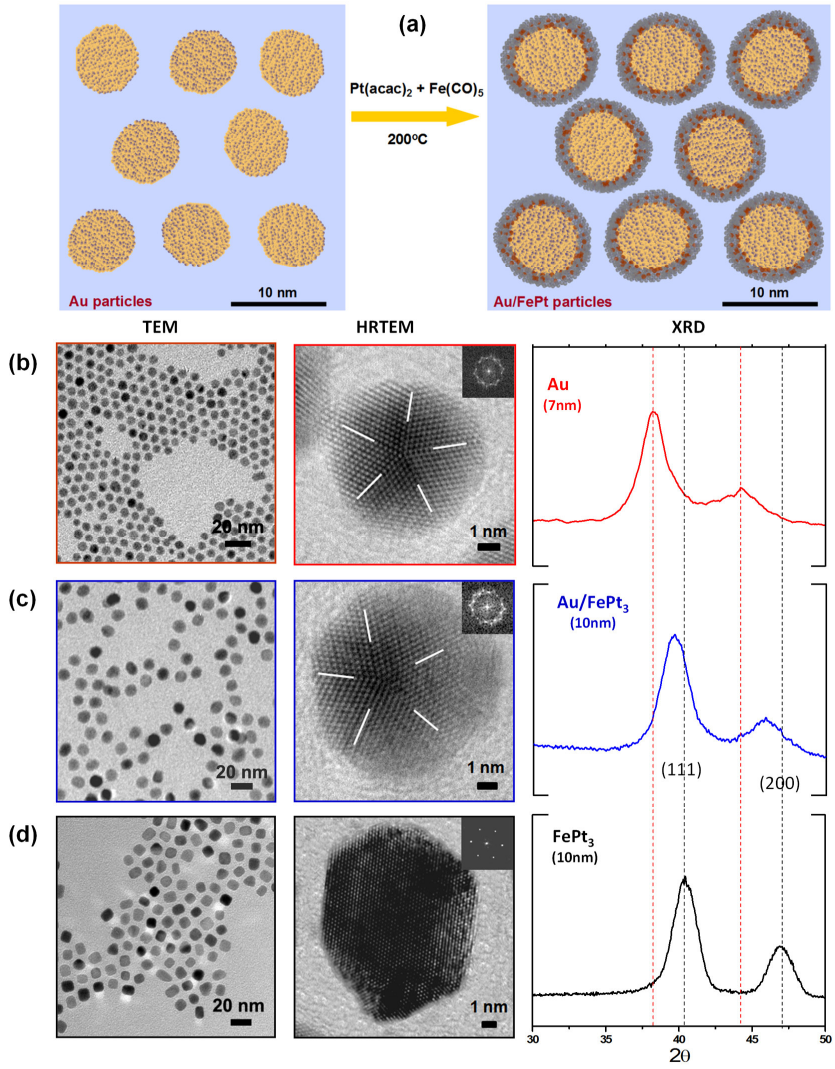

Figure 5.2. Synthesis and characterization of core/shell Au/$FePt_3$ NPs. (a) Schematic illustration of core/shell Au/$FePt_3$ NPs synthesis. TEM, HRTEM and XRD characterization of: (b) 7 nm Au, (c) 7/1.5 nm core/shell Au/$FePt_3$ NPs and (d) 10 nm $FePt_3$. The twinning boundaries for five-fold symmetry axes were marked by dash lines in the HRTEM images of Au and Au/$FePt_3$ NPs, where the insets show their respective fast Fourier transform (FFT) patterns with multi-fold symmetry clearly identified. The positions of (111) and (200) peaks for Au (red) and $FePt_3$ (black) are marked with dotted lines respectively in the XRD patterns.

Au NPs were prepared via the reduction of chloroauric acid ($HAuCl_4$) by *Tert*-butylamine-borane at room temperature [22], while epitaxial coating by $FePt_3$ was done by mixing Au NPs with platinum acetylacetonate, $Pt(acac)_2$, at 120°C in the presence of oleic acid and oleylamine, followed by adding $Fe(CO)_5$ and further growth at 200°C (Figure 5.2a). The molar ratio of $Fe(CO)_5$ to $Pt(acac)_2$ was adjusted to control the composition of the coating,[28] with a ratio of 0.8 : 1 giving Fe : Pt = 1 : 3 (Figure 5.12 and 5.20). Similar synthetic conditions without Au seeds were used to obtain Pt and $FePt_3$ NPs of the same size in order to eliminate particle size effect [29-32] in the following study. As-synthesized NPs were incorporated into carbon black (900 m^2/g), and the organic surfactants were removed by heating the NPs/carbon mixture in oxygen rich atmosphere.

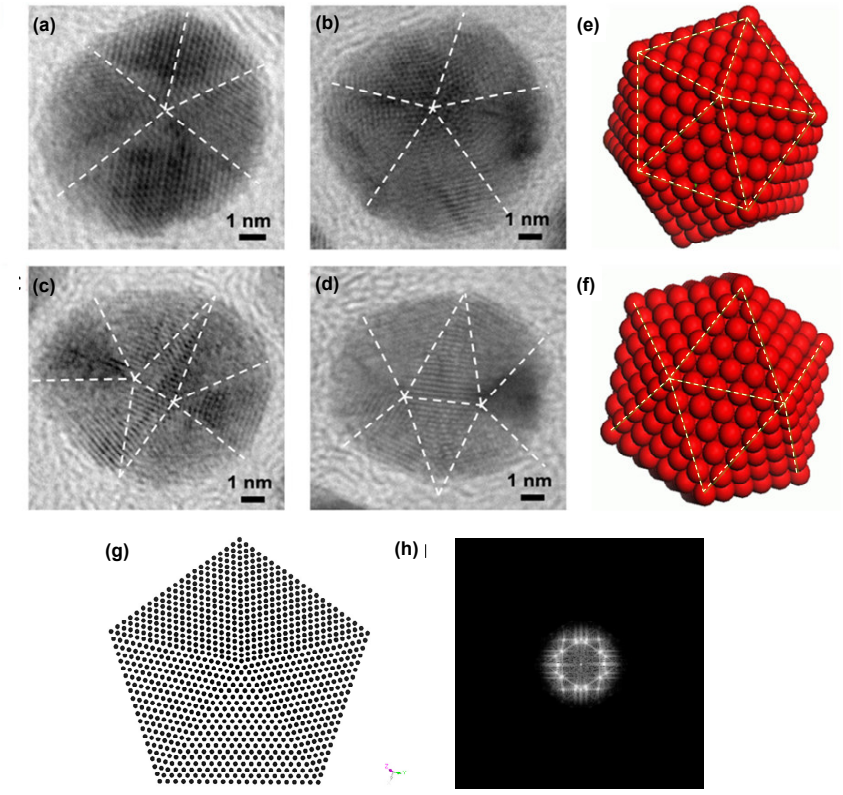

Figure 5.3. (a – d) Representative HRTEM images of icosahedral Au/$FePt_3$ NP viewed along different directions with (e, f) the corresponding orientation of model particles. (g) The arrangement of atoms extracted from the facets around a five-fold symmetry axis of an icosahedron and (h) its FFT pattern. The multi-fold symmetry in the FFT pattern can be comparable with those shown in Figure 5.2.

Figure 5.2 depicts the morphology, structure and size of the Au/$FePt_3$ NPs with the standard deviation in size distribution less than 5%. The average diameter of the monodisperse Au NPs increased from 7 to 10 nm after the $FePt_3$ coating (figure 5.2b), indicating that a 1.5 nm thick layer has been deposited over the Au seeding NPs (Figure 5.2c). High resolution TEM (HRTEM) images in figure 5.2 reveal substantial differences in morphology among the particles. The Au NPs possess an icosahedral shape [22] while the $FePt_3$ NPs have a cubo-octahedral shape that is typical for Pt and Pt-bimetallic NPs. From figure 5.2 it is also obvious that the icosahedron-like morphology of the Au seeds is retained after coating with the $FePt_3$, as evidenced by the presence of fivefold symmetry axis, which is considered to be the characteristic feature of this type of morphology (figure 5.2c and 5.3).[33-35]

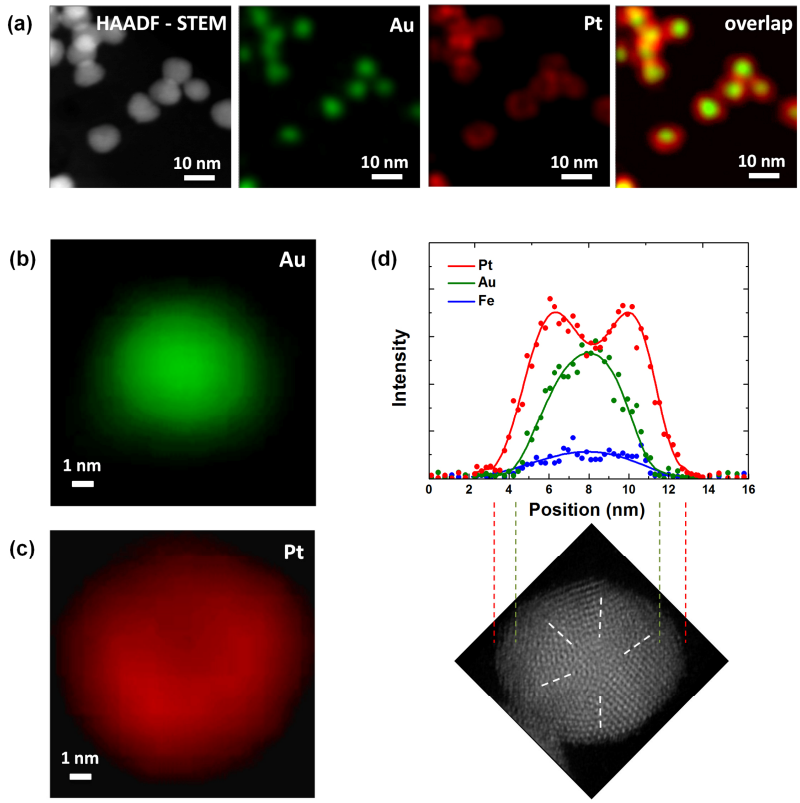

Figure 5.4. Elemental distribution analysis of core/shell Au/$FePt_3$ NPs: (a) HAADF-STEM characterization and elemental mapping of Au (green), Pt (red) and their overlap; (b), (c) the elemental maps of Au and Pt for a single core/shell particle and (d) line profile - elemental distribution along a single particle.

Although it is difficult to distinguish Au from Pt in HRTEM images (figure 5.2c) due to the negligible contrast between these two elements, the concentration profile of multimetallic particles was established by elemental analysis carried out by scanning transmission electron microscopy (STEM). Figure 5.4a shows the high angle annular dark field (HAADF) STEM image and elemental mapping of Au and Pt in the NPs, indicating that Au (green) is surrounded by Pt (red) (additional images are given in figure 5.5; however, the signal for Fe is rather weak and mapping of Fe is statistically challenged). Figure 5.4b and 5.4c present elemental mapping of Pt and Au in a single ~10 nm NP, while figure 5.4d shows the line profiles for all three elements obtained by scanning e-beam across the NP. It can be seen that the Au peak (green line) is about 3 nm narrower than the Pt peak (red line), confirming the coating thickness of about 1.5 nm.

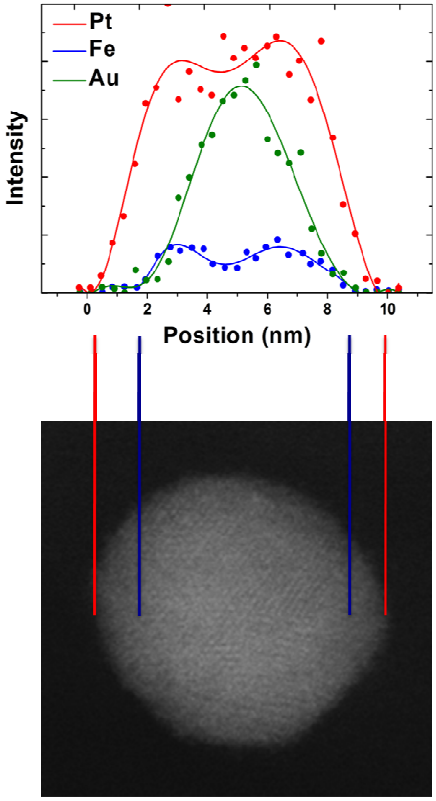

Figure 5.5. More images for element mapping of Au/$FePt_3$ NP by HAADF-STEM. The concentration profile is clearly seen by the overlapping image (left) of Pt and Au. Below, additional line profile is given for a single Au/$FePt_3$ particle that reveals the coating thickens and its concentration profile.

The concentration profile was also verified by the structural and optical characterizations of the Au/$FePt_3$ NPs. The X-ray diffraction (XRD) patterns of the Au seeds, Au/$FePt_3$ and $FePt_3$ NPs have typical peaks of fcc crystals (Figure 5.2 and S11). By taking a close view of the XRD patterns, we find that the (111) peak of Au/$FePt_3$ NPs is downshifted compared to that of $FePt_3$ NPs, and the spacing between the adjacent (111) planes are calculated to be 0.235 nm, 0.227 nm and 0.223 nm for Au, Au/$FePt_3$ and $FePt_3$ NPs respectively according to Bragg's law. A similar trend can also be established for (200) and other peaks. This observation implies that the average Pt-Pt bonding length in the Au/$FePt_3$ NPs is slightly larger than that in $FePt_3$ NPs. Such an increase of metallic bonding radius in the coated $FePt_3$ could originate from alloying at the Au/$FePt_3$ interface where no clear boundary exists and an intermixed phase is formed between Au and $FePt_3$ (which has also been confirmed by HAADF STEM analyses, figure 5.8). Additionally, optical properties of Au/$FePt_3$ NPs were investigated by UV-Vis spectroscopy (figure 5.6). The 7 nm Au NPs have a strong surface plasmonic absorption peak at 520 nm. [36] In contrast, the Au/$FePt_3$ NPs show a featureless spectrum similar to the $FePt_3$ NPs. This, plus the elemental analysis, proves that the Au seeds are entirely coated by $FePt_3$ in the multimetallic NPs.

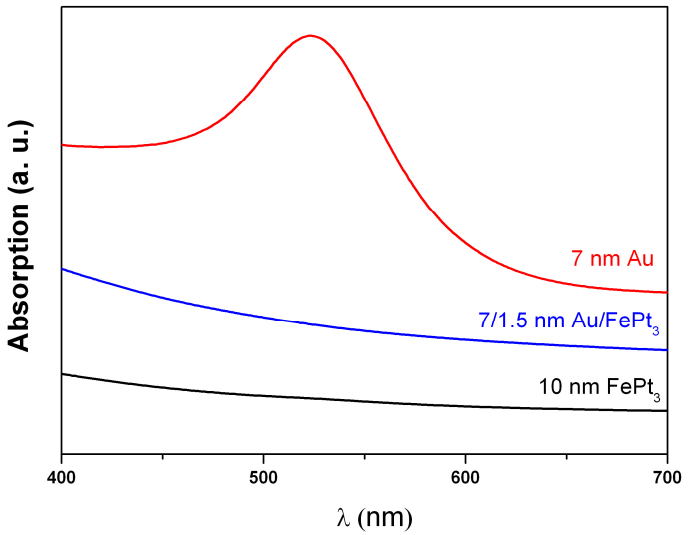

Figure 5.6. UV-vis spectra of Au/$FePt_3$ and Au NPs dispersed in hexane. 7 nm Au NPs show a surface plasmon resonance peak around 520 nm, but Au/$FePt_3$ NPs have no visible feature in the UV-vis spectrum (just like $FePt_3$ NPs). This confirms that the Au seeds were entirely coated by $FePt_3$, and no Au atoms are present on the surface of multimetallic particles.

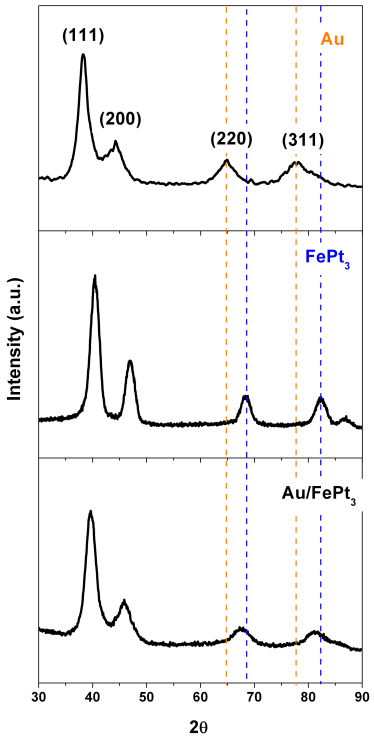

Figure 5.7. Whole range of XRD patterns for Au, $FePt_3$, and Au/$FePt_3$ NPs. In addition to (111) and (200) peaks shown in Figure 5.2, shift for high-angle peaks (220) and (311) are marked here (dashed lines: orange for Au, and blue for $FePt_3$). Particularly, the pattern for Au/$FePt_3$ NPs shows no extra peak at the positions of Au (220) and Au (311) peaks, indicating neither free Au nor dimmer-like Au-$FePt_3$ NPs exist after coating.

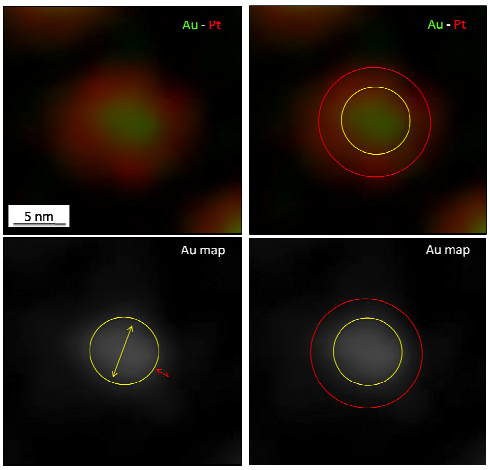

Figure 5.8. HAADF-STEM analysis of the interfacial alloying in the Au/$FePt_3$ NPs. The Au map shows ~5nm core of pure Au (yellow) and ~1 nm thick layer of mixed Au-Pt-Fe (red).

5.4 Electrochemical characterization

Electrochemical characterization of the NPs was done by RDE with a glassy carbon disk (figure 5.9). Based on the cyclic voltammetries obtained for different catalysts the Au/$FePt_3$ behaves just like Pt and $FePt_3$ NPs, indicating that the multimetallic particles have a Pt-rich surface. The catalytic performance of Au/$FePt_3$/C for the ORR is similar to its bimetallic counterpart $FePt_3$/C, with an improvement factor of > 3 versus Pt/C catalyst, which is consistent with the results measured on well-defined extended surfaces. Additional insights for the Au/$FePt_3$/C NPs were obtained from the electrochemical CO oxidation and cyclic voltammetry by opening potential up to 1.7 V (figure 5.21). A perfect match between H_{upd} and CO stripping charge combined with the absence of Au redox peaks at 1.35 and 1.15 V prove that there is no presence of Au atoms on the surface of the multimetallic particles. The electrochemical results indicate that a highly efficient chemical coating of the Au substrate has produced a homogeneous layer of the Pt-bimetallic alloy without Au atoms in the topmost surface layer.

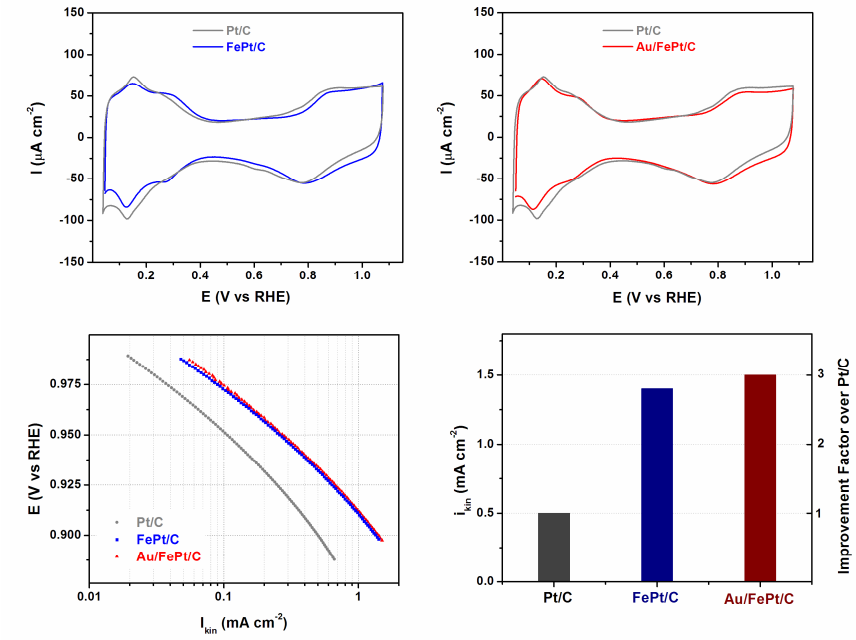

Figure 5.9. Electrochemical RDE characterization of Pt/C (grey), FePt3/C (blue) and Au/FePt3/C (red) catalysts in 0.1M HClO4: (a), (b) cyclic voltammetries, (c) specific activities at 1600 rpm for the ORR at different electrode potentials (Tafel plot) and (d) summary of specific activities for the ORR@0.9 V vs. RHE, at 60oC with 1600 rpm with a sweep rate of 20 mV/s.

The most vital feedback from the electrochemical characterization has been obtained from the durability measurements. These experiments were designed to imitate the operating conditions of fuel cells and were carried out by cycling the potential between 0.6 V and 1.1 V (versus RHE) in an oxygen saturated electrolyte. Figure 5.10a-c shows the summary of the electrochemical properties of Au/$FePt_3$/C compared with Pt/C and $FePt_3$/C before and after 60,000 potential cycles. No significant loss in surface area or specific activity was observed for Au/$FePt_3$/C, in contrast to $FePt_3$/C and Pt/C. Of particular note is that the initial specific activity of the Au/$FePt_3$/C catalyst was as high as that of $FePt_3$/C, but after the potential cycling the activity of $FePt_3$/C dropped much more than the activity of Au/$FePt_3$/C did. After the potential cycling the multimetallic catalyst has 7 times higher specific activity, and more than one order of magnitude higher mass activity than Pt/C.

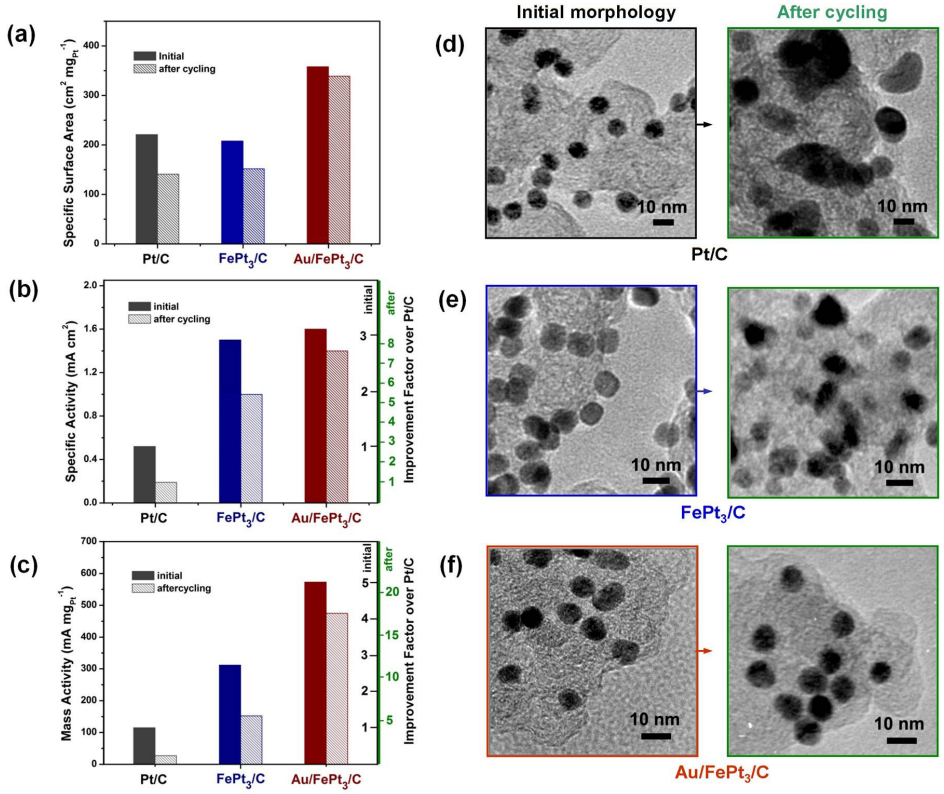

Figure 5.10. Stability characterization of the Pt/C, $FePt_3$/C and Au/$FePt_3$/C catalysts by 60,000 potential cycles between 0.6 V and 1.1 V vs. RHE in oxygen saturated 0.1 M $HClO_4$ electrolyte at 20°C with a sweep rate of 50 mV/s: (a-c) Summary of the specific surface area, specific and mass activities and (d-f) TEM characterization of the catalysts before and after the potential cycling.

In order to understand the enhanced stability of Au/FePt/C catalyst and get detailed insight into the degradation mechanism, TEM characterization was performed before and after the stability studies (figure 5.10d-f). No observable change can be seen for Au/$FePt_3$ NPs before and after the 60,000 potential cycles, neither in size nor shape (figure 5.10f and TEM images in figure 5.11). However, after the potential cycles, the size of Pt and $FePt_3$ NPs has been substantially changed (Figure 5.10d and 5.10e). Big particles of over 20 nm in diameter are formed, due to the Pt instability and well-known phenomena of Ostwald ripening during electrochemical cycling. [3] These results provide remarkable evidence for the devastating morphology changes suffered by $FePt_3$/C and Pt/C catalysts, which have had a direct influence on the decay in catalyst performance. On the contrary, the multimetallic Au/$FePt_3$ NPs do not suffer from any obvious change in morphology or performance, and represent a highly durable electrocatalyst for the ORR.

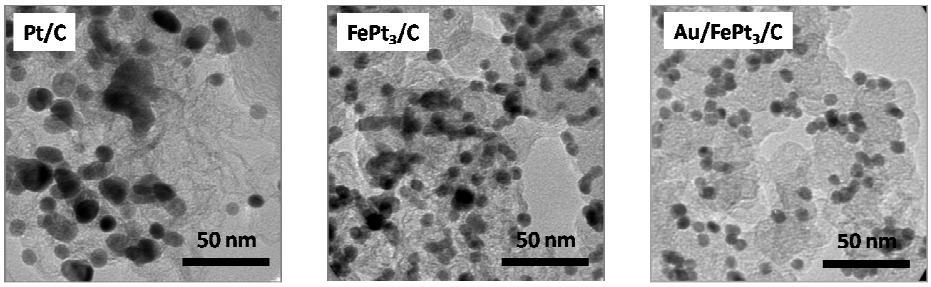

Figure 5.11. TEM images of the three catalysts after the stability test of 60,000 cycles from 0.6V to 1.1V vs. RHE. In the case of Au/$FePt_3$/C, though some NPs stack together, they can still be individually distinguished from each other.

5.5 Discussion

Since the catalytic activity of Au/$FePt_3$/C is at the same level as that for $FePt_3$/C, it is not likely that the Au core directly affects the electronic/adsorption/catalytic properties of the surface Pt atoms. This is consistent with what we observed in thin films, *i.e.*, the activity of a Au(111)-Pt surface did not differ from that of a Pt-poly surface, suggesting unchanged electronic properties of the topmost Pt atoms. For that reason, the mechanism of stability improvement observed in the Au/$FePt_3$ system should be considered as being due to the synergy between the particle morphology and its unique concentration profile. Thus it is plausible to propose that

the Au core plays a key role in the durability enhancement while the topmost Pt atoms, electronically altered by the subsurface Fe, provide the high catalytic activity.

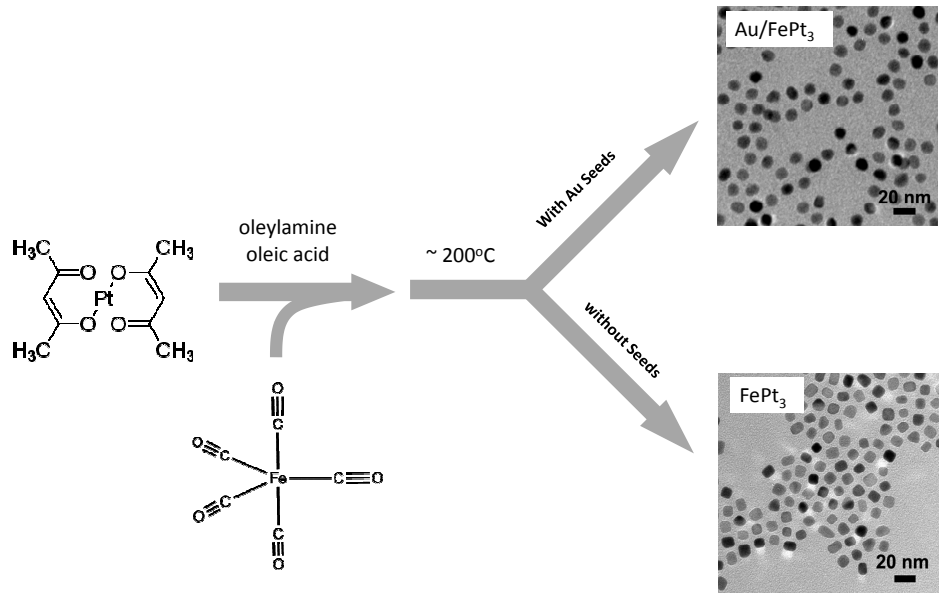

Figure 5.12. Scheme of Au/$FePt_3$ NP synthesis. $Pt(acac)_2$ was thermally reduced by oleylamine to Pt, and simultaneously $Fe(CO)_5$ decomposed to Fe. Pt and Fe nucleated (coated) over Au seeds into Au/$FePt_3$ NPs. In the absence of Au seeds, $FePt_3$ NPs can grow under the same synthetic conditions and size can be controlled.

As discussed above, we have demonstrated the control of morphology through seed-mediated growth using the distinctive icosahedral Au seeds; direct synthesis without Au seeds produced $FePt_3$ NPs of cubo-octahedral shape (figure 5.12), the most common morphology for Pt and Pt-bimetallic catalysts reported in the literature.

Considering that surface atom solubility is highly dependent on its coordination number (the number of nearest neighbors) [18, 29, 37], the low-coordinated atoms are more sensitive to oxidation and dissolution in electrochemical environments. [18, 19] In particular, an atom on a (111) facet has a coordination number of 9, versus 8 for (100) facets, 7 for edge sites and 6 for corner sites on a cubo-octahedral particle (figure 5.13). Correspondingly, the spatial arrangement of the topmost atoms in an icosahedron-like particle would diminish the number of low-coordinated surface sites and increase surface average coordination number compared to cubo-octahedral particles (figure 5.13 and 5.22), *e.g.*, 12 atoms with

the coordination number of 6 on an icosahedron vs. 24 on a cubo-octehedron. Therefore, it is reasonable to expect that the surface atoms of an icosahedron-like Au/$FePt_3$ NPs are less vulnerable to dissolution than those of cubo-octahedral $FePt_3$ NPs, thus enhancing the durability of the multimetallic catalyst.

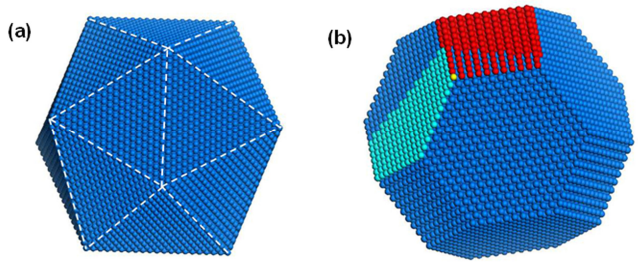

Figure 5.13. The detailed analysis of the coordination number distribution of Pt surafce atoms of a 10 nm NP in (a) icosahedral or (b) cuboocahedral shape. There are 29881 atoms in the cubo-octahedral NP, and 28741 atoms in the icosahedral NP. Stastical results (listed in section 5.7) show that the surface of icosahedron has higher average coordination number than that of cubo-octahedron.

In accordance with surface segregation energies in transition metals [38], a gold enriched surface would be expected in this system. However, no trace of surface Au was found from elemental mapping and electrochemical measurements, signifying that the stable topmost layer consists of Pt atoms only, while interfacial alloying between the Au core and the Pt-bimetallic shell might occur in the subsurface layers. A similar divergence in surface composition from the thermodynamically favorable state was also reported for Rh/Pd core/shell NPs, and it was found to be strongly dependent on the nature of the reactive environment. [24] For the given electrochemical conditions, apparently Pt is easier to be oxidized than Au (figure 5.1), which provides the driving force for Pt atoms to stay on the surface in a highly oxophilic environment. Therefore, we propose here that the counterbalance between the two opposing forces; the rather strong interaction between Pt and surface oxides on one side, and the tendency of Au to segregate over Pt on the other side, have induced another beneficial stabilization mechanism of the topmost Pt layer (figure 5.23 and 5.24). It turns out that these two opposing energetic driving forces are of comparable magnitude, according to first-principles calculations. In particular, the surface-adsorbed O or OH groups, in proximity to Au atoms (for example, at sufficiently high O coverages), can reverse the thermodynamic driving force for Au to segregate to the surface of a Pt lattice. In effect, as discussed above,

the energetic preference for Au to be on the surface of Pt in vacuum is cancelled out by the reduced affinity of Au for adsorbed oxygen containing species. These results, in turn, imply that Au will remain below the Pt surface during electrochemical operation at potentials sufficiently high to cause adsorption of oxygen containing species. Thus, the adsorbate-induced segregation has led to the formation of a Pt-skin layer, which is electronically/catalytically altered by subsurface Fe while stabilized by subsurface Au.

The existence of subsurface Au atoms makes an additional contribution to the durability enhancement of the Pt skin layer by modifying the well-known place-exchange mechanism.[18, 39] This mechanism operates for Pt at electrode potentials relevant to the ORR and involves migration of atomic oxygen from surface to subsurface positions. Place-exchange is considered to be one of the precursors for Pt dissolution, yet in the case of Au/$FePt_3$ particles it is effectively hindered due to the presence of Au atoms in subsurface layers, i.e., Au cannot be oxidized in the given potential range that is relevant for the ORR (see figure 5.1a, potential regions III and IV), and therefore, occurrence of Au in the subsurface layers would make the formation of subsurface oxides less energetically favorable and hence suppress the dissolution of Pt (Figure 5.25). Supplementary evidence in support of this mechanism has been obtained through a Density Functional Theory (DFT) model of subsurface atomic oxygen adsorption in $FePt_3$(111) alloys (figure 5.26). When a Au atom is substituted for Pt in the subsurface layer, the strength of subsurface oxygen binding decreases in magnitude by about 0.15 eV. This decrease is expected to make oxygen place exchange thermodynamically less feasible, thereby reducing Pt loss in the ternary system under this well-known Pt-dissolution mechanism.

Although there is the effect of particle morphology and surface coordination, we believe that the unique compositional profile of Au/$FePt_3$ NPs should be the dominant factor contributing to the observed durability enhancement, as it alternates the energetics and kinetics related to the dissolution processes of Pt in the electrochemical environments, which is revealed by our first-principle theoretical studies. The proposed durability enhancement in this study is quite unique, and differs from the recent report in which Au nanoclusters were deposited on Pt particle surface. [16] In that case the stability enhancement was assigned to the raised oxidation potential of Pt by Au. In contrast, the ternary catalyst described here does not suffer any loss of Pt active sites due to the presence of surface Au clusters and thus provides highly efficient utilization of Pt. The fine balance among the key factors such as the proper order of synthesis steps, stoichiometric ratio

between the elements, and the temperature for FePt overgrowth have enabled the formation of NPs with controlled shape, size, and composition profile, which do not only preserve the beneficial catalytic properties of Pt-bimetallic alloy surfaces, but also exhibit superior durability performance by using a minimal amount of Pt in the system. Most significantly, the dramatic activity enhancement is illuminated by the improvement factors of over 7 in specific activity and more than one order of magnitude in mass activity for Au/$FePt_3$/C versus Pt/C after extensive potential cycling.

5.6 Summary

In summary, we have developed a synergistic approach toward advanced fuel-cell catalysts by combining the studies of well-defined surfaces and nanomaterial synthesis. Based on the knowledge gained from FePt thin films deposited on Au single-crystal substrates, tailored Au/Pt-bimetallic nanoparticles have been designed and synthesized by an organic solvothermal method. The morphology control and preferred composition profile were achieved through epitaxial growth of Pt-bimetallic alloy over Au seeds. Compared to $FePt_3$/C and Pt/C, the multimetallic Au/$FePt_3$ catalyst showed superior durability while preserving the beneficial catalytic activity of Pt-bimetallic alloys. This work reveals the great potential of utilizing multimetallic nanostructures in tuning the catalytic and durability properties of nanocatalysts. The developed synergistic strategy reported here could also be generalized to connect fundamental studies and novel nanomaterial synthesis for advanced catalytic and other applications.

5.7 Appendix

5.7.1 Part 1 Experimental Methods and Characterizations

5.7.1.1 Nanoparticle Synthesis

5.7.1.1.1 7 nm Au NPs

A solution of 10 ml 1,2,3,4-Tetrahydronaphthalene (tetralin, anhydrous 99%, Sigma-Aldrich), 10 ml oleylamine (70%, Sigma-Aldrich), and 0.1 g $HAuCl_4 \cdot 3H_2O$ (99.9985%-Au, Strem) was prepared in air at 15°C and magnetically stirred under N_2 flow. 0.5 mmol of Tert-butylamine-borane (97%, Sigma-Aldrich) complex was dissolved in tetralin (1 mL) and oleylamine (1 mL) and injected into the precursor solution. The reaction initiated instantaneously and the solution changed to a deep purple color within 5 s. The mixture was allowed to be aged at 15^{o}C for 1 h before 60 ml acetone (ACS grade, BDH) was added to precipitate the Au NPs. The Au NPs were collected by centrifugation (8500 rpm, 8 min), washed with acetone and redispersed in hexane (ACS grade, BDH).

5.7.1.1.2 7/1.5 nm Au/FePt3 NPs

30 mg of 7 nm Au NPs were mixed with 10 ml octadecene (90%, Sigma-Aldrich), 0.1 g $Pt(acac)_2$ (98%, Strem), 1 ml oleylamine and 1 ml oleic acid (90%, Sigma-Aldrich) at 120^{o}C. 0.03 ml $Fe(CO)_5$ (99.5%, Strem) was added under N_2 atmosphere, then the temperature was raised to 200^{o}C. The solution was cooled down to room temperature after 30 minutes. 50 ml iso-propanol (99.5%, Sigma-Aldrich) was added to precipitate the NPs and the product was collected by centrifuge (6000 rpm, 5 min). The obtained Au/$FePt_3$ NPs were washed with ethanol (denatured ACS grade, BDH) and redispersed in hexane. Similar recipe without adding Au seeds was used to synthesize 10 nm $FePt_3$ NPs. Synthesized NPs were incorporated into carbon black (900 m^2/g), and the organic surfactants were removed by heating the NPs/carbon mixture in oxygen rich atmosphere. Total metal loading was adjusted to be 20% for all catalysts used in this work.

5.7.1.2 Material Characterizations

TEM images were collected on a Philips EM 420 (120 kV). HRTEM images were recorded using a Jeol JEM-2010 (200 kV). XRD patterns of the particle assemblies were collected on a Bruker AXS D8-Advance diffractometer with Cu Kα radiation (λ = 1.5418 Å). UV/vis spectra were recorded on a Perkin Elmer Lambda 35 spectrometer. STEM and elemental analysis were carried out on FEI Tecnai F20ST analytical electron microscopy at Argonne National Laboratory. Additional analyses were done with JEOL 2200FS TEM/STEM at Oak Ridge National Laboratory equipped with a CEOS aberration (probe) corrector. The microscope was operated at 200kV in high angle annual dark field (HAADF) scanning transmission electron microscopy (STEM) mode. The probe size was ~0.7Å and probe current was ~30pA during HAADF-STEM imaging. When accumulating EDS data, to increase probe current to ~400-500pA, the probe size was ~2Å. A Bruker-AXS X-Flash 5030 silicon drift detector was the EDS system.

5.7.1.3 Electrochemical Study

The catalysts were dispersed in deionized water (double-filtered, Milli-Q, $\rho \geq$ 18.2 MΩ cm) by sonication. A drop of the catalyst suspensions was deposited onto a glassy carbon disk (6 mm in diameter) and dried in Ar stream. The Pt loading was 15 ug/cm^2 (Pt/disk) in all cases. All cyclic voltammograms and polarization curves were recorded with sweep rates of 20 and 50 mV/s using an Autolab 302 electrochemical analyzer. 0.1 M perchloric acid (prepared by diluting ultra pure perchloric acid (70%, OmniTrace Ultra™, EMD) with deionized water) was used as the electrolyte. The prolonged potential cycling was done at 20^{o}C in order to diminish the influence of contaminants and electrolyte evaporation, which could be significant at elevated temperatures. All potentials are given versus reversible hydrogen electrode (RHE).

5.7.1.4 Theory and Simulations

The DACAPO code [40] was used for all total energy calculations in this study. A four-layer slab, periodically repeated in a super cell geometry with six equivalent layers of vacuum between any two successive metal slabs, was used; the RPBE [40]-optimized Pt_3Fe lattice constant is 3.96 Å. A (2x2) unit cell was employed. The top two layers of the slab were allowed to relax until the total force on all atoms was less than 0.04 eV/Å in any Cartesian direction. Adsorption was allowed on one of the two exposed surfaces

of the metal slabs, and the electrostatic potential was adjusted accordingly [41]. Ionic cores were described by ultrasoft pseudopotentials [42], and the Kohn-Sham one-electron valence states were expanded in a basis of plane waves with kinetic energy below 340 eV; a density cutoff of 500 eV was used. The surface Brillouin zone was sampled with an 18 Chadi-Cohen **k** point grid. The convergence of the total energy with respect to the cut-off energies and the **k** point set was confirmed. The exchange-correlation energy and potential were described by the generalized gradient approximation (GGA-RPBE) [42]. The self-consistent RPBE density was determined by iterative diagonalization of the Kohn-Sham Hamiltonian, Fermi population of the Kohn-Sham states (k_BT = 0.1 eV), and Pulay mixing of the resulting electronic density [43]. All total energies were extrapolated to k_BT = 0 eV.

5.7.2 Part 2 Electrochemical Properties of Well-Defined Surfaces

5.7.2.1 Electrochemical characterization of Pt and $FePt_3$ thin films on Au(111) substrate

5.7.2.1.1 Au(111)-Pt

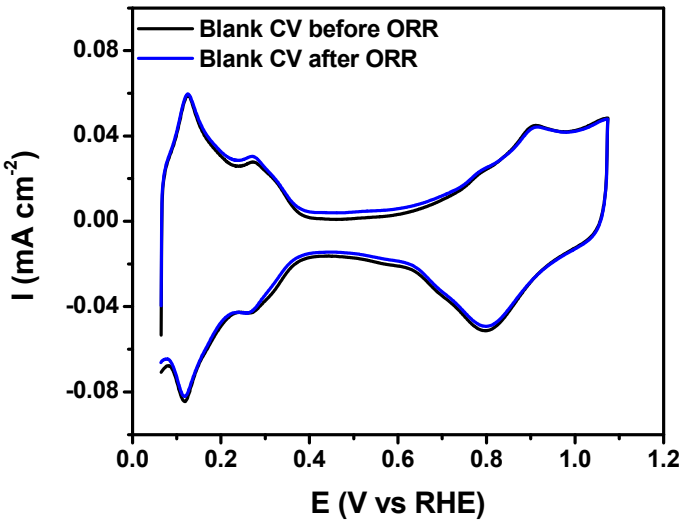

Figure 5.14. Blank CV for 1.5 nm Pt thin film supported on Au(111) before (black), and after (blue) ORR measurements at 20 and 60°C. The integrated charge of H_{upd} is found to be 210 μCcm^{-2}, which is equal to the expected value for polycrystalline Pt surface.

The cyclic voltammogram of the Au(111)-Pt surface in Ar saturated electrolyte is identical before and after the ORR experiments. No change in integrated charge of underpotentially deposited hydrogen (H_{upd}) demonstrates stable behavior of Pt atoms on the Au substrate, confirming that the surface composition stays the same.
Electro-oxidation of the fully covered CO adlayer over Au(111)-Pt surface revealed that the integrated charge from the CO stripping peak of 420 μCcm^{-2} matches the surface area obtained from H_{upd}. That was additional confirmation that surface was fully covered with Pt atoms. In addition, cyclic voltammetry does not change before and after experiments with CO indicating that the surface composition is not affected.

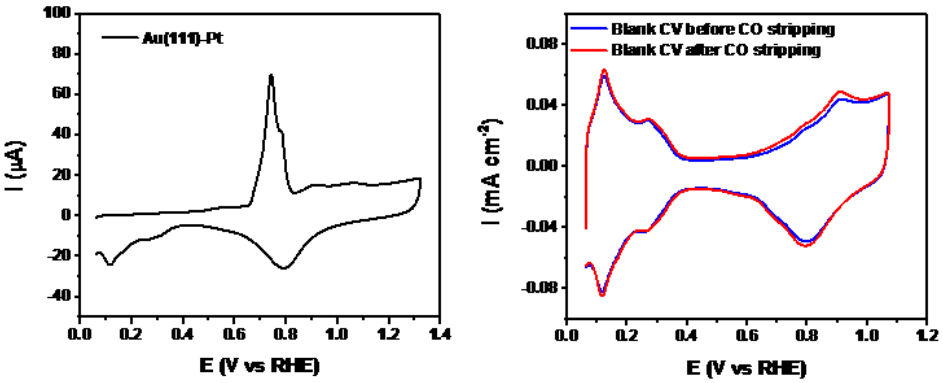

Figure 5.15. (a) CO stripping performed on Au(111)-Pt thin film. The integrated charge of CO stripping is 420 μCcm^{-2}, which is a perfect match with expected value for polycrystalline Pt. (b) Blank CV measured before (blue) and after (red) CO stripping. They are similar to each other, and the H_{upd} region is identical showing no reduction in exposed Pt surface area.

5.7.2.1.2 Au(111)-$FePt_3$

Cyclic voltammetry of Au(111)-$FePt_3$ in Ar saturated electrolyte does not change before and after the ORR experiments, Figure 5.16. The H_{upd} features are broader than in the Au(111)-Pt thin film, with the integrated charge density of 180 μCcm^{-2}, which is lower than that of Au(111)-Pt. This fits with previous results obtained on bulk alloys [13] in which the H_{upd} region of Pt-bimetallic alloy surfaces was found to be lower than that of polycrystalline Pt. Additionally, no change in integrated charge of H_{upd} demonstrates stable behavior of Pt atoms on the Au substrate, confirming that surface composition of Pt-bimetallic thin film stays the same.

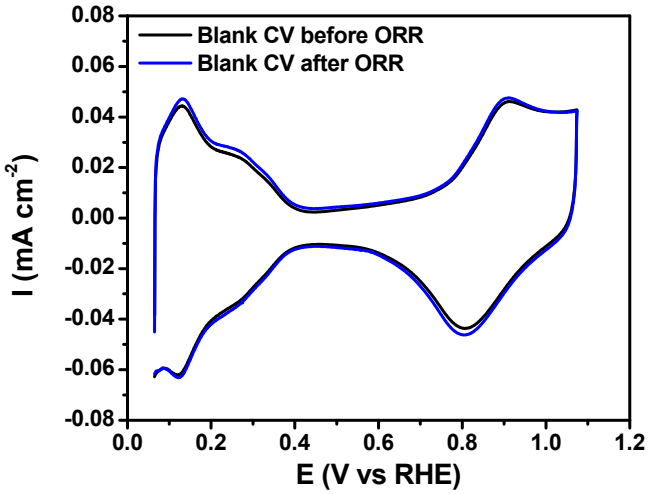

Figure 5.16. Blank CV for Au(111)-$FePt_3$ thin film before (black) and after (blue) ORR measurements at 20 and 60°C. Similar to the Pt film on gold, from the absence of change in H_{upd} area it can be determined that there was no loss of Pt surface area during measurement of the ORR.

Electro-oxidation of a fully covered CO adlayer on the Au(111)-$FePt_3$ surface revealed that the integrated charge from the CO stripping peak of 420 μCcm^{-2} matches the surface area obtained from Au(111)-Pt and polycrystalline Pt surfaces. The difference between the integrated charges for H_{upd} and CO stripping originates from altered electronic properties of the Pt topmost atoms. Due to changed electronic/adsorption properties [13] only the total charge of H_{upd} is affected - decreased with about 30 μCcm^{-2}, while total coverage of CO_{ad} due to strong Pt-CO interaction remains the same as in the case of pure Pt surfaces. This is additional confirmation that the Pt-bimetallic thin film completely covered the geometric surface area of the Au(111) substrate. In addition, cyclic votammetry does not change before and after experiments with CO, indicating that the surface coverage of Pt atoms stays the same.

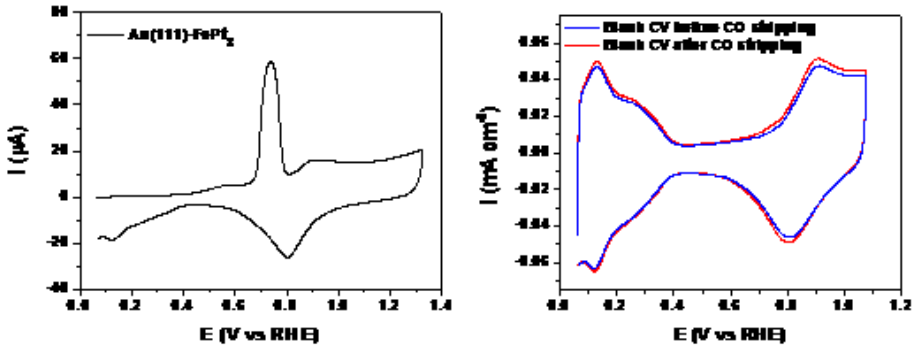

Figure 5.17. (a) CO stripping performed on Au(111)-FePt3 thin film, showing a single CO stripping feature. The integrated charge of CO stripping is 420 μCcm-2, equal to the values obtained on Au(111)-Pt and polycrystalline Pt. (b) Blank CVs measured before and after CO stripping show that the Hupd region is identical without reduction in exposed Pt surface area.

5.7.2.1.3 The absence of Au atoms on the Au(111)-$FePt_3$ surface

Figure 5.1 summarizes the electrochemical characterization of well-defined extended thin film surfaces on the Au(111) substrate. From this summary it is obvious that, in accordance with the electrochemical property of the individual elements, addition of each of these metals induces extra functionality in the catalyst. In addition, the Au surface atoms are chemically stable in acidic electrolyte and inert towards the adsorption/desorption processes of H_{upd} (region I), while reversible adsorption/desorption of surface oxides is evident in the region IV between $1.1 < E < 1.6$ V. This redox couple at 1.35 V and 1.15 V could be effectively used as a signature for the presence of Au surface atoms. In order to make a systematic electrochemical analysis of these thin film surfaces, we extended the potential window up to 1.65 V vs. reversible hydrogen potential. In figure 5.18, a voltammogram of Au(111)-$FePt_3$ is shown, which was recorded in the extended potential region. No detectable peaks that would indicate the presence of Au were found.

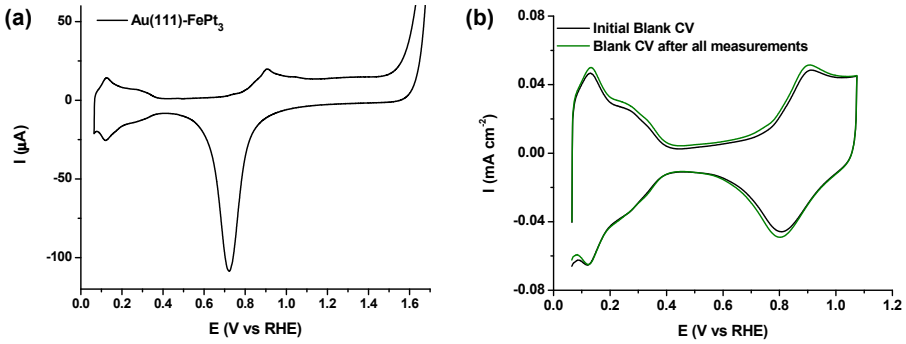

Figure 5.18. (a) CV for Au(111)-$FePt_3$ thin film with 1.5 nm thickness by opening the potential to 1.65V. The CV does not show characteristic features for the presence of surface Au. (b) Comparison of CVs before (black curve) and after (green curve) ORR at 20 and 60°C, CO stripping and increasing the upper potential limit measurements.

In addition, comparison between CVs (figure 5.18b) before and after the whole series of electrochemical measurements, such as ORR at 20 and 60°C, CO stripping and measurements in an extended potential range up to 1.65 V, confirms that during the course of the measurements the H_{upd} area has not changed and the thin Pt-bimetallic film remains stable without noticeable change in surface composition.

In order to demonstrate that Au surface atoms could be detected if they are exposed to the electrolyte we performed electrochemical measurements with a different film thickness. Based on these results it was possible to conclude that surfaces of $FePt_3$ films that are thinner than 1 nm have some Au atoms on the surface. This is clearly visible from the cyclic voltammetry in figure 5.19, where the Au oxidation is clearly visible, indicating the presence of Au surface atoms. From the integrated H_{upd} charge of 170 μCcm^{-2} it was estimated that the Au surface composition was about 5%. This example confirms that this methodology can be efficiently used to detect Au surface atoms.

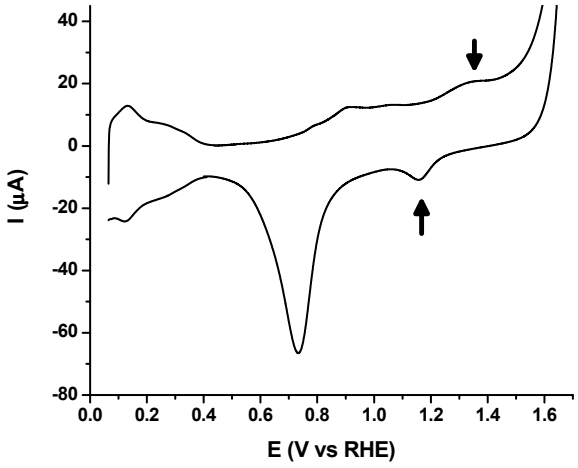

Figure 5.19. CV for Au(111)-$FePt_3$ thin film of <1 nm by opening the potential to 1.65V. It shows clearly that, in contradictory to Au(111)-$FePt_3$ thin film of 1.5 nm shown above, some gold is exposed on the surface as seen by the Au-OH_{ad} redox couple at 1.35V and 1.15 V.

5.7.3 Part 3 Properties of Multimetallic Nanoparticles

5.7.3.1 Elemental analysis of Au/$FePt_3$ nanoparticles:

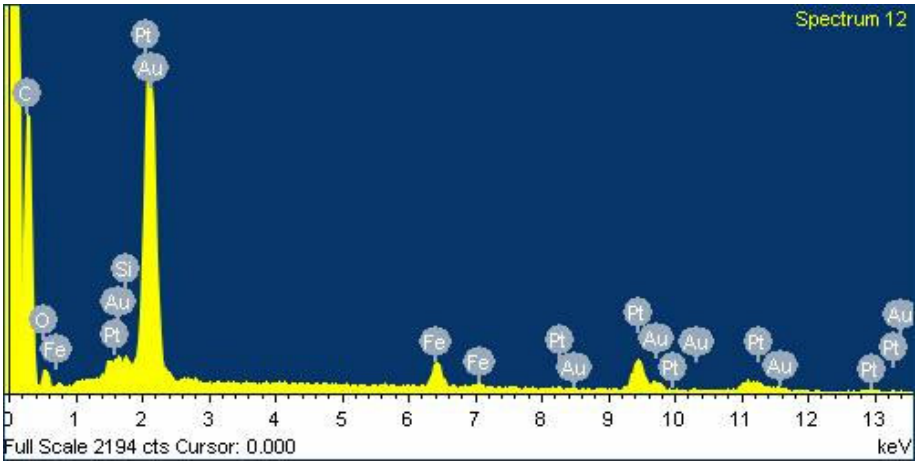

Figure 5.20. EDX pattern of Au/$FePt_3$ NPs. The atomic composition of the NPs is Au 28%, Fe 17%, and Pt 55%.

5.7.3.2 Electrochemical Characterization

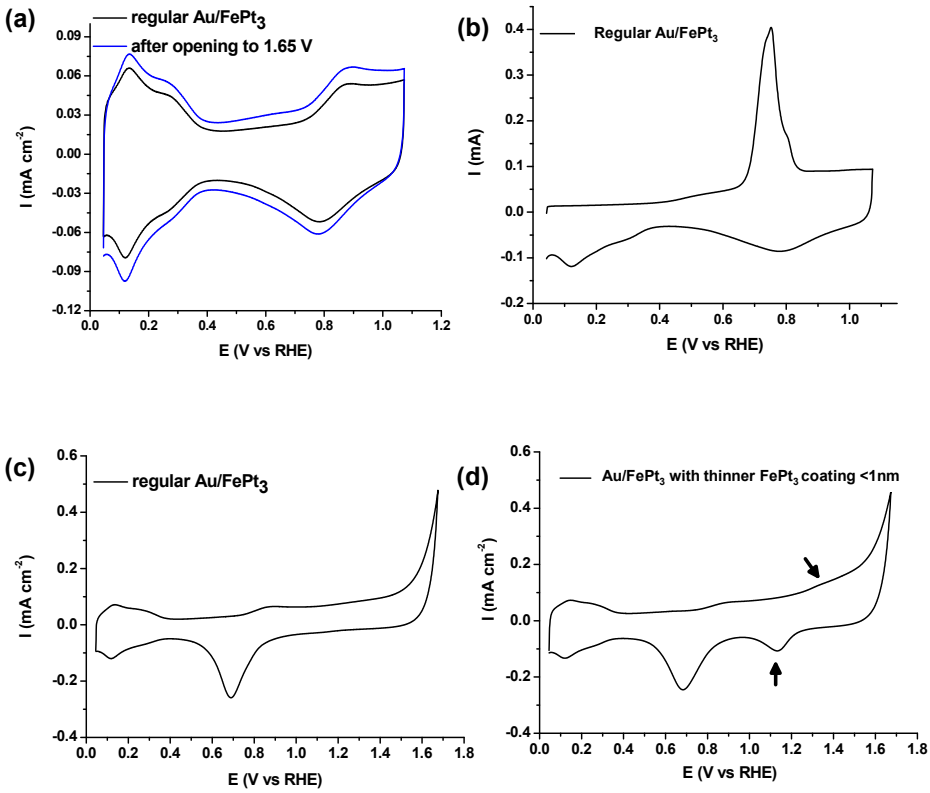

Figure 5.21. Electrochemical characterization of Au/FePt$_3$/C nanoparticle catalyst. (a) CVs before and after electrochemical characterizations (no surface atoms of Au after opening potential to 1.65 V); (b) CO stripping curve for regular 7/1.5 nm Au/FePt$_3$/C NPs; (c) and (d) CVs recorded for regular and Au/FePt$_3$/C with thinner FePt$_3$ coating catalysts respectively by opening the upper potential limit to 1.65 V.

The integrated H_{upd} charge obtained from regular particles was found be in perfect agreement with the charge calculated from CO stripping. In figure 5.21a, CVs before and after electrochemical characterizations for ORR at 20 and 60^{o}C, CO stripping and measurements in extended potential range up to 1.65 V, confirm that during the course of the measurements the H_{upd} area has not changed and the Pt-bimetallic coating remains stable without noticeable change in surface composition. However, the double layer region has increased (blue curve in insert **a**) after opening and cycling potential to 1.65 V. This is due to the oxidation and consecutive roughening of the carbon support at elevated potentials. A very

important finding is given in figure 5.21c, which depicts that no Au features are visible in the CV with upper potential opened to 1.65 V, confirming the formation of stable Pt surface free of any Au atoms.

We investigated another type of Au/$FePt_3$ NPs with bimetallic coating thickness less than 1.0 nm, which were obtained by controlled synthesis with reduced precursors (0.05 g $Pt(acac)_2$ and 0.015 ml $Fe(CO)_5$) and lower growth temperature (180^oC). The particles with thinner coating, however, show characteristic gold features in the CV when the upper potential limit is opened to 1.65 V (figure 5.21d), indicating that PtM-coating does not completely encapsulate Au core. This illustrates that, if present on the NP surface, Au atoms could be detected by cyclic voltammetry.

5.7.4 Part 4 Mechanism of Stability Enhancement

5.7.4.1 Nanoparticle Shape

Table 5.1. Theoretical calculation of average coordination number of surface atoms for different shape of nanoparticles of 10 nm in size.

Coordination number	Cubo-octahedron [44-46]	Icosahedron [47]
6	**24**	**12**
7	**396**	**0**
8	**726**	**570**
9	**3176**	**3420**
10	**0**	**0**
11	**0**	**0**
Total number of surface atoms	**4322**	**4002**
Average coordination number	**8.632**	**8.849**

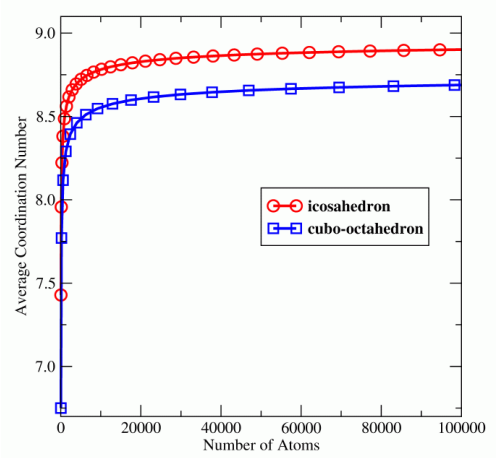

Figure 5.22. Average coordination number of the surface atoms varies as a fucntion of the total number of atoms in the particles with a cubo-octhedral, or icosahedral shape.

5.7.4.2 Stability enhancement through adsorbate induced segregation of Pt

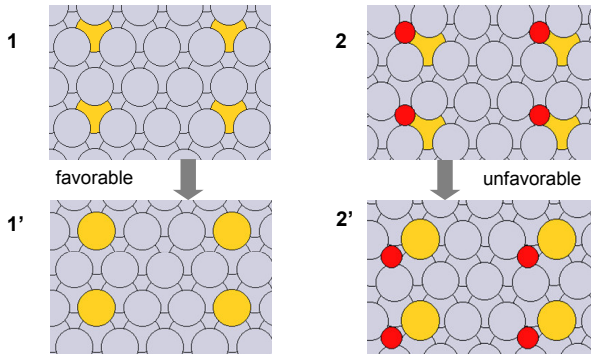

Figure 5.23. (*Top view*) Density Functional Theory calculations of subsurface and surface Au atoms on a Pt(111) surface: (1-1') A top view of Au segregation from the subsurface to the surface layer; the energy change for this process is ~ -0.4 eV in vacuum (thermodynamically favorable). (2-2') A top view of Au segregation from the subsurface to the surface layer in the presence of adjacent oxygen on the surface. The segregation energy in this case is ≥ 0.0 eV (thermodynamically unfavorable), and Au atoms movement to the surface is supressed. Higher coverages of oxygen (as would be observed at elevated electrode potentials) are expected to further inhibit the movement of Au to the surface. All calculations are done on a (3x2), 5-layer unit cell with the top three layers relaxed. The RPBE functional is used with a Monkhorst-Pack k-point grid of (3,4,1); ultrasoft pseudopotentials are employed, and a planewave cutoff of 340 eV (density cutoff of 500 eV) is also used.
Gray spheres denote Pt, yellow denotes Au and red denotes O.

Pt is much more oxophilic than Au, this means that Pt surface atoms oxidize at more negative potentials than Au surface atoms. The onset of oxide adsorption on Au is shifted positively with more than 600 mV (figure 5.1a).

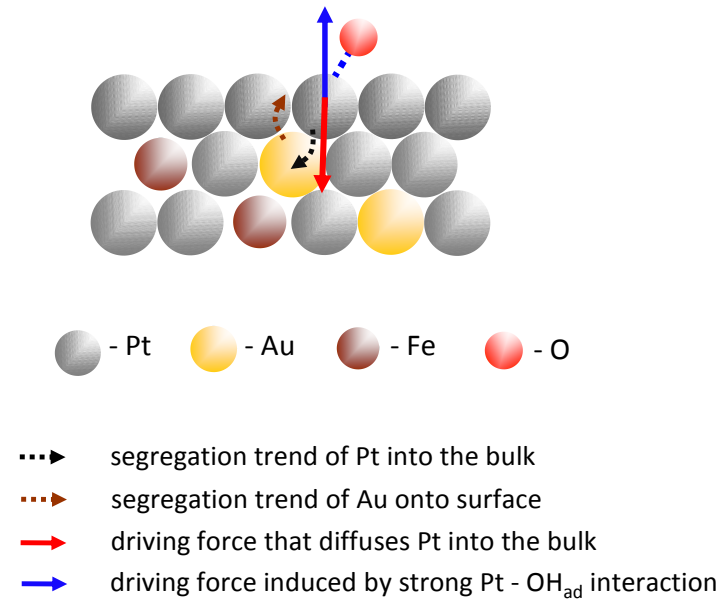

Figure 5.24. (*Side View*) Schematic illustration of the stability enhancement mechanism

Au atoms tend to segregate on the surface due to the lower surface energy of Au than Pt, but under the given electrochemical conditions (0.6 < E < 1.1 V), oxygenated species (*e.g.*, O, OH) are binding strongly to surface Pt, which provide the driving force for Pt atoms to stay on the surface in the highly oxophilic environment. Such a counterbalance between the two opposing forces (see figure 5.24); the rather strong interaction between Pt and surface oxides on one side, and the tendency of Au to segregate over Pt on the other side, stabilizes of the topmost Pt layer.

5.7.4.3 Stabilization of Pt surface atoms through the hindered place exchange mechanism

Gold cannot be oxidized in the given potential range that is relevant for the ORR (0.6 < E < 1.2 V), and therefore occurrence of Au in the subsurface layers would make the formation of subsurface oxides less energetically favorable and hence suppress the dissolution of Pt.

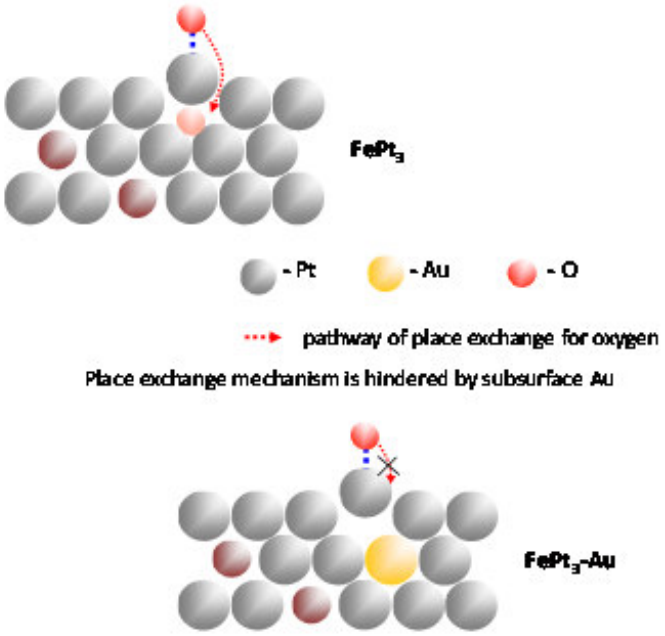

Figure 5.25. (*Side View*) Schematic illustrations of stability enhancement mechanism of Pt surface atoms in multimetallic NPs

5.7.4.4 DFT calculations of the subsurface atomic oxygen adsorption in $FePt_3$(111) alloys with subsurface Au

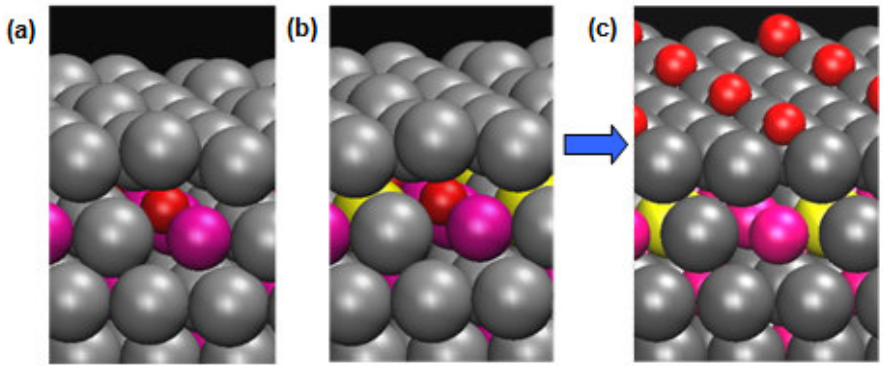

Figure 5.26. (Side View) Most favorable absorption of subsurface oxygen. (a) FePt3 alloy with 0.5 ML of Fe in the first subsurface layer. (b) Au/FePt3 alloys with 0.5 ML of Fe and 0.25 ML of Au in the first subsurface layer. (c), the overall thermodynamic driving force for subsurface oxygen formation. Gray spheres denote Pt, yellow denotes Au, red denotes O, and magenta denotes Fe.

Figure 5.26 (a) corresponds to a classic Pt skin-type structure. When a Au atom is substituted for Pt in the subsurface layer (b), the strength of subsurface oxygen adsorption decreases in magnitude by about 0.15 eV. Since the corresponding strength of surface Pt-oxygen binding is nearly the same in both cases, the overall thermodynamic driving force for subsurface oxygen formation (i.e., the subsurface minus the surface oxygen binding energies) also decreases in magnitude by a comparable amount due to the presence of subsurface Au. Oxygen place exchange thus becomes thermodynamically less favorable, thereby reducing Pt loss in the ternary system under this well-known Pt-dissolution mechanism.

References

[1] W. Vielstich, A. Lamm, and H. A. Gasteiger, Handbook of fuel cells : fundamentals, technology, and applications, Wiley, Chichester, England ; Hoboken, N.J., 2003.

[2] B. Richter, D. Goldston, G. Crabtree, L. Glicksman, D. Goldstein, D. Greene, D. Kammen, M. Levine, M. Lubell, M. Savitz, D. Sperling, F. Schlachter, J. Scofield, and J. Dawson, Reviews of Modern Physics. 80 (2008) S1.

[3] P. J. Ferreira, G. J. la O', Y. Shao-Horn, D. Morgan, R. Makharia, S. Kocha, and H. A. Gasteiger, Journal of the Electrochemical Society. 152 (2005) A2256.

[4] A. J. Appleby, Catal. Rev. 4 (1971) 221.

[5] T. Toda, H. Igarashi, H. Uchida, and M. Watanabe, Journal of the Electrochemical Society. 146 (1999) 3750.

[6] U. A. Paulus, A. Wokaun, G. G. Scherer, T. J. Schmidt, V. Stamenkovic, V. Radmilovic, N. M. Markovic, and P. N. Ross, Journal of Physical Chemistry B. 106 (2002) 4181.

[7] H. A. Gasteiger, S. S. Kocha, B. Sompalli, and F. T. Wagner, Applied Catalysis B-Environmental. 56 (2005) 9.

[8] S. Guerin, B. E. Hayden, C. E. Lee, C. Mormiche, and A. E. Russell, Journal of Physical Chemistry B. 110 (2006) 14355.

[9] H. T. Duong, M. A. Rigsby, W. P. Zhou, and A. Wieckowski, Journal of Physical Chemistry C. 111 (2007) 13460.

[10] S. Koh, J. Leisch, M. F. Toney, and P. Strasser, Journal of Physical Chemistry C. 111 (2007) 3744.

[11] A. U. Nilekar, Y. Xu, J. L. Zhang, M. B. Vukmirovic, K. Sasaki, R. R. Adzic, and M. Mavrikakis, Topics in Catalysis. 46 (2007) 276.

[12] V. R. Stamenkovic, B. Fowler, B. S. Mun, G. F. Wang, P. N. Ross, C. A. Lucas, and N. M. Markovic, Science. 315 (2007) 493.

[13] V. R. Stamenkovic, B. S. Mun, M. Arenz, K. J. J. Mayrhofer, C. A. Lucas, G. F. Wang, P. N. Ross, and N. M. Markovic, Nature Materials. 6 (2007) 241.

[14] J. Greeley and J. K. Norskov, Journal of Physical Chemistry C. 113 (2009) 4932.

[15] V. Stamenkovic, B. S. Mun, K. J. J. Mayrhofer, P. N. Ross, N. M. Markovic, J. Rossmeisl, J. Greeley, and J. K. Norskov, Angewandte Chemie-International Edition. 45 (2006) 2897.

[16] J. Zhang, K. Sasaki, E. Sutter, and R. R. Adzic, Science. 315 (2007) 220.

[17] Y. Shao-Horn, W. C. Sheng, S. Chen, P. J. Ferreira, E. F. Holby, and D. Morgan, Topics in Catalysis. 46 (2007) 285.
[18] V. Komanicky, K. C. Chang, A. Menzel, N. M. Markovic, H. You, X. Wang, and D. Myers, Journal of the Electrochemical Society. 153 (2006) B446.
[19] D. S. Strmcnik, D. V. Tripkovic, D. van der Vliet, K. C. Chang, V. Komanicky, H. You, G. Karapetrov, J. Greeley, V. R. Stamenkovic, and N. M. Markovic, Journal of the American Chemical Society. 130 (2008) 15332.
[20] J. Luo, L. Wang, D. Mott, P. N. Njoki, Y. Lin, T. He, Z. Xu, B. N. Wanjana, I. I. S. Lim, and C. J. Zhong, Advanced Materials (Weinheim, Germany). 20 (2008) 4342.
[21] T. Ghosh, M. B. Vukmirovic, F. J. DiSalvo, and R. R. Adzic, Journal of the American Chemical Society. 132 (2010) 906.
[22] S. Peng, Lee, Y., Wang, C., Yin, H., Dai, S., Sun, S., Nano Research. 1 (2008) 229.
[23] T. J. Schmidt, V. Stamenkovic, M. Arenz, N. M. Markovic, and P. N. Ross, Electrochimica Acta. 47 (2002) 3765.
[24] F. Tao, M. E. Grass, Y. W. Zhang, D. R. Butcher, J. R. Renzas, Z. Liu, J. Y. Chung, B. S. Mun, M. Salmeron, and G. A. Somorjai, Science. 322 (2008) 932.
[25] D. Ferrer, A. Torres-Castro, X. Gao, S. Sepulveda-Guzman, U. Ortiz-Mendez, and M. Jose-Yacaman, Nano Letters. 7 (2007) 1701.
[26] X. M. Lu, H. Y. Tuan, J. Y. Chen, Z. Y. Li, B. A. Korgel, and Y. N. Xia, Journal of the American Chemical Society. 129 (2007) 1733.
[27] Z. M. Peng, J. B. Wu, and H. Yang, Chemistry of Materials. 22 (2010) 1098.
[28] S. H. Sun, C. B. Murray, D. Weller, L. Folks, and A. Moser, Science. 287 (2000) 1989.
[29] K. Kinoshita, Journal of the Electrochemical Society. 137 (1990) 845.
[30] K. J. J. Mayrhofer, B. B. Blizanac, M. Arenz, V. R. Stamenkovic, P. N. Ross, and N. M. Markovic, Journal of Physical Chemistry B. 109 (2005) 14433.
[31] C. e. a. Wang, J. Phys. Chem. C. (2009).
[32] E. F. Holby, W. C. Sheng, Y. Shao-Horn, and D. Morgan, Energy & Environmental Science. 2 (2009) 865.
[33] Z. L. Wang, Journal of Physical Chemistry B. 104 (2000) 1153.
[34] B. Lim, J. G. Wang, P. H. C. Camargo, M. J. Jiang, M. J. Kim, and Y. N. Xia, Nano Letters. 8 (2008) 2535.
[35] S. E. Habas, H. Lee, V. Radmilovic, G. A. Somorjai, and P. Yang, Nature Materials. 6 (2007) 692.
[36] M. C. Daniel and D. Astruc, Chemical Reviews. 104 (2004) 293.
[37] N. Kimizuka, T. Abe, and K. Itaya, Denki Kagaku. 61 (1993) 796.
[38] A. V. Ruban, H. L. Skriver, and J. K. Norskov, Physical Review B. 59 (1999) 15990.
[39] H. You, D. J. Zurawski, Z. Nagy, and R. M. Yonco, Journal of Chemical Physics. 100 (1994) 4699.
[40] B. Hammer, L. B. Hansen, and J. K. Nørskov, Phys. Rev. B. 59 (1999) 7413.
[41] L. Bengtsson, Physical Review B. 59 (1999) 12301.
[42] D. Vanderbilt, Phys. Rev. B. 41 (1990) 7892.
[43] G. Kresse and J. Furthmuller, Comput. Mater. Sci. 6 (1996) 15.
[44] G. F. Wang, M. A. Van Hove, P. N. Ross, and M. I. Baskes, Journal of Chemical Physics. 121 (2004) 5410.
[45] G. F. Wang, M. A. Van Hove, P. N. Ross, and M. I. Baskes, Journal of Physical Chemistry B. 109 (2005) 11683.

[46] G. F. Wang, M. A. Van Hove, P. N. Ross, and M. I. Baskes, Journal of Chemical Physics. 122 (2005).
[47] C. L. Cleveland and U. Landman, Journal of Chemical Physics. 94 (1991) 7376.

Chapter 6

Platinum-alloy Nanostructured Thin Film Catalysts for the Oxygen Reduction Reaction

In an effort to increase fuel cell activity for the oxygen reduction reaction (ORR), a range of metallic alloy nanostructured thin film (NSTF) catalysts have been manufactured by 3M and measured both at room temperature and at 333K. Characterization of the particles was done ex-situ by microscopy and X-Ray diffraction and in situ by the rotating disk electrode (RDE). Optimal loadings for the ORR were established and activities superior to carbon supported nanoparticles (Pt/C) have been recorded. The most active catalyst was a 55 weight%$_{Pt}$ PtNi alloy, which is an order of magnitude more active than Pt/C in kinetic current, and an improvement factor of 2.5 in mass activity. Lowering the platinum content of this catalyst did not lead to increased mass activity values.

6.1 Introduction

The need for clean cars as well as a more efficient use of energy rather than burning fuel in internal combustion engines instigated many companies to make fuel cell operated devices and vehicles available to the general public [1]. A major challenge lies in optimizing the oxygen reduction reaction (ORR) in the fuel cell [2-5], especially to make fuel cells operable in large-scale automotive applications. This challenge sparked a concentrated effort to improve fuel cell catalysts [2, 3, 6-16] to meet the department of energy (DOE) targets [17].

One of the busiest fields currently is the development of high surface area catalysts. These catalysts are usually carbon-supported, which is accompanied by many problems, such as contact problems, particle dissolution [18-20] and agglomeration [19, 21] and carbon support corrosion [19, 22, 23]. It has been shown that the nanostructured thin film (NSTF) catalysts of 3M [21, 24, 25], which has no carbon support, are much more stable in a membrane electrode assembly (MEA) than any supported nanoparticulate catalyst [17].

For this reason the activity for the ORR of a range of PtNi and PtCo based multimetallic NSTF catalysts has been measured, both at room temperature and at 333K - a temperature close to the more ideal operating temperature (353K [5]) of a current polymer electrolyte fuel cell (PEFC). At temperatures higher than 333K, the water evaporation of the electrolyte would be too severe to measure the catalysts properly in the rotating disk electrode (RDE) setup. The proper loadings for the NSTF in RDE testing were established in detail, and activites are reported for the NSTFs measured with the appropriate loading.

The most active catalyst found in this work is the PtNi binary NSTF catalyst with mass activities exceeding those of carbon supported high surface area catalysts. The PtCo-based catalysts were significantly less active than their nickel-containing counterparts. A PtNiCo ternary catalyst was also tested, the activity of which resembles the other PtCo catalysts closely and does not approach the level of the PtNi and PtNiFe catalysts. Finally, the content of Pt in the alloy was reduced in an effort to lower total Pt loading of the catalyst. Unfortunately, this did not lead to increased kinetic activities, and hence also did not yield increased mass activities.

6.2 Experimental

The metallic NSTF catalyst was manufactured by 3M as reported previously [24, 25]. In brief, the desired metals were sputtered consecutively on a perylene red film. This creates the so-called nanostructured thin film (NSTF) catalyst. In order to facilitate measurements in RDE, the individual whiskers were brushed off the manufactured films and stored as a powder. The Pt/C catalyst used in this work is a state-of-the-art 5 nanometer sized Pt catalyst from Tanaka (TKK, Tokyo), supported on vulcan.

To prepare the suspension needed for electrode preparation for the thin film RDE method [26], a small glass bottle was cleaned in a beaker with acid and boiled repeatedly with Milli-Q H_2O (18.2 MΩ resistivity, less than 4 ppb toc). About 2 mg of NSTF catalyst powder was weighed into the bottle and 2 ml Milli-Q water added. Next, the suspension was sonicated for at least 30 minutes before use. A pre-polished Glassy Carbon (GC) disc of 6 mm in diameter was mounted in a KLF leak-free collet. The collet with GC disc inserted was cleaned in concentrated perchloric acid for 10 minutes, followed by extensive rinsing with Milli-Q water. Prior to the experiment the resistance of the disc in the collet was checked to assure the absence of electrical resistance. The GC disk in the collet is then polished with 0.05 μm aluminum oxide, followed by rinsing with Milli-Q H_2O and cleaning in acid. A measured volume of the sonicated catalyst suspension, was then pipetted onto the GC disc. The collet was put onto a hotplate at 40^{o}C in an Ar atmosphere and left to dry. After the electrode had dried, the surface was rinsed with Milli-Q water to wash off the loosely bonded particles and subsequently protect the surface from contamination and exposure to atmospheric gases. The electrolyte was in all cases 0.1M $HClO_4$, prepared by diluting concentrated 70% concentrated perchloric acid (Grade ACS, AMD Chemicals). The electrolyte was made in batches of 500 ml; stored in a teflon flask which was cleaned beforehand in a mixture of concentrated nitric and sulfuric acid, and rinsed extensively with Milli-Q water.

A standard in-house 3-electrode cell was used in all measurements. An Ag / AgCl electrode in equilibrium with the electrolyte separated from the cell by a salt bridge was used as the reference electrode. The Luggin-Haber capillary was positioned as close to the cell as possible without disturbing the flow by rotation of the electrode, generally at about 10 mm distance from the surface of the disk. Any residual Ohmic losses were compensated for by positive feedback in the potentiostat. The reference electrode was calibrated daily with a reversible hydrogen electrode (RHE) in the

electrolyte used that day. All potentials reported here are reported with respect to the RHE. The counter electrode was a Pt mesh. The potentiostat used was an Autolab PGSTAT 30 with ECD, scan-gen and FI-20 modules, in combination with the Autolab GPES software.
The glass electrochemical cell was of in-house design, with a heating jacket built into the cell for measurements at elevated temperatures.

6.3 Results and Discussion

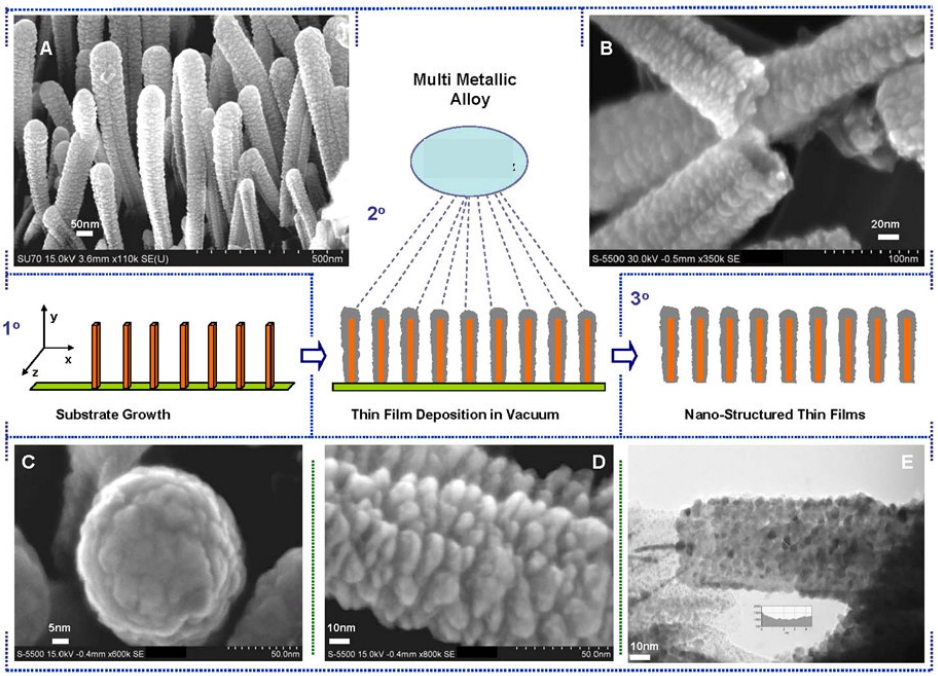

Figure 6.1, TEM (E) and SEM images (A-D) of 3M NSTF catalysts with schematic representation of deposition in the middle.

6.3.1 Microscopy

TEM and SEM images of the catalysts as received from 3M Company are shown in figure 6.1. The figure shows clearly the unique structure of the catalyst which resembles long rods, studded with rough atomic stumps. Images of this catalyst have been published before in [21, 27]. The middle part of figure 6.1 shows a

graphic representation of the deposition process. Consecutive layers of platinum and the respective metal in the alloy were sputtered on a crystallized organic pigment (*N*,*N*-di(3,5-xylyl)perylene-3,4:9,10bis(dicarboximide), in short: perylene red) in Ultra High Vacuum (UHV) [24, 25]. The sputtering covered each of the perylene reds whiskers with a thin metallic film. Platinum and nickel were sputtered in sequence on the substrate, resulting in a metal-covered, whiskered polymer, shown in the electron microscope images in figure 6.1. For our experiments we deposited this catalyst on the GC disk in the RDE setup by first brushing the individual whiskers off the supporting polymer and then suspending them in a small bottle with milli-Q water. The resulting suspension was pipetted on the disk and left to dry in argon, with the amount of suspension pipetted determining the loading of Pt on the disk.

6.3.2 Determination of proper platinum loading

Before activity measurements could be commenced, the proper loading of particles on the glassy carbon needed to be determined. Mayrhofer et al [28] determined this to be 42 μg_{pt} cm^{-2}_{disk}, while 3M company uses a loading of 0.1 mg_{Pt} cm^{-2} on their fuel cell cathode [21]. Our determination of the optimal loading is shown in figure 6.2. Part A of the figure shows the full oxygen reduction reaction (ORR) curves in 0.1 M perchloric acid with a rotation of 1600 rpm. The curves compare well to those reported before [27, 28]. The influence of the loading is illustrated in this graph:

First, the potential at half the diffusion limiting current, the so-called half-wave potential ($E_{1/2}$) increases linearly with loading from 42 to 130 cm^{-2}_{disk}, shown in detail in figure 6.2B. The increasing value for $E_{1/2}$ with increasing loading makes the traditional measure of activity (overpotential at half-wave) difficult to apply for this catalyst, unless the loading is kept constant. Also, high loading decreases the potential window of the kinetic region (at currents lower than half the diffusion limiting current) and can introduce larger errors from reading the current at the steep part of the slope [26].

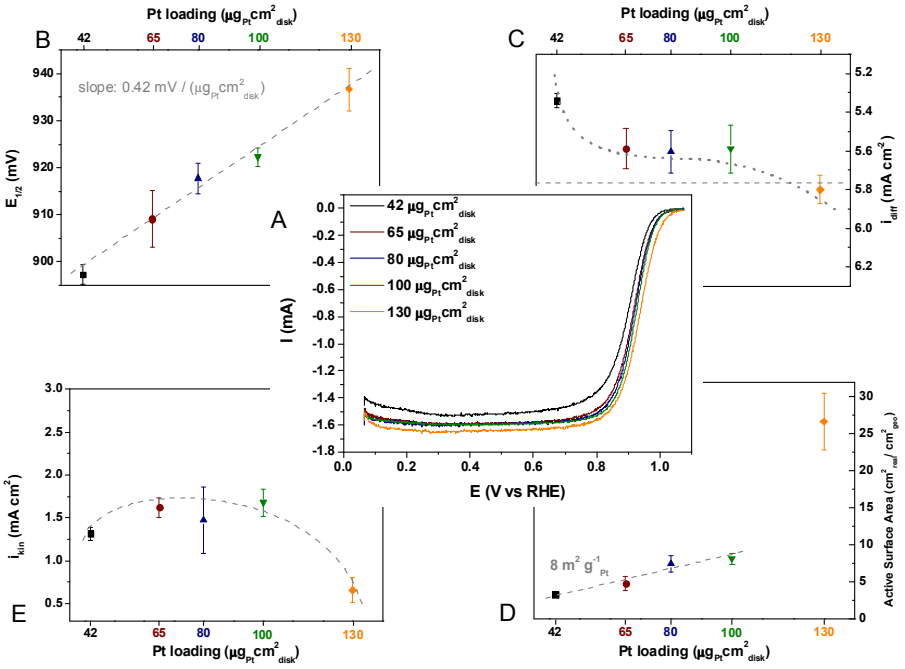

Figure 6.2, effect of loading of the NSTF catalyst on glassy carbon. A shows the full ORR curves, measured at 293K with a rotation of 1600 rpm and a scan rate of 20 mV s^{-1} in 0.1 M $HClO_4$. Shown in the surrounding graphs is the effect of the loading on half-wave potential (B), diffusion limiting current for the ORR (C), active surface area as measured from H_{upd} (D) and kinetic current density for the ORR at 0.9V vs RHE (E). Standard deviations of a minimum of 3 measurements are given in error bars.

Secondly, the diffusion limiting current (I_{diff}) increases with increasing loading, with a stable region from 60 to 100 μg_{Pt} cm^{-2}_{disk}, as shown in figure 6.2C. This is in agreement with experiments of Mayrhofer *et al.*, who claim measurements with lower diffusion limiting currents still exhibit the same kinetic current densities when properly corrected for the diffusion contribution [28], but a proper diffusion limiting current is recommended. The diffusion limiting current observed in the experiment is also a measure of distribution. Even at higher loadings I_{diff} will occasionally be lower than theoretically expected. This is indicative of a poor catalyst distribution on the GC disk, with part of the glassy carbon area uncovered by the NSTF and thus exposed, and other spots on the disk too thickly coated. When the loading is increased above 100 cm^{-2}_{disk}, I_{diff} increases again, this is because the catalyst layer becomes thicker than the diffusion layer and the accepted mass-transport characteristics for the RDE are not satisfied anymore [29, 30].

Furthermore, the active surface area (SA) increases (of course) with increasing loading. As can be seen in figure 6.2D, this is a linear trend until about 100 μg_{Pt} cm^{-2}_{disk}, with a surface area of about 8 m^2 per gram of Pt. This is 20% lower than the value of 10 m^2 g^{-1} reported before [21] in an actual MEA. The effect of the support (GC) cannot be ruled out in this respect, and the shielding of part of the surface of the NSTF by the glassy carbon can result in a lower active surface area per gram of Pt. Interestingly, at higher loadings the SA increases more than linearly. This coincides with the appearance of the higher diffusion limiting current as mentioned before, and is indicative of a multi-layer of catalyst particles on the disk. The surface area at high loading is puzzling as it exceeds the value reported for the MEA, we found the approximate surface area per mass for high loadings to be around 20 m^2 g_{Pt}^{-1}, double the value reported for the same catalyst in a MEA [21]. This effect has to our knowledge not been observed before and further investigation would be required to find the origin.

Finally what this means for the activity, *i.e.* the kinetic current at 0.9V versus RHE, is shown in figure 6.2E. Clearly, lower and higher loadings have a reduced activity for the ORR. At low loadings, the SA is harder to determine, which causes the lower apparent activity. In other measurements on the alloys (not shown in figure 6.2), lower loadings actually gave increased activity values due to the under-estimation of the active surface area by H_{upd} charge. It is best to avoid these troubles and remain slightly higher in loading, though not as high as 130 μg_{Pt} cm^{-2}_{disk}, where the more than linearly increased surface area suppressed the kinetic current.

After taking these observations into consideration we determined the ideal loading in these experiments to be 65 μg_{Pt} cm^{-2}_{disk}; low enough to avoid problems due to the increased activity and to not waste Pt (and thus to keep mass activities relatively high), yet high enough to avoid problems with distribution and surface area determination. All further figures and data reported here are measured with 65 μg_{Pt} cm^{-2}_{disk}.

6.3.3 Blank Cyclic Voltammetry

Different alloy and monometallic Pt catalysts were considered in this research. Three bimetallic catalysts: Pt_3Co, Pt_3Ni and $PtNi_2$ and four trimetallic catalysts; a $Pt_{0.32}Ni_{0.61}Fe_{0.07}$ alloy, a $Pt_{0.67}Co_{0.30}Mn_{0.03}$ alloy, a $Pt_{0.4}Co_{0.5}Zr_{0.1}$ alloy, and a Pt_3CoNi alloy.

For the ease of comparison of the cyclic voltammograms (CVs) the catalysts will be divided into two categories; one group containing platinum nickel alloys (PtNi of

various compositions and PtNiFe ternary alloy) and the other group containing Pt cobalt alloys (PtCo, PtCoMn and PtCoZr). There was also a PtCoNi ternary alloy, which falls into both categories, and of course there is monometallic Pt NSTF.

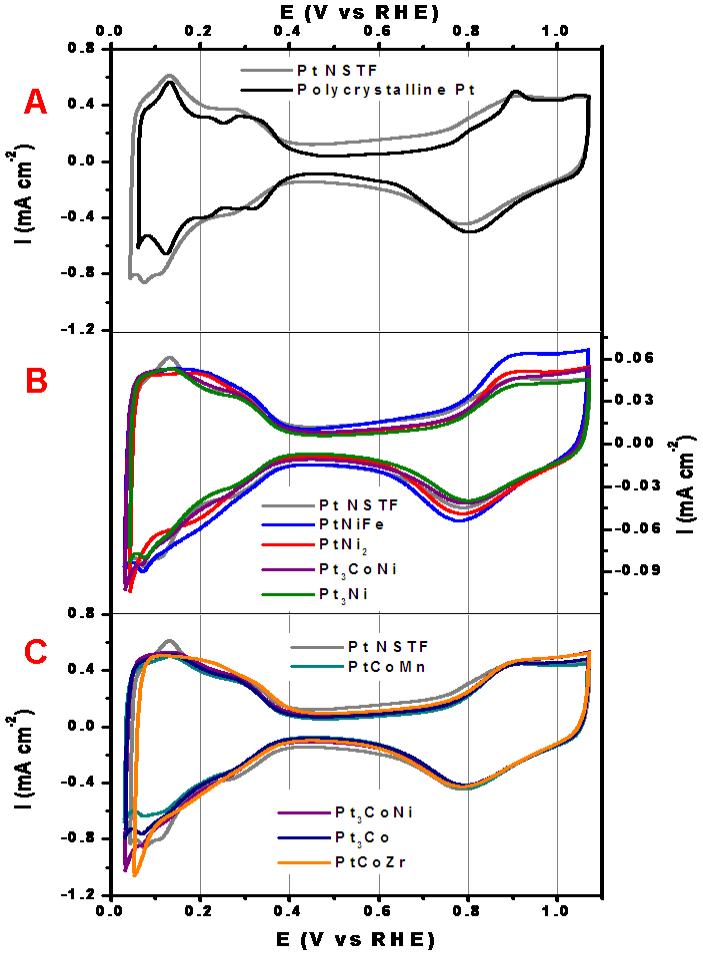

Figure 6.3. Blank cyclic voltammetry for the various NSTF catalysts. All were measured at 293K in 0.1M $HClO_4$ with 50 mV s^{-1}. Part A shows the comparison between monometallic Pt NSTF and polycrystalline bulk platinum. The various Nickel and Cobalt-based catalysts are shown in B and C respectively. The loading of the NSTF catalyst was 65 μg_{Pt} cm^{-2}_{disk}.

Blank CVs are shown in figure 6.3, with the Ni samples in part B and the Co samples in part C. To make a good comparison between nanostructured catalysts and extended surfaces, a comparison with bulk polycrystalline Pt is in order (figure 6.3A). The underpotentially deposited hydrogen (H_{upd}) region at potentials lower

than 0.4V exhibits much broader features for the NSTF catalyst. This is a first indication that on the thin film catalyst a plethora of lower coordinated Pt atoms are on the surface and the crystalline islands are smaller than on poly Pt. This is confirmed by the higher affinity for surface oxide, with the oxide reduction peak shifted about 25 mV lower for the NSTF catalyst. The magnitude of adsorption of oxides (as determined from the charge of oxide formation in figure 6.3A) on Pt NSTF is higher immediately positive of the onset of surface oxide formation at 0.75V, see figure 6.4A. This charge offers a convenient way to compare adsorption on the catalysts without the influence of the double layer charging, which is much higher for the NSTF catalyst due to the glassy carbon support.

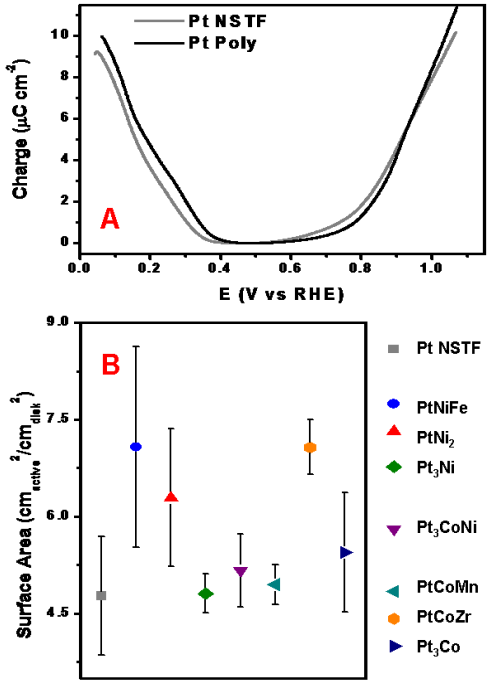

Figure 6.4. Part A shows the comparison in adsorption isotherm between monometallic Pt NSTF and polycrystalline bulk platinum; this is the charge under the blank CV after double-layer correction. The surface areas of the various Nickel and Cobalt-based catalysts are shown in part B, compared to the Pt NSTF as well. The loading of the NSTF catalyst was 65 μg_{Pt} cm^{-2}_{disk}.

It is clear that the differences in cyclic voltammetry between the alloy catalysts are subtle. PtNiFe and $PtNi_2$ show a different H_{upd} region. The maximum in that region is reached at a higher potential than in case of the monometallic NSTF. Pt_3Ni and PtCoNi exhibit similar CVs, both closely resembling the blank CV of Pt NSTF. The

double layer of the alloy electrodes is very dependent on the polishing of the GC substrate and can differ from experiment to experiment as the disk is rougher. Also, the capacity of the double layer is independent of the active surface area of the catalyst and as the figure is normalized for this active surface area, the double layer capacity seems largest on the catalysts with lower active SA. There is even less difference between the various cobalt containing catalysts, where only PtCoZr exhibits the broader H_{upd} region seen with PtNiFe and $PtNi_2$ as well. From figure 6.4B it is concluded that these three catalysts have the largest surface area of the catalyst per gram Pt at a loading of 65 μg_{Pt} cm^{-2}_{disk}. The alloys are expected to have a higher specific surface area, as the non-noble elements from the alloy dissolve upon contact with the electrolyte [31], thereby roughening the surface. Moreover, becausese the surface of monometallic Pt NSTF is already rough (see the electron microscope images in figure 6.1), the increase would be expected to be minimal. As is evident from figure 6.4, this expectation holds true for most catalysts, but PtNiFe, $PtNi_2$ and PtCoZr catalysts have an increased surface area compared to the other catalysts due to their reduced Pt content in the compositions relative to the other alloys, with 32, 33 and 40 atomic-% respectively. This increased surface area also explains the broader H_{upd} features mentioned before, as there is less crystallinity and a larger amount of low-coordinated Pt surface atoms.

6.3.4 Oxygen Reduction Reaction

The results for the oxygen reduction reaction (ORR) are shown in figure 6.5. The loading of the NSTF catalysts was 65 μg_{Pt} cm^{-2}_{disk}. Tafel plots are shown in part A-C to graphically compare the activity for the NSTF catalysts over a range of 0.85 to 0.95V. It can be seen that there is not a definite linear relation between log of the current versus the potential (Tafel slope). It is clear that the monometallic Pt NSTF catalyst offers a large improvement versus carbon supported Pt catalyst, see figure 6.5A. The Pt/C used in our work has a loading of 17 μg_{Pt} cm^{-2}_{disk}; a higher loading will lead to diffusion layer problems. This catalyst is itself three times more active than the commercial Pt/C catalysts [32]. Therefore, the Pt NSTF catalyst has an improvement of close to an order of magnitude versus the reported Pt/C, as claimed before [28]. Obvious from figure 6.5B is the high activity for the ORR for the low-Pt content PtNi-catalysts, PtNiFe and $PtNi_{2.5}$, an order of magnitude versus the 5 nm TKK catalyst, and 3 times more active than the monometallic Pt NSTF. The other nickel-containing and the cobalt-based catalysts are very similar in activity, as can be seen in figure 6.5C. The catalytic specific activity is better illustrated in

figure 6.6, in which the half-wave potential (A) and kinetic current at 900 mV versus RHE (B) are compared. Again, the obvious conclusion from this graph is that the two catalysts with high nickel content; *i.e.* PtNiFe and $PtNi_2$ are superior in activity to the other NSTFs and completely overshadow the Pt/C catalyst.

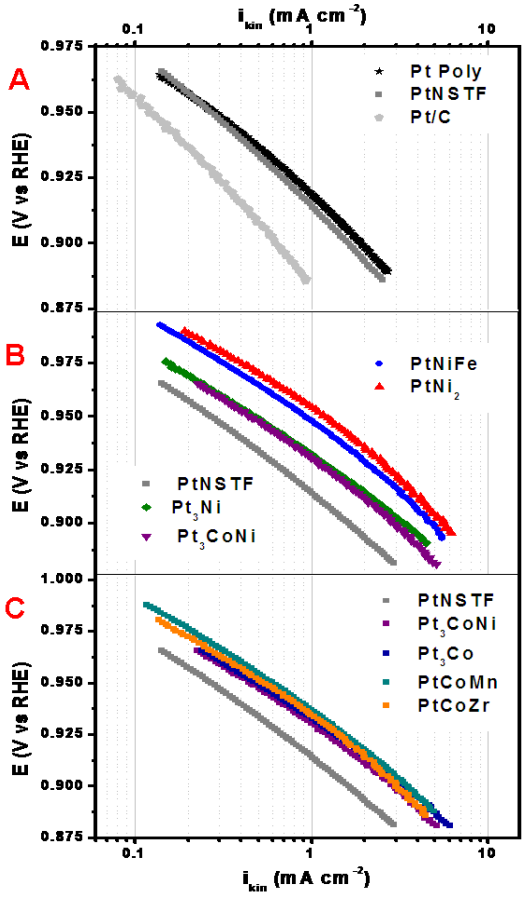

Figure 6.5. ORR on NSTF catalysts, compared to polycrystalline Pt. Tafel plots are shown in A for the monometallic Pt sample, compared to Pt poly and state of the art Pt/C catalyst, and B and C show the Ni and Co based alloys respectively.

This is true even when we consider the mass activities at 900 mV versus RHE, shown in figure 6.6C. Carbon supported nanoparticles usually have high mass activities, because one of the main advantages of these nanoparticles is the high surface area to mass ratio. This high ratio means that there is a lot of active surface area per gram of platinum, for example about 50 m^2 platinum surface area per gram

of Pt for a carbon-supported 5 nm sized catalyst, as determined from our reference experiments. This is a factor of 5 higher than the typical value for the NSTF catalysts. However, from our experiments we can conclude that the PtNi alloy NSTF catalysts actually have a higher mass activity than the carbon supported Pt nanoparticles in addition to higher kinetic activities.

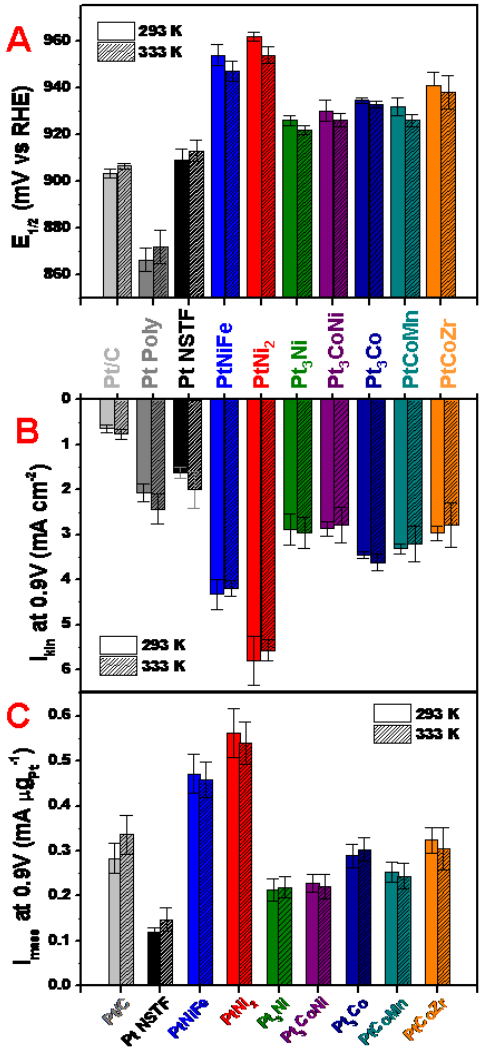

Figure 6.6. Bar graphs of the ORR on NSTF catalysts, compared to polycrystalline Pt. Part A shows the half-wave potential ($E_{1/2}$) for loadings of 65 μg_{Pt} cm$^{-2}_{disk}$ for the NSTF catalysts and 18 μg_{Pt} cm$^{-2}_{disk}$ for the Pt/C and the kinetic and mass current densities at 0.9V are shown in part B and C, respectively. The single-color bars represent the value at 293 K, and the accented bars represent 333 K.

Finally, the Pt content in the PtNi alloy was lowered in an effort to increase mass activity even further. Figure 6.7 shows the results for the ORR activity at 0.9 V vs RHE, both in kinetic and in mass activity. The blank cyclic voltammetries of these catalysts (not shown) are essentially identical. It is clear that the kinetic currents decrease when the platinum content is lowered, but the expected increase in mass activity due to increased Pt surface area being available, is not observed. Based on the catalysts measured, the PtNi alloy with about 55 wt-% platinum is the best catalyst.

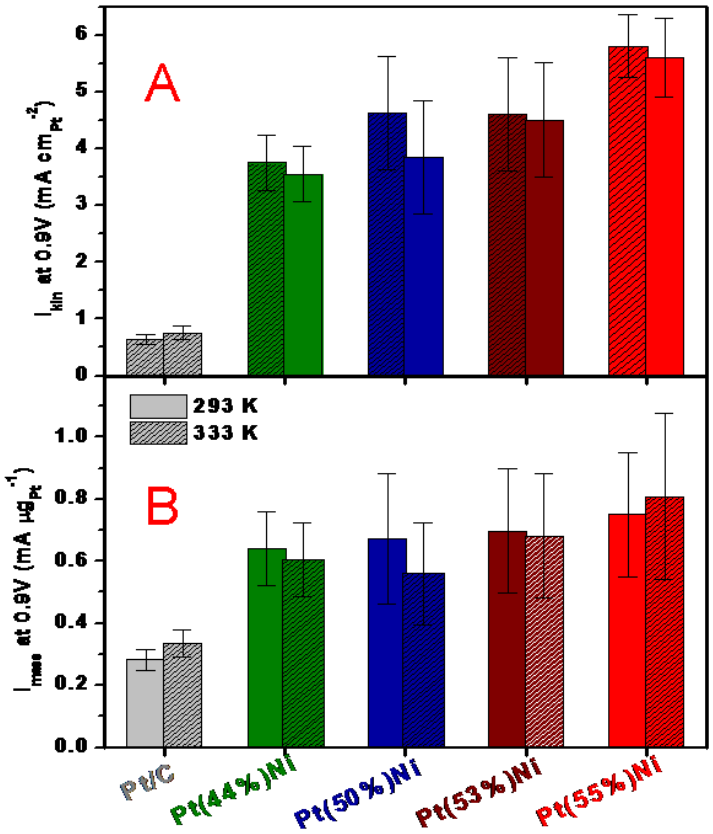

Figure 6.7. Bar graphs of the ORR on PtNi catalysts with different Pt content. Light grey bars show the Pt/C catalyst as a reference. The kinetic and mass current densities at 0.9V are shown in part A and B, respectively. Loadings of 65 μg_{Pt} cm^{-2}_{disk} for the NSTF catalysts and 18 μg_{Pt} cm^{-2}_{disk} for the Pt/C were used. The single-color bars represent the value at 293 K, and the accented bars represent 333 K.

6.4 Conclusion

A range of multimetallic platinum-based nanostructured thin film catalysts, manufactured by 3M, have been measured in the rotating disk electrode setup. These nanoparticles are not dispersed on vulcan, but directly deposited on glassy carbon; in the actual membrane electrode assembly, they are non-carbon supported. The surface of these particles is shown to be very rough, full of low-coordinated platinum.

The optimal loading for RDE measurements in our setup was determined to be 65 $\mu g_{Pt}\ cm^{-2}_{disk}$; a higher loading will give rise to problems with the diffusion layer, and anomalous behavior of the surface area per gram of particles, while a lower loading will leave parts of the glassy carbon disk uncovered, and cause the diffusion limiting current to be lower than the expected value for a 6 mm disk electrode.

Of all catalysts measured, the PtNi alloys show more promising activities for the ORR than the PtCo based alloys. Especially the PtNi, and PtNiFe alloys are very active. Furthermore, these alloys have a higher active surface area per gram of platinum, which means that their mass activities are superior to any of the other catalysts measured. The mass activities of PtNi and PtNiFe even exceed those of 5 nm platinum nanoparticles on vulcan.

Finally, the Pt content in the PtNi alloy was lowered in an effort to increase mass activity even further, but it was found that when the Pt content is lowered below 55 mass%, this does not lead to an increased mass activity.

So far, the most active catalyst measured, both in kinetic current and in mass activity, is the PtNi alloy with 55 mass% platinum. Further experiments will be necessary to optimize the platinum content in the alloy. Furthermore, the layer thickness of the sputtered layer on the perylene red may be reduced, which will increase the Pt utilization and give increased mass activity values. It is clear from our experiments, that the NSTF catalyst is a very promising ORR catalyst, with increased activities compared to any other nanoparticulate catalyst currently available.

References

[1] B. Johnston, M. C. Mayo, and A. Khare, Technovation. 25 (2005) 569.
[2] H. A. Gasteiger, S. S. Kocha, B. Sompalli, and F. T. Wagner, Applied Catalysis B-Environmental. 56 (2005) 9.

[3] H. A. Gasteiger, J. E. Panels, and S. G. Yan, Journal of Power Sources. 127 (2004) 162.
[4] M. C. Tucker, Journal of Power Sources. 195 (2010) 4570–4582.
[5] H. A. Gasteiger and M. F. Mathias, in: M. Murthy, T. F. Fuller, J. W. Van Zee, and S. Gottesfeld, (Eds), Proton conducting membrane fuel cells III: proceedings of The Electrochemical Society, Vol. 2002-31, The Electrochemical Society, Inc., Pennington, New Jersey, 2005, p. 1.
[6] K. J. J. Mayrhofer, B. B. Blizanac, M. Arenz, V. R. Stamenkovic, P. N. Ross, and N. M. Markovic, Journal of Physical Chemistry B. 109 (2005) 14433.
[7] J. X. Wang, N. M. Markovic, and R. R. Adzic, Journal of Physical Chemistry B. 108 (2004) 4127.
[8] L. Xiao, L. Zhuang, Y. Liu, J. T. Lu, and H. D. Abruna, Journal of the American Chemical Society. 131 (2009) 602.
[9] J. Hernandez, J. Solla-Gullon, E. Herrero, A. Aldaz, and J. M. Feliu, Journal of Physical Chemistry C. 111 (2007) 14078.
[10] L. G. R. A. Santos, K. S. Freitas, and E. A. Ticianelli, Electrochimica Acta. 54 (2009) 5246.
[11] A. S. Arico, P. Bruce, B. Scrosati, J. M. Tarascon, and W. Van Schalkwijk, Nature Materials. 4 (2005) 366.
[12] A. Atkinson, S. Barnett, R. J. Gorte, J. T. S. Irvine, A. J. Mcevoy, M. Mogensen, S. C. Singhal, and J. Vohs, Nature Materials. 3 (2004) 17.
[13] P. Strasser, S. Koh, T. Anniyev, J. Greeley, K. More, C. Yu, Z. Liu, S. Kaya, D. Nordlund, H. Ogasawar, M. F. Toney, and A. Nilsson, Nature Chemistry. Published online: 25 April 2010 | doi:10.1038/nchem.623 (2010).
[14] K. J. J. Mayrhofer and M. Arenz, Nature Chemistry. 1 (2009) 518.
[15] J. Greeley, I. E. L. Stephens, A. S. Bondarenko, T. P. Johansson, H. A. Hansen, T. F. Jaramillo, J. Rossmeisl, I. Chorkendorff, and J. K. Norskov, Nature Chemistry. 1 (2009) 552.
[16] D. Strmcnik, K. Kodama, D. van der Vliet, J. Greeley, V. R. Stamenkovic, and N. M. Markovic, Nature Chemistry. 1 (2009) 466.
[17] K. E. Martin, J. P. Kopasz, and M. K.W., Fuel Cell Chemistry and Operation, Chapter 1, 2010, p. 1.
[18] K. Kinoshita, J. Lundquist, and P. Stonehart, Journal of Electroanalytical Chemistry. 48 (1973) 157.
[19] S. S. Zhang, X. Z. Yuan, J. N. C. Hin, H. J. Wang, K. A. Friedrich, and M. Schulze, Journal of Power Sources. 194 (2009) 588.
[20] K. J. J. Mayrhofer, S. J. Ashton, J. C. Meier, G. K. H. Wiberg, M. Hanzlik, and M. Arenz, Journal of Power Sources. 185 (2008) 734.
[21] M. K. Debe, A. K. Schmoeckel, G. D. Vernstrorn, and R. Atanasoski, Journal of Power Sources. 161 (2006) 1002.
[22] V. Komanicky, K. C. Chang, A. Menzel, N. M. Markovic, H. You, X. Wang, and D. Myers, Journal of the Electrochemical Society. 153 (2006) B446.
[23] Y. Y. Shao, J. Wang, R. Kou, M. Engelhard, J. Liu, Y. Wang, and Y. H. Lin, Electrochimica Acta. 54 (2009) 3109.
[24] M. K. Debe and A. R. Drube, Journal of Vacuum Science & Technology B. 13 (1995) 1236.
[25] M. K. Debe and R. J. Poirier, Journal of Vacuum Science & Technology a-Vacuum Surfaces and Films. 12 (1994) 2017.

[26] T. J. Schmidt, H. A. Gasteiger, G. D. Stab, P. M. Urban, D. M. Kolb, and R. J. Behm, Journal of the Electrochemical Society. 145 (1998) 2354.
[27] A. Bonakdarpour, K. Stevens, G. D. Vernstrom, R. Atanasoski, A. K. Schmoeckel, M. K. Debe, and J. R. Dahn, Electrochimica Acta. 53 (2007) 688.
[28] K. J. J. Mayrhofer, D. Strmcnik, B. B. Blizanac, V. Stamenkovic, M. Arenz, and N. M. Markovic, Electrochimica Acta. 53 (2008) 3181.
[29] F. Gloaguen, P. Convert, S. Gamburzev, O. A. Velev, and S. Srinivasan, Electrochimica Acta. 43 (1998) 3767.
[30] J. Perez, E. R. Gonzalez, and E. A. Ticianelli, Electrochimica Acta. 44 (1998) 1329.
[31] V. R. Stamenkovic, B. S. Mun, K. J. J. Mayrhofer, P. N. Ross, and N. M. Markovic, Journal of the American Chemical Society. 128 (2006) 8813.
[32] P. J. Ferreira, G. J. la O', Y. Shao-Horn, D. Morgan, R. Makharia, S. Kocha, and H. A. Gasteiger, Journal of the Electrochemical Society. 152 (2005) A2256.

Chapter 7

Multimetallic Nanotubes as Catalysts for the Oxygen Reduction Reaction

The most challenging problems in fuel cell technology are the insufficient activity of the catalyst for the cathodic oxygen reduction reaction (ORR), catalyst degradation, and carbon support corrosion. To improve the former, and avoid the latter, carbon-free multimetallic nanotube catalysts that can attain superior rates of activity for the ORR have been synthesized. The composition and surface morphology of the multimetallic nanotubes have been tuned to improve their affinity for the ORR. The level of activity for the fuel cell cathodic reaction established on the multimetallic nanotube catalyst exceeds the highest value reported for bulk polycrystalline Pt bimetallic alloys, and it is 60-fold more active than the current state-of-the-art Pt/C nanoscale catalyst.

7.1 Introduction

Hydrogen fuel cell research is a major effort over the last few decades with many companies working to make fuel cell operated devices and vehicles available to the general public. A major challenge lies in optimizing the cathode side of the fuel cell. Whereas the hydrogen oxidation reaction (HOR) on the anode side is easily catalyzed and well understood, the oxygen reduction (ORR) on the cathode side is trickier. The reversible potential for the ORR at 1.23 V vs RHE is not reached in real fuel cells due to the inactivity of current catalysts, leading to losses of potential of more than 400 mV. Due to this lower operating potential, the thermal efficiency drops well below the theoretical value of 83% at the reversible potential. It is therefore of importance to increase the activity of ORR catalyst to reduce this overpotential and increase fuel cell efficiency. [1-13].

Most of the research centers around platinum, as it is the best monometallic ORR catalyst. There is, however, the scarceness and cost of Pt to consider as well. As the implementation of fuel cells worldwide would require a significant amount of catalyst, this would put an enormous strain on the Pt stock, as well as raise the price of a fuel cell significantly. With the current state-of-the-art catalyst, an approximate five fold reduction in Pt content is necessary to meet requirements in cost for large scale automotive applications [1]. This has fueled the interest to search for relatively cheaper non-precious metals as catalysts [14-19] Moreover, multi-metallic alloys have made significant impact in fuel cell catalyst design by decreasing the amount of platinum while improving activity and durability [20], and are thus the focus of much research, both on bulk electrodes [20-32], and in nanoscale catalysts. [33-37] Rather than a trial and error approach in synthesizing these alloys, we have relied in previous work on well-defined, extended surfaces. [20-22] Pt_3Ni and Pt_3Co alloy catalysts are the most active catalysts for the ORR to date [21], with Pt_3Ni (111) skin electrodes being the most active of all [20]. Therefore nanoscale systems based on these metals were synthesized by 3M. Rather than using PtNi nanoparticles on Carbon [31, 38, 39], a Pt-alloy nanostructured thin film (NSTF) catalyst, which required no high-surface-area carbon support, was prepared by 3M, therby eliminating carbon support corrosion. This NSTF catalyst is prepared by sputtering metal layers on a polymer substrate and is shown to have increased activity and stability compared to traditional carbon-supported nanoparticles. [40, 45-47]

7.2 Experimental

Consecutive layers of platinum and nickel were sputtered on a crystallized organic pigment (*N*,*N*-di(3,5-xylyl)perylene-3,4:9,10bis(dicarboximide), in short: perylene red) in Ultra High Vacuum (UHV). [45, 46] The sputtering covered each of the perylene red whiskers with a thin metallic film. The platinum and nickel were sputtered on the substrate one after the other; the deposition resulting in a metal-covered, whiskered polymer, see figure 7.1. Both the monometallic Pt and the PtNi alloy catalyst were created by this method.

The whiskers thus created were gently brushed off the perylene red and collected, creating in essence a catalyst powder. The inside of the whiskers still contained residue of the polymer and in some places several whiskers were clumped together. However, the resulting powder of these whiskers allowed suspending them in water. The mass of the catalyst is determined by weighing on a microbalance before transferring to a clean container and the desired amount of pure water is added. This allows for a relatively accurate determination of the amount of catalyst per unit volume in the suspension. The suspension is then sonicated for at least 45 minutes before depositing a known amount on a polished glassy carbon disk, so that the disk will contain the desired loading of Pt. The pipetted drop is then let to dry in a light argon stream at about 50^{o}C. When the drop has dried, the catalyst is firmly attached to the GC disk, without the need for nafion. Before immersion in the cell at potential control, the surface of the disk was gently washed with a small flow of ultrapure water to dislodge any loosely bound particles, and to assure that the layer was stable.

The nanotubes were generated by thermally annealing the brushed-off whiskers in a tube furnace in a hydrogen atmosphere, as depicted in schematic form in figure 7.2. About 1.5 mg catalyst was deposited on a small tray in the middle of a quartz glass tube in a furnace (Carbolite MTF 10/15/160) at room temperature. For 15 minutes research grade argon gas was blown through the tube to purge all oxygen out, followed by flowing research grade hydrogen to create a pure hydrogen atmosphere. After the pure hydrogen atmosphere is achieved, the furnace is set to 100 ^{o}C. The furnace is kept at 100 ^{o}C for 30 minutes to make sure all possible water evaporates from the sample. Consequently the temperature is increased in 100 ^{o}C increments every 15 minutes until the temperature of 400^{o}C is reached. The furnace is then kept at 400 ^{o}C for 4 hours, after which heating is shut off and the catalyst slowly cooled to < 90^{o}C at which temperature the flow of gas in the cell is switched

to a mixture of 5% hydrogen in Argon. The catalyst is then let to cool overnight in this gas flow. When preparing the nanotube electrode, the catalyst powder from the furnace was treated identical to the whiskers described above.
An Autolab PGSTAT 30 with FI20, ECD, ADC and SCAN GEN modules was used for the electrochemical measurements. Perchloric acid of 0.1M, created by diluting concentrated $HClO_4$ (70%, JT Baker ULTREX II Ultrapure Reagent) with MilliQ water, was in all cases the electrolyte. All gases were research grade (5N5+). A silver-silver chloride reference electrode was used. However, all potentials referred to in this paper are converted to the pH independent RHE scale. All experiments were repeated a substantial amount of times (at least 4 times each) to confirm reproducibility, and to improve accuracy in the determination of kinetic activities.
A measured ORR curve consist of a kinetic contribution and a diffusion contribution according to the relation $I_{ORR}^{-1} = I_{kinetic}^{-1} + I_{diffusion}^{-1}$. The kinetic current densities ($i_{kinetic} = I_{kinetic}$ / Active Surface Area) were deduced from the measured ORR curve by using this relation. The active surface area of the nanocatalysts was determined by integrating the H_{upd} part of the CV and correcting for the double layer charge as described in [37].

7.3 Results

7.3.1 Catalyst preparation and characterization

The schematic in the middle of figure 7.1 shows the step by step deposition of the catalyst onto the polymer film, and the SEM images (figure 7.1 A-D) show the morphology of the nanostructured thin film (NSTF). Figure 7.1A shows the extended surface morphology of the particles in the NSTF. The ordering of these particles on this support is very random and disoriented. Figure 7.1B shows a close up of a broken particle from which is clear that if the support is removed, hollow particles will emerge. The whiskers have a very rough outer surface with smaller individual whiskers on top of the large ones. Images D and E indicate that the outside of the particles is very rough and full of low-coordinated Pt atoms. However, Gancs *et al.* [40] recently reported that these small side whiskers have mainly (111) facets with a small amount of (100) facets. Figure 7.1E shows a TEM image which clearly shows a relatively thin particle with surface stumps. To analyze this catalyst in a controlled way and compare it to state of the art Pt/C

catalyst we opted to use the Rotating Disk Electrode (RDE) method. (see [41] and Methods section) The increased specific activity for monometallic Pt NSTF catalysts versus Pt/C has been reported before. [40]

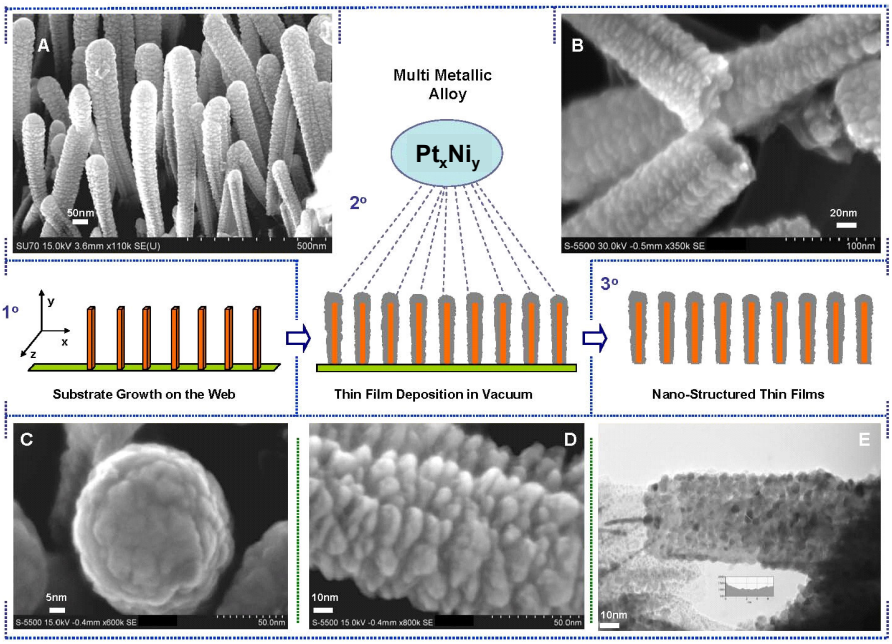

Figure 7.1, SEM images of the NSTF catalyst. Part A shows the macroscopic structure of the separate particles on the support. B shows a broken particle. C and D are close ups, with E a TEM image of this catalyst. Inset in the middle shows the production process.

However, a second approach to prepare the particles for RDE measurements was also performed. In an effort to clean the metallic particles from its supporting polymer, the catalyst was annealed prior to deposition on the glassy carbon (GC) disk; TEM images A through C show that in time the polymer substrate is disappearing and the particles become hollow. More information on the annealing preocedure can be found in the section 7.2. The time it takes to remove most of the perylene red is estimated to be about an hour from observations during the experiment with variable annealing times; details can be found in section 7.5. Figure 7.2A' through C' show that in time the surface structure changes as well with annealing; the low coordinated surface Pt disappear and a more smooth hollow nanotube emerges. The optimal time of annealing at 400 ^{o}C in a pure H_2 flow was deduced to be four hours. (see section 7.5)

The smoothening of the particles into nanotubes is expected to lower the surface area, which it does, but not by a large margin. The decrease in total electrochemical

surface area per μg_{Pt} after annealing is 10%, from an average 9.8 m^2 g_{Pt}^{-1} for the PtNi NSTF to an average 8.7 m^2 g_{Pt}^{-1} for the nanotubes. The active surface area was deduced from the charge of adsorbed hydrogen, as explained in [37]. The reason for this relatively small decrease is that a large portion of the surface on the inside was blocked by the polymer in the NSTF, and has been opened up after annealing the polymer, counterbalancing the loss in surface area through smoothening of the particles. As we will show below, the decrease in surface area is compensated by the increase in specific activity, so that even the mass activity has improved significantly.

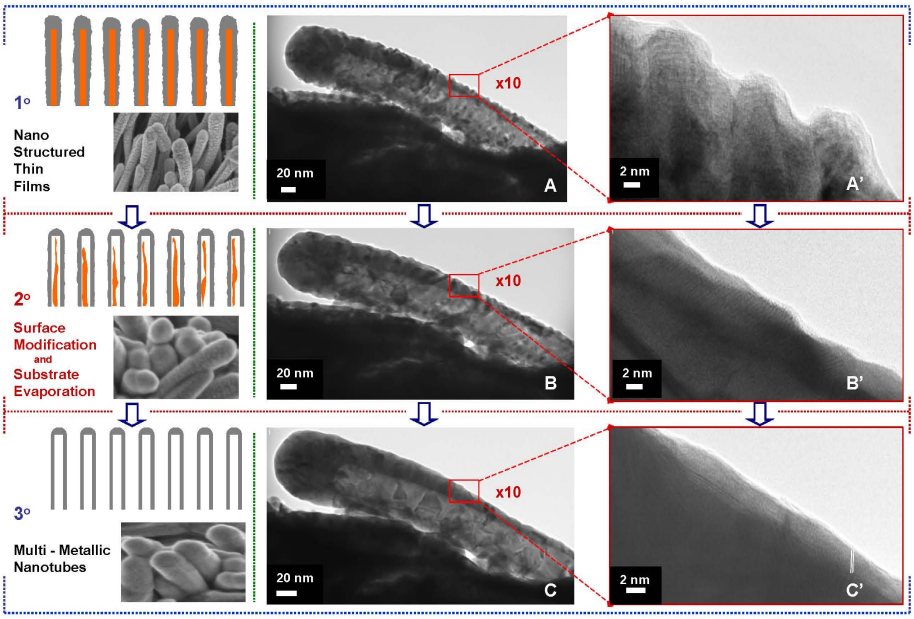

Figure 7.2. Schematic of the process of annealing the NSTF. TEM images A-C show the progressive substrate evaporation, while images A'-C' show the surface modification.

The XRD experiments shown in figure 7.3, show that during annealing there is a small angle shift, due to the lowered lattice constant, which points to further alloying of the catalyst with Pt atoms being replaced by Ni in the crystal lattice. Furthermore, the grain size of the (111) facets increase as is evident from the increased sharpness of the (111) peak in the XRD pattern. Finally the ratio between the (111) and (200) orientations has increased from 1 to 1.2, reinforcing the conclusion that with annealing the (111) facets on the nanotubes are improved and extended.

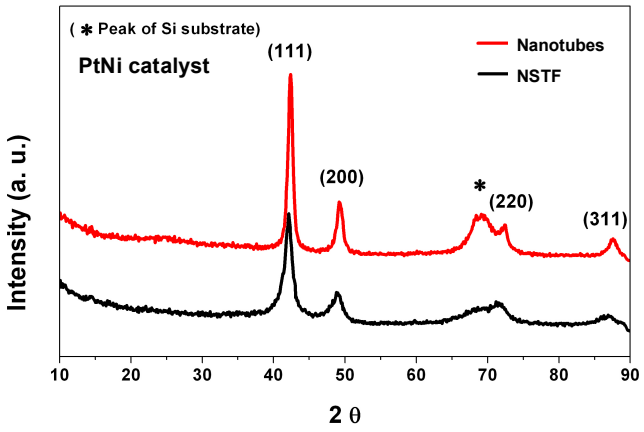

Figure 7.3. XRD analysis of PtNi nanotubes compared to its NSTF precursor. A small angle shift is visible after creating the rods, as well as grain size increase and ratio change between (111) and (200).

7.3.2 Electrochemical characterization

The PtNi NSTF catalyst exhibits very similar behavior to its monometallic counterpart in cyclic voltammetry, as shown in figure 7.4A. The region at low potentials, where hydrogen adsorb (< 0.4V in for the PtNi NSTF catalyst), is called the H_{upd} region. Small, features are visible in the H_{upd} region for PtNi NSTF (green curve) at about 0.1V,presumably due to (110)-sites [48, 49], similar to Pt NSTF (black curve). Oxide formation (at potentials > 0.7V; the surface oxide region) has a 50 mV higher onset on PtNi, compared to monometallic Pt, which is a first indication of the higher activity for the ORR, as surface oxides are the blocking species for the ORR on the catalyst surface [21]. However, the amount of surface oxides seems to be significantly larger than on Pt, as can be deduced from the charge under the CV in the surface oxide region. A possible explanation is that nickel readily oxidizes, but adsorbs no hydrogen in the H_{upd} region of a CV, leading to the observed discrepancy between the oxide region of monometallic Pt and the PtNi alloy.

The PtNi nanotubes behave very similar to the PtNi NSTF in this oxide region, the only difference being a slight delay in OH adsorption on the nanotubes compared to the NSTF. The H_{upd} part of the curve, however, is quite different. The Pt (111) CV is shown in the graph to point out the similarities between the single crystal and the PtNi nanotubes in the H_{upd} region. The flat feature for PtNi nanotubes may indicate that the surface of the particles has a large contribution of (111) facets compared to

(110) and (100). In the oxide region, however, the nanotubes' onset for the adsorption of oxide containing species is delayed with about 160 mV compared to Pt (111).

7.3.3 ORR

The ORR polarization curves are shown in figure 7.4B. All catalysts reach the expected theoretical diffusion limiting current on a 6 mm disk with a rotation of 1600 rpm. Kinetic current densities for the ORR are shown in figure 7.4C as Tafel plots. (For the determination of the kinetic current densities from the ORR curves, see section 7.2) In this figure, the order of kinetic currents becomes apparent, with Pt/C being the least active surface per unit of surface area, followed by Pt NSTF. A significant increase in activity is observed for the nanotubes as compared to the PtNi NSTF, and will be discussed below. The Tafel slopes can be deduced from this graph and follow an interesting trend: the higher the activity for oxygen reduction, the lower the Tafel slope. This means that the steepness of the curve, which is the increase in reaction velocity, is increased more than the onset of the ORR. Values for the Tafel slope range from 60 mV per decade and 70 mV dec^{-1} for Pt NSTF and polycrystalline Pt respectively, to 41 mV dec^{-1} for PtNi NSTF and nanotubes. Tafel slopes are often used to deduce information on reaction pathways, and values of 40 and 60 mV dec^{-1} point to different rate determining steps. The value of 60 mV dec^{-1} is typical for an electrochemical equilibrium, followed by a rate determining chemical step, whereas 40 mV dec^{-1} points to an electrochemical equilibrium, followed by an electrochemical rate determining step [42]. If in this case the Tafel slope holds the same information is debatable, as in our experiments on different NSTF catalysts a whole range of slopes from 40 to 60 mV dec^{-1} were found, and the mechanism of oxygen reduction is not expected to differ. These values are significantly lower from those obtained in the literature before (*e.g.* [21, 43]), which can be explained by the fact that those particular measurements did not correct for solution resistance. The importance of correcting for solution resistance is illustrated in Chapter 2 of this thesis.

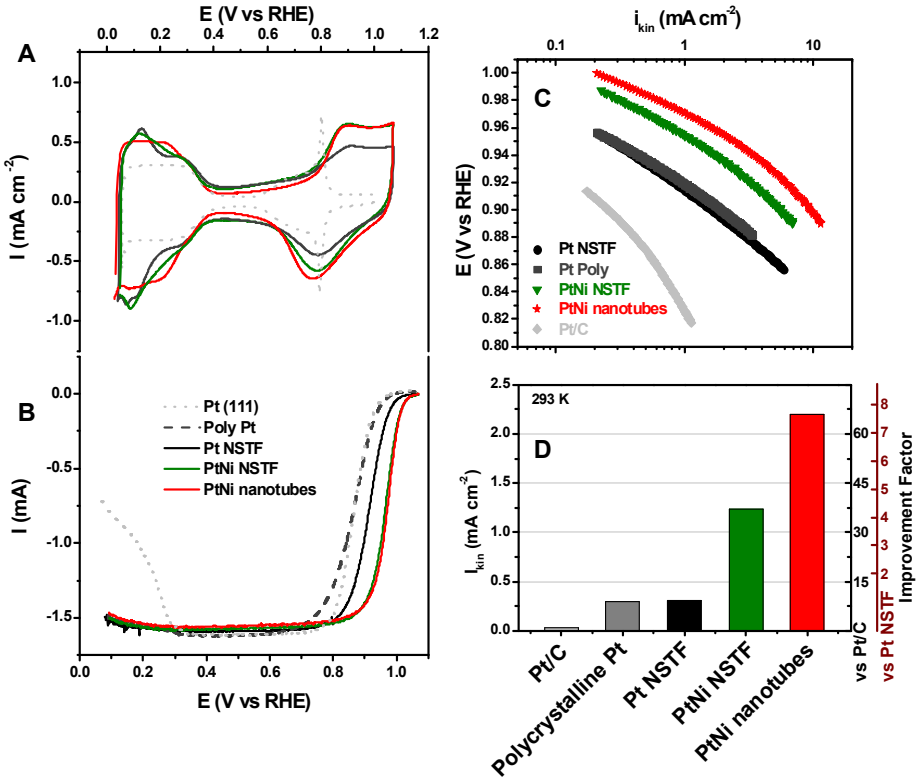

Figure 7.4. Cyclic voltammetry and Oxygen Reduction reaction on the NSTF catalysts. CVs are shown in A, measured with 50 mV $^{s-}$1 in 0.1M HClO4. The full ORR curves shown in B, measured in 0.1M $HClO_4$ with 20 mV $s^{-1.}$ The tafel slopes for the curves in B are shown in C. The bar graphs in D show the kinetic current and the improvement factor versus Pt (both carbon supported and NSTF). Values for Pt_3Ni skeleton and skin structures obtained from [19].

Concerning the activity for the ORR, there is a significant effect of both alloying and annealing. Similar as reported in [21], the bimetallic PtNi catalyst has a higher kinetic activity than platinum. In this case the PtNi whiskers are most properly compared to their own monometallic counterpart (Pt NSTF). The comparison is made by measuring the kinetic current density at 0.95V vs RHE for the catalysts. A lower potential of 0.9V or even 0.85V as has been used in the past [1, 20, 27, 43] is less accurate as the ORR on the alloy catalyst particles is so active at these potentials, that the current is strongly controlled by diffusion, see figure 7.4B. At 0.95V vs. RHE the kinetic current measured for the PtNi NSTF catalyst is 4.1 times higher than that for the monometallic Pt. The activity for the PtNi NSTF is even higher than the bulk Pt_3Ni alloy. When we subsequently anneal the PtNi catalyst

and create the nanorods, the activity increases to an improvement factor of 7.3 over Pt NSTF. This trend is similar to observed before [27], where annealed Pt_3Ni formed the "skin" Pt_3Ni structure, which was found to be more active for the ORR than the non-annealed "skeleton" structure. The NSTF and the nanotubes are about twice as active as these bulk Pt_3Ni alloys. When we compare the activity of the PtNi nanotubes to the value reported for the industry standard high-surface area catalyst [1], there is an improvement factor of over 60 versus Pt/C. The PtNi nanotube activity also surpasses bulk polycrystalline Pt, which is 10 times more active than Pt/C.

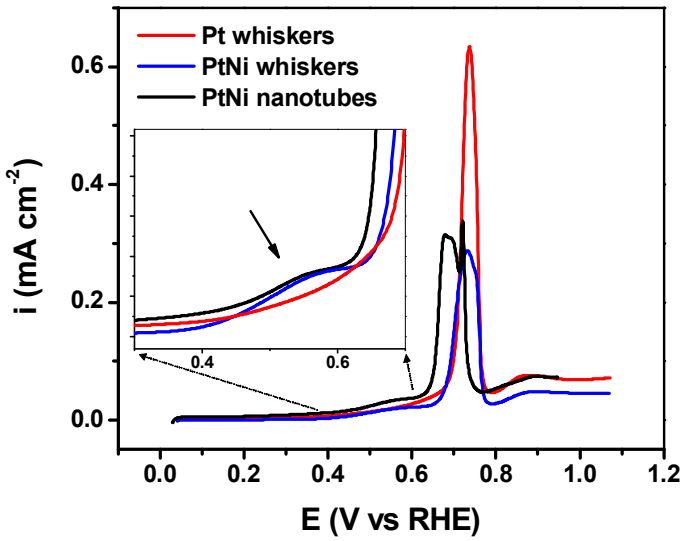

Figure 7.5. CO stripping on PtNi NSTF and nanotubes. Scan rate 50 mV s^{-1}. Inset shows an enlarged portion of the curve with an emphasis on a pre-oxidation peak.

At elevated temperatures of 60°C the improvement factors show similar trends, though the magnitudes differ. Monometallic Pt becomes more active at this temperature, whereas the PtNi catalyst does not. The improvement factor of the PtNi whiskers versus Pt at 60°C is 2.8. Nanotubes are about 1.3 times more active than PtNi whiskers at 60°C, and an improvement factor of 4.3 versus monometallic Pt NSTF is obtained. The improvement factor versus polycrystalline-Pt is still more than 3, which indicates that at 60 °C, the catalyst is still more active than bulk polycrystalline Pt-skin and skeleton type alloys. [27] One possible reason for the absence of activation of the PtNi catalyst at higher temperatures is the higher contamination level in a heated electrochemical cell. The more active catalyst sites

on this particular catalyst compared to monometallic Pt will be more sensitive to the same levels of small organic contaminations present in the cell.

To confirm that oxide containing species indeed adsorb at lower potentials on the PtNi nanotubes and to measure the true double layer charge for the electrochemical surface area determination as explained in [37], CO stripping experiments were performed. These are shown in figure 7.5 and give a CO coverage of 0.88 on the PtNi whiskers by comparing the charge of CO stripping with the charge of H_{upd}. This coverage is comparable to experiments performed on the monometallic Pt whiskers, where coverage was found to be 0.85. The result of CO stripping on the PtNi nanotubes is identical to the whiskers, with a coverage of 0.88, indicating that the surface composition of both catalysts must be similar. Furthermore, the CO stripping curves corroborate our conclusion that the nanotubes have a lower affinity for adsorption of oxide species, and that there are fewer low-coordinated Pt atoms on the surface. It has been shown before that low coordinated "defect" sites on well defined surfaces are the most active sites for CO oxidation [44]. In figure 7.5, a pre-peak can be seen for the NSTF catalysts, indicative of ample low-coordinated Pt sites on the surface, but no such peak is observed for the nanotubes. Furthermore, CO stripping from the surface proper starts at higher potentials for tubes, compared to the whiskers, while at monometallic Pt CO oxidation starts at an even lower potential. The combination of the higher onset potential for CO oxidation, together with the absence of a pre-peak is further evidence for the smoother defect-poor surface of the nanotubes.

A defect-poor surface does have the added disadvantage of a lower active surface area per unit of weight of Pt. As mentioned earlier, the PtNi nanotubes have a significant 10% decrease in surface area compared to the NSTF alloy. This means that the ratio between mass activities of the nanotubes versus the NSTF catalyst will diminishe slightly compared to ratio of the kinetic current densities. However, as is shown in figure 7.6, the nanotubes are still more active than the NSTF. And more importantly: both catalysts are more active than the carbon supported catalyst by a factor of 4 (whiskers) and 7 (nanotubes), despite the 25 times higher surface area per g_{Pt} for this highly dispersed catalyst [1].

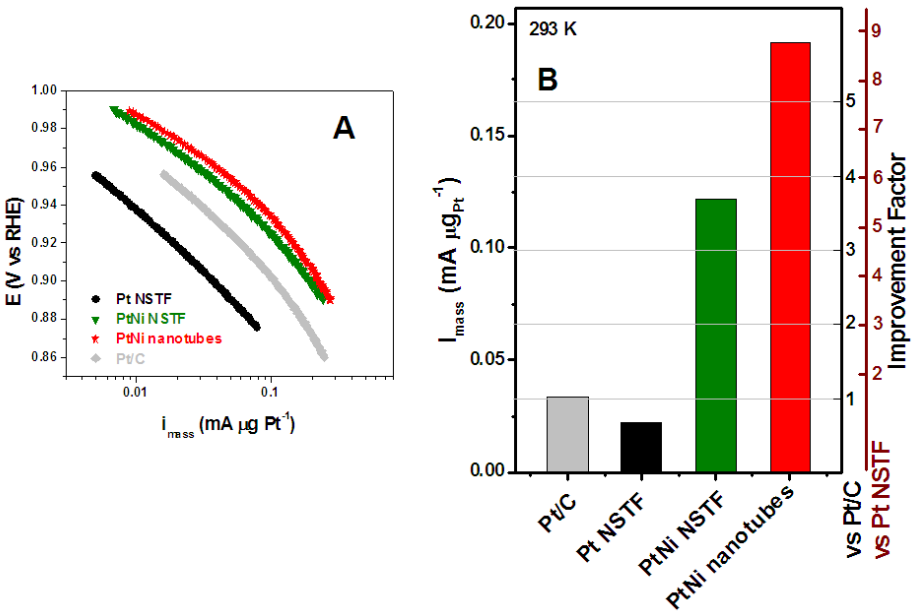

Figure 7.6. ORR mass activities of the nanocatalysts.

7.4 Conclusion

In summary, a novel method of nanocatalyst preparation has been reported. PtNi nanorods were created specifically tailored to inhibit surface oxidation, thereby activating the oxygen reduction reaction. CO stripping curves and X-ray diffraction patterns confirm the formation of a smoother, less defected surface after annealing of the PtNi NSTF catalyst to create PtNi nanotubes.

The highest kinetic activities ever measured for the ORR for nanocatalysts have been reported in this paper. Improvement factors of 7.5 versus polycrystalline Pt, 7.3 over monometallic Pt NSTF and more than 60 versus Pt/C were measured at room temperature. Even at 60°C the activities for PtNi nanorods exceed those of very active Pt-skin type polycrystalline alloys, with an increase in activity of 40 versus Pt/C and 4.5 versus polycrystalline Pt. More important is perhaps the significant increase in mass activity versus highly dispersed Pt nanoparticles on carbon. The 5.8 fold increase in activity versus Pt/C mass activity values at 20°C and 3.4 fold at 60°C underscore the great promise. Stability at higher operating

temperatures must be improved, but even at its current state the PtNi nanorods are a eminent improvement over carbon supported Pt nanoparticles.

7.5 Appendix

The optimal annealing temperature, environment and time were found by systematically changing these parameters. The experiments concerning optimization of the annealing procedure were performed on a prior version to the catalyst described in the paper. This particular catalyst was a ternary PtNiFe catalyst, with the iron present from contamination in the sputtering targets. The morphology and surface area were identical to the PtNi catalyst describes in the paper. The activity for the oxygen reduction reaction (ORR) was about 25% lower for the PtNiFe catalyst as compared to the PtNi.

7.5.1 General observations during the annealing

When the temperature is ramped up, a red deposition is visible on the quartz tube when the temperature is increased above 300^{o}C in H_2. This is residue of the perylene red, Inductively Coupled Photon Mass Spectroscopy (ICPMS) confirmed that no Pt, Ni or Fe was present in this residue. This confirms the removal of the red polymer substrate, without modifying the metal composition of the catalyst.

7.5.2 Effect of annealing temperature

The effect of annealing temperature and atmosphere can be seen in figure 7.7. Part A shows the cyclic voltammetry (CV) of those catalysts, and the main difference can be spotted in the H_{upd} region of the graph. Where the NSTF and the catalyst, annealed at 300^{o}C in Argon show a peak at 0.1V vs RHE, the hydrogen annealed curves do not. Those hydrogen annealed catalysts have a broader H_{upd} region with a slight feature visible at about 0.2V. The OH_{ads} region is not obviously shifted more positive for the hydrogen annealed catalysts. The effect on the oxygen reduction reaction (ORR) activity is clear, however. Part B shows an optimum reached for annealing above 350^{o}C. When the catalyst was annealed at even higher temperatures, the particles start agglomerating, and a successful transfer to the glassy carbon (GC) substrate was no longer able to be achieved.

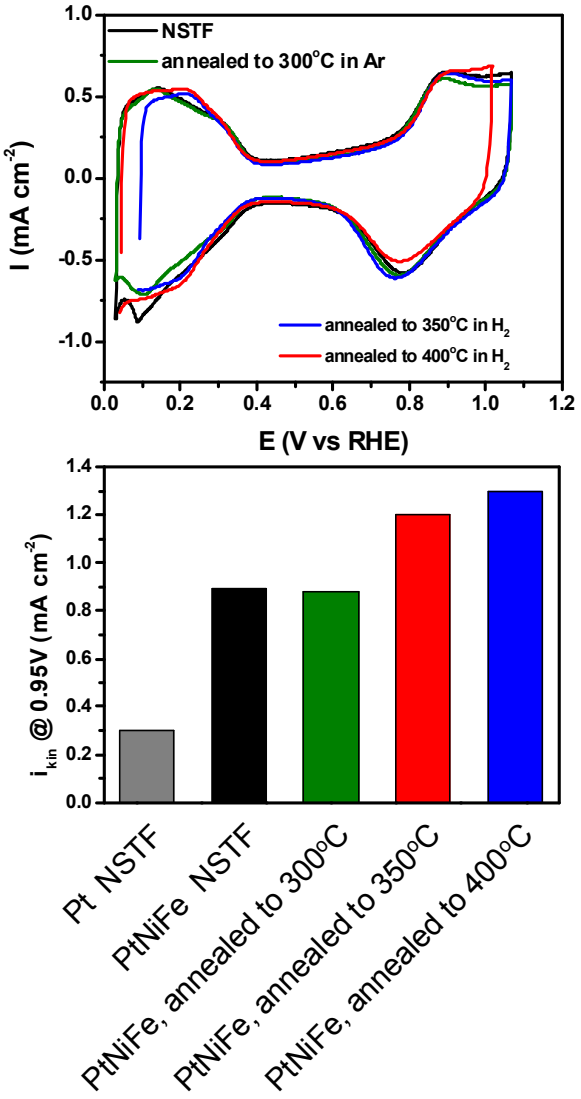

Figure 7.7. Effect of annealing temperature and atmosphere on blank cyclic voltammetry and oxygen reduction reaction. Black line in part A represents the PtNiFe NSTF catalyst, green, blue and red represent annealing at 300°C in Ar, 350°C in H_2 and 400°C in H_2, respectively. Scans were measured in 0.1 M $HClO_4$ at 50 mV s^{-1}.
Part B represents kinetic current density values, measured at 0.95 V vs RHE in the ORR curve in 0.1 M $HClO_4$ with 1600 rpm rotation and a scan rate of 20 mV s^{-1}. The grey bar represents monometallic Pt NSTF, the other colors represent the same catalysts as those in part A.

7.5.3 Different annealing environments

Figure 7.8 shows blank CVs obtained after annealing the particles in an alternate way. The red curve in the graph shows the annealing as described in the paper, with annealing for 4 hours in H_2, followed by cooling in Ar/H_2 overnight (annealing method 1). The blue curve represents an annealing method 2. In this method, the particles were annealed as described in method, but with a follow-up treatment of 15 minutes in which the particles were exposed to UV light in ozone. The goal was to remove any residual organics by oxidation after the surface was already annealed, to improve cleanliness. Finally, the orange curve shows annealing method 3, in which the particles were first annealed for 1 hour in pure oxygen to 300°C, to oxidize as many organics as possible, followed by a 3 hour annealing in H_2 to reduce surface oxides.

The effect on the CV is minimal. In the alternate annealing methods, the H_{upd} are is not as flat and (111)-like as in method 1, and OH adsorbtion has a slightly lower onset. The effect on the ORR activity is also minimal; the values are not shown as the catalysts exhibit identical kinetic activities within margin of error.

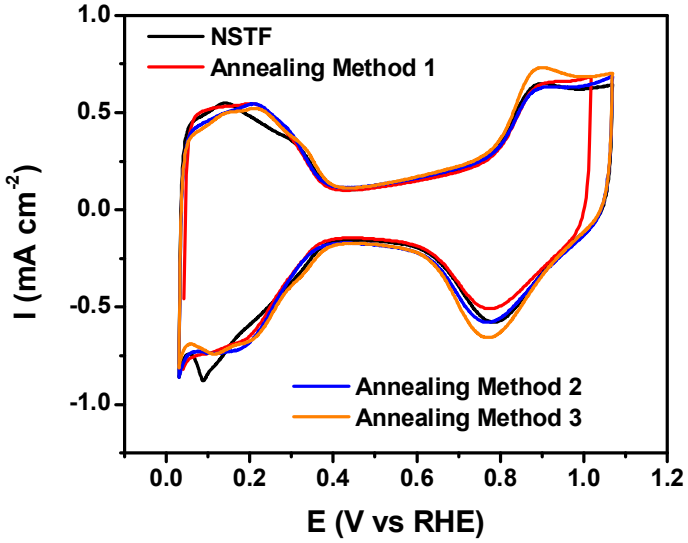

Figure 7.8. Effect of different annealing methods on the blank CV. Scans measured in 0.1 M $HClO_4$ with 50 mV s^{-1}. Black line represents the NSTF, the red, orange and blue lines represent annealing methods 1 through 3; for details see text.

7.5.4 Effect of annealing time

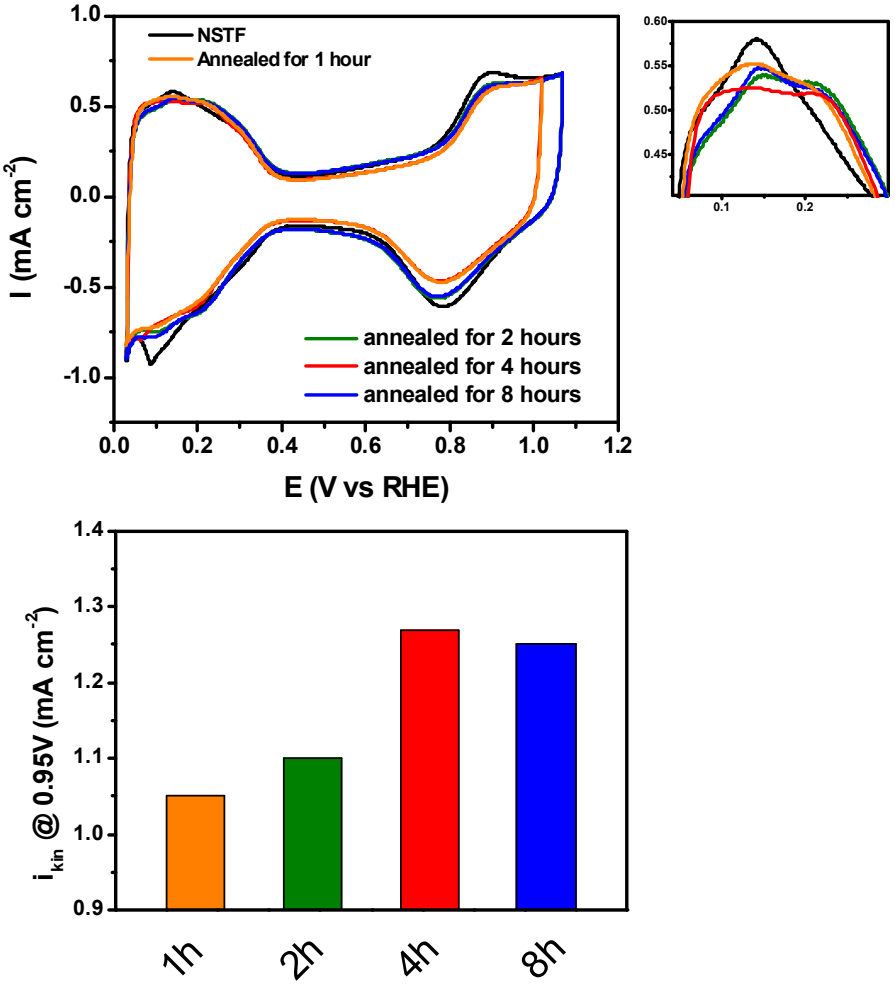

Figure 7.9. Effect of annealing time. Part A shows the blank cyclic voltammetries, with the inset a zoom in on the H_{upd} area of the curve. Black line represents the NSTF, orange, green, red and blue lines show the CVs for 1, 2, 4 and 8 hours annealing time, respectively.
Part B shows the effect on the kinetic current density for the ORR at 0.95V vs RHE, as measures in 0.1 M $HClO_4$ with 1600 rpm and 20 mV s^{-1}. Colors match those assigned in part A.

The duration of annealing was investigated as well. The particles were still gradually ramped up to a temperature of 400°C, but the duration they were kept at 400°C was varied. Blank CVs and ORR activities for these catalysts are shown in Figure 7.9. The zoom-in shows clearly the effect of annealing on the H_{upd} region of

the CV. The peak at 0.1 V, visible in the blank CV of PtNiFe NSTF is retained when the particles are only annealed for an hour, but the feature at 0.2V gets more pronounced with increasing annealing time. The onset of OH adsorbtion is identical in all catalysts. The apparent smaller double layer region (in between the H_{upd} and OH_{ads} regions) is due to the fact that the curves are showing current densities (normalized for surface area), where the double layer is geometrical surface area dependant. When the CVs are plotted showing the currents (non-normalized) then the double layers are equal in size and shape.
The ORR activities show a dependence on the annealing time. Up to 4 hours of annealing, the activity increases with increasing annealing time, and then remains essentially constant.

7.5.5 Effect on Active Surface Area

Figure 7.10 shows the active surface area in m^2 per gram catalyst used. It is assumed that the Pt content of the particles does not alter. This assumption is based on the fact that the Energy Dispersive X-ray (EDX) spectra of the catalyst after annealing (figure 7.11) shows the particles have the same composition within margins of error as before the annealing. Catalyst composition of the NSTF was supplied by 3M. The Pt content was 6% higher in the annealed particles, but that can be explained by the removal of the polymer substrate of the NSTF, see point 1 above.

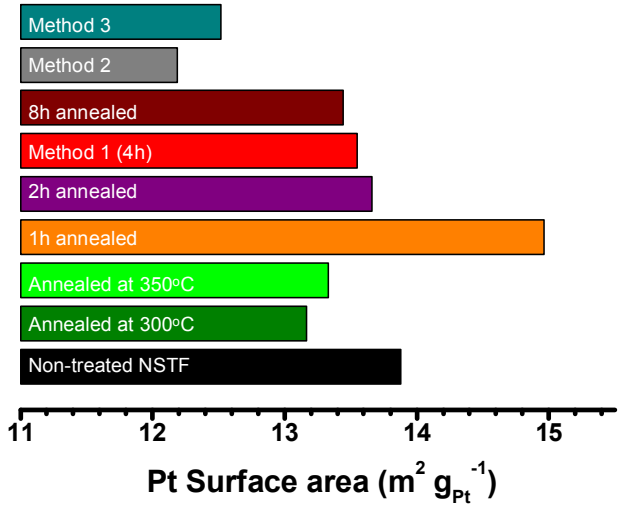

Figure 7.10. Effect of annealing treatment on the active surface area.

Shorter annealing times seem to give rise to a larger active surface area. This is because the removal of the polymer substrate is a faster process than the smoothening of the surface of the particles. Initially, the surface area is increased by making parts of the inside of the nanotubes available for catalytic reactions through removal of the perylene red; and at longer time scales the surface is slowly annealed and made smoother.

Because the kinetic activity for the ORR increases when the particles are smoother, the loss in surface area does not reflect in a loss of mass activity, on the contrary, mass activity is increased for the 4 hour annealed particles, compared to the 1 hour annealed catalyst, which in turn is more active per unit mass than the NSTF.

The alternative annealing methods show a decrease in active surface area. This is likely because part of the surface has oxidized irreversibly, and no longer shows activity towards hydrogen adsorption or ORR. This means that the mass activities are smaller than the particles annealed with Method 1.

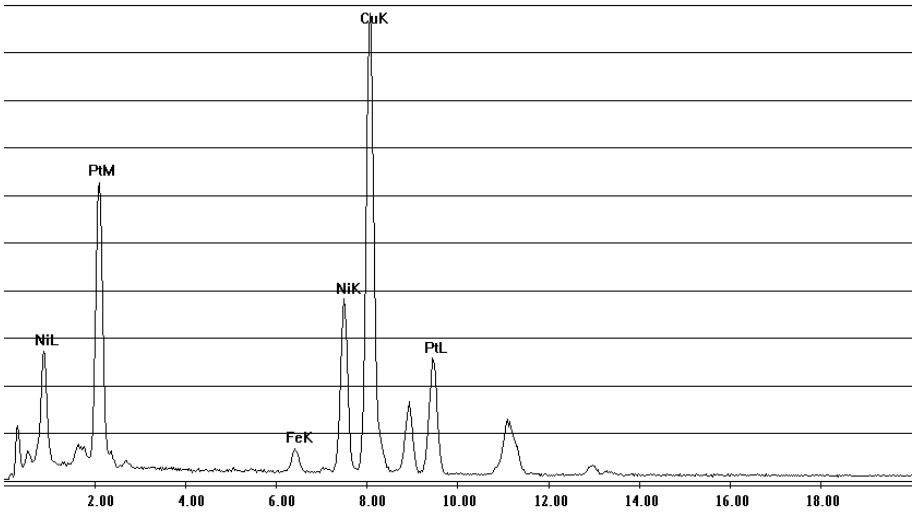

Figure 7.11. EDX spectrum of the 8 hour annealed particles.

References

[1] H. A. Gasteiger, S. S. Kocha, B. Sompalli, and F. T. Wagner, Applied Catalysis B-Environmental. 56 (2005) 9.

[2] H. A. Gasteiger, J. E. Panels, and S. G. Yan, Journal of Power Sources. 127 (2004) 162.

[3] K. J. J. Mayrhofer, B. B. Blizanac, M. Arenz, V. R. Stamenkovic, P. N. Ross, and N. M. Markovic, Journal of Physical Chemistry B. 109 (2005) 14433.

[4] J. X. Wang, N. M. Markovic, and R. R. Adzic, Journal of Physical Chemistry B. 108 (2004) 4127.
[5] L. Xiao, L. Zhuang, Y. Liu, J. T. Lu, and H. D. Abruna, Journal of the American Chemical Society. 131 (2009) 602.
[6] J. Hernandez, J. Solla-Gullon, E. Herrero, A. Aldaz, and J. M. Feliu, Journal of Physical Chemistry C. 111 (2007) 14078.
[7] L. G. R. A. Santos, K. S. Freitas, and E. A. Ticianelli, Electrochimica Acta. 54 (2009) 5246.
[8] A. S. Arico, P. Bruce, B. Scrosati, J. M. Tarascon, and W. Van Schalkwijk, Nature Materials. 4 (2005) 366.
[9] A. Atkinson, S. Barnett, R. J. Gorte, J. T. S. Irvine, A. J. Mcevoy, M. Mogensen, S. C. Singhal, and J. Vohs, Nature Materials. 3 (2004) 17.
[10] P. Strasser, S. Koh, T. Anniyev, J. Greeley, K. More, C. Yu, Z. Liu, S. Kaya, D. Nordlund, H. Ogasawar, M. F. Toney, and A. Nilsson, Nature Chemistry. Published online: 25 April 2010 | doi:10.1038/nchem.623 (2010).
[11] K. J. J. Mayrhofer and M. Arenz, Nature Chemistry. 1 (2009) 518.
[12] J. Greeley, I. E. L. Stephens, A. S. Bondarenko, T. P. Johansson, H. A. Hansen, T. F. Jaramillo, J. Rossmeisl, I. Chorkendorff, and J. K. Norskov, Nature Chemistry. 1 (2009) 552.
[13] D. Strmcnik, K. Kodama, D. van der Vliet, J. Greeley, V. R. Stamenkovic, and N. M. Markovic, Nature Chemistry. 1 (2009) 466.
[14] S. Gupta, D. Tryk, I. Bae, W. Aldred, and E. Yeager, Journal of Applied Electrochemistry. 19 (1989) 19.
[15] S. L. Gupta, D. Tryk, W. Aldred, I. T. Bae, and E. Yeager, Journal of the Electrochemical Society. 134 (1987) C129.
[16] M. Lefevre, E. Proietti, F. Jaouen, and J. P. Dodelet, Science. 324 (2009) 71.
[17] F. Jaouen, J. Herranz, M. Lefevre, J. P. Dodelet, U. I. Kramm, I. Herrmann, P. Bogdanoff, J. Maruyama, T. Nagaoka, A. Garsuch, J. R. Dahn, T. Olson, S. Pylypenko, P. Atanassov, and E. A. Ustinov, Acs Applied Materials & Interfaces. 1 (2009) 1623.
[18] R. Kothandaraman, V. Nallathambi, K. Artyushkova, and S. C. Barton, Applied Catalysis B-Environmental. 92 (2009) 209.
[19] K. Kendall, Nature Materials. 1 (2002) 211.
[20] V. R. Stamenkovic, B. Fowler, B. S. Mun, G. F. Wang, P. N. Ross, C. A. Lucas, and N. M. Markovic, Science. 315 (2007) 493.
[21] V. Stamenkovic, T. J. Schmidt, P. N. Ross, and N. M. Markovic, Journal of Physical Chemistry B. 106 (2002) 11970.
[22] V. R. Stamenkovic, B. S. Mun, K. J. J. Mayrhofer, P. N. Ross, and N. M. Markovic, Journal of the American Chemical Society. 128 (2006) 8813.
[23] M. R. Miah and T. Ohsaka, Electrochimica Acta. 54 (2009) 5871.
[24] F. Tian and A. B. Anderson, Journal of Physical Chemistry C. 112 (2008) 18566.
[25] S. Koh and P. Strasser, Journal of the American Chemical Society. 129 (2007) 12624.
[26] M. H. Shao, T. Huang, P. Liu, J. Zhang, K. Sasaki, M. B. Vukmirovic, and R. R. Adzic, Langmuir. 22 (2006) 10409.
[27] V. R. Stamenkovic, B. S. Mun, M. Arenz, K. J. J. Mayrhofer, C. A. Lucas, G. F. Wang, P. N. Ross, and N. M. Markovic, Nature Materials. 6 (2007) 241.
[28] J. L. Zhang, M. B. Vukmirovic, Y. Xu, M. Mavrikakis, and R. R. Adzic, Angewandte Chemie-International Edition. 44 (2005) 2132.

[29] S. Mukerjee and S. Srinivasan, Journal of Electroanalytical Chemistry. 357 (1993) 201.
[30] U. A. Paulus, A. Wokaun, G. G. Scherer, T. J. Schmidt, V. Stamenkovic, N. M. Markovic, and P. N. Ross, Electrochimica Acta. 47 (2002) 3787.
[31] U. A. Paulus, A. Wokaun, G. G. Scherer, T. J. Schmidt, V. Stamenkovic, V. Radmilovic, N. M. Markovic, and P. N. Ross, Journal of Physical Chemistry B. 106 (2002) 4181.
[32] T. Toda, H. Igarashi, H. Uchida, and M. Watanabe, Journal of the Electrochemical Society. 146 (1999) 3750.
[33] F. J. Lai, L. S. Sarma, H. L. Chou, D. G. Liu, C. A. Hsieh, J. F. Lee, and B. J. Hwang, Journal of Physical Chemistry C. 113 (2009) 12674.
[34] P. Mani, R. Srivastava, and P. Strasser, Journal of Physical Chemistry C. 112 (2008) 2770.
[35] Y. Tamura, K. Taneda, M. Ueda, and T. Ohtsuka, Corrosion Science. 51 (2009) 1560.
[36] F. H. B. Lima, J. F. R. de Castro, L. G. R. A. Santos, and E. A. Ticianelli, Journal of Power Sources. 190 (2009) 293.
[37] K. J. J. Mayrhofer, D. Strmcnik, B. B. Blizanac, V. Stamenkovic, M. Arenz, and N. M. Markovic, Electrochimica Acta. 53 (2008) 3181.
[38] S. Mukerjee, S. Srinivasan, M. P. Soriaga, and J. Mcbreen, Journal of the Electrochemical Society. 142 (1995) 1409.
[39] S. Mukerjee, S. Srinivasan, M. P. Soriaga, and J. Mcbreen, Journal of Physical Chemistry. 99 (1995) 4577.
[40] L. Gancs, T. Kobayashi, M. K. Debe, R. Atanasoski, and A. Wieckowski, Chemistry of Materials. 20 (2008) 2444.
[41] T. J. Schmidt, H. A. Gasteiger, G. D. Stab, P. M. Urban, D. M. Kolb, and R. J. Behm, Journal of the Electrochemical Society. 145 (1998) 2354.
[42] A. J. Bard and L. R. Faulkner, Electrochemical Methods, J. Wiley & Sons, New York, 1980.
[43] V. Stamenkovic, T. J. Schmidt, P. N. Ross, and N. M. Markovic, Journal of Electroanalytical Chemistry. 554 (2003) 191.
[44] D. S. Strmcnik, D. V. Tripkovic, D. van der Vliet, K. C. Chang, V. Komanicky, H. You, G. Karapetrov, J. Greeley, V. R. Stamenkovic, and N. M. Markovic, Journal of the American Chemical Society. 130 (2008) 15332.
[45] M. K. Debe and A. R. Drube, Journal of Vacuum Science & Technology B. 13 (1995) 1236.
[46] M. K. Debe and R. J. Poirier, Journal of Vacuum Science & Technology a-Vacuum Surfaces and Films. 12 (1994) 2017.
[47] M. K. Debe, A. K. Schmoeckel, G. D. Vernstorn, R. Atanasoski, Journal of Power Sources. 161 (2006) 1002.
[48] J.C. Serrano-Ruiz, A. López-Cudero, J. Solla-Gullón, A. Sepúlveda-Escribano, A. Aldaz and F. Rodríguez-Reinoso, Journal of Catalysis. 253 (2008) 159.
[49] N. M. Markovic and P. N. Ross, Surface Science Reports. 45 (2002) 117.

Chapter 8

Electrochemistry of Pt (100) in Alkaline Media: A Voltammetric Study

Pt (100) is one of the fcc metal surface planes that reconstruct upon annealing at high temperatures. The state of the surface is important in electrochemistry, in order to correlate catalytic behavior with surface structure. Therefore, the behavior of single crystalline Pt (100) in alkaline media was investigated, with particular attention paid to surface long range order. It was found that, in line with previous results, the manner of cooling the crystal after annealing influenced the state of surface significantly, with a profound effect on blank cyclic voltammetry as well as on carbon monoxide oxidation. Different ratios of inert and reductive gases were used to see if an optimal mixture could be obtained. Using air, argon, hydrogen, CO, and combinations of these gases gave rise to different states of the surface, with clear observable differences in blank voltammetric behavior and CO stripping. Also, the effect of alkali-metal cations and bromide on the blank and CO stripping voltammetry was investigated. Our main conclusion is that cooling in a carbon monoxide containing gas gives a clean, almost defect-free surface with long-range 1x1 symmetry. A similar surface can also be prepared with a hydrogen-containing cooling gas, but the content of hydrogen in that stream is critical.

The contents of this chapter have been accepted: D. van der Vliet and M.T.M. Koper, *Surf. Sci.* **(2010),** DOI: 10.1016/j.susc.2010.07.027

8.1 Introduction

For many decades now, single crystalline electrodes have been successfully used in surface electrochemistry, in an effort to correlate catalytic behavior with surface morphology. Especially the basal planes of the most dominant catalytic metal, platinum, have been used extensively in the literature. To understand catalytic trends, knowing the physical state of the surface is of utmost importance, which is why many surface sensitive techniques such as STM have been of valuable use in electrochemistry. [1-3]

On the three low-index planes of Pt, the (100) plane often exhibits the highest catalytic activity, especially for bond-making and bond-breaking reactions. [4-12] Therefore, reliably preparing a (100) surface with long-range order is key to understanding structure sensitivity in electrocatalysis. However, Pt (100) is considered to be a difficult surface to prepare in electrochemistry, reproducibility generally being an issue. From vacuum studies, it is known that Pt (100), as well as Pt (110) form reconstructed surfaces upon annealing [7, 8, 13-22]. This reconstruction can be lifted when the electrode is cooled in H_2, CO or NO. [7, 22, 23] Electrochemical studies confirmed that the reconstruction is (partially) retained, even if the crystal is transferred to an electrochemical cell, in contact with acid electrolyte [23-25]. For alkaline media, many different reports in which Pt (100) was used have been published. [4, 10, 26-33] In these papers, the blank cyclic voltammetry (CV) is not well defined; compare for example [10, 27] with [4, 28], in which the blank CVs look significantly different. This reinforces the belief that Pt (100) is a difficult surface to work with. In all reports, the CV exhibits four features on both the positive and the negative scan between 0.2V and 0.7V versus RHE, but in [10, 27], the peak at about 0.4V vs. RHE is dominant, whereas in [4], the peak at about 0.5V is largest. The other difference lies in the fourth peak at 0.6V, suggested to be caused by OH adsorption [26]. This peak is far more pronounced in [4] than in [10, 27]. When planes vicinal to the Pt (100) surface are considered, the blank cyclic voltammetry shows a clear trend towards an increase in the peak at 0.4 V with smaller terrace size [4, 28], suggesting that this peak is related to one-dimensional ordered (100) step sites. Simultaneously, the peaks that were present at potentials higher than 0.42 V significantly reduced in size, suggesting that these features are linked to two-dimensional ordered (100) domains. [4] The vicinal

planes considered had (100) terraces and (111) steps, which remain unreconstructed after flame-annealing [34].

The role of flame-annealing and cooling atmosphere was previously demonstrated with Pt (111) in acid [35] and alkaline [36] media, where no visible difference in blank cyclic voltammetry was found, but the manner of electrode preparation did have a large effect on catalysis. Preliminary findings in our group [37] show that for Pt (100) the pretreatment has an effect on both blank CV and CO oxidation. Dependence of the peaks at 0.4 and 0.5 V vs. RHE on the pretreatment method was found, as well as the increase in CO stripping peak potential for hydrogen/argon or CO/argon cooled crystals compared to the argon cooled electrode.

A more detailed investigation into the features observed in the blank cyclic voltammetry, and their dependence on cooling atmosphere is reported in this communication. We use voltammetric techniques in correlation with the STM images of Kibler *et al.* in sulfuric acid [23] to interpret the features that arise in blank cyclic voltammetry of Pt (100) in alkaline media. Furthermore, we discuss various ways of pre-treating the electrode before immersion in the electrochemical cell, and show the effects on the blank CV and catalytic activity for oxidative stripping of carbon monoxide, hereafter referred to as CO stripping. From vacuum studies, it is known that CO forms different adsorbate structures on reconstructed Pt (100) compared to unreconstructed Pt (100). [21] Furthermore, in accordance with the recently published results on Pt (111) [38], we show that alkali-metal cations influence both the blank cyclic voltammetry of Pt (100), and the activity for CO stripping. Finally, we introduce anions and compare the results with Pt (533), which has terraces of (111) geometry with (100) steps, to conclusively assign the observed peaks in the blank CV to specific surface processes.

8.2 Materials and Methods

We used bead-type single crystals of platinum with a diameter of *ca.* 3 mm. They were prepared by flame annealing at a fixed position in a natural gas Bunsen burner, with an identical position and flame for each annealing, and controlled cooling in a cooling gas stream. When no carbon monoxide was present in the cooling gas, the electrode was immersed in water saturated with the cooling gas before being transferred to the electrochemical cell. With CO in the cooling gas stream, the electrode was covered with CO after cooling, and protection with a drop of water

was not necessary, as the electrode was already protected by the CO. The crystal was immersed in the electrolyte under potential control at 0.1 V versus RHE.
We used a Teflon cell of similar design to the one used before [38], with a Pt wire as the counter electrode. All experiments were performed with an Autolab PGSTAT 12 with a noise-reducing capacitor between the reference electrode and a second Pt counter electrode in the cell. The reference used was a calomel electrode, separated by a salt bridge from the main cell compartment. All potentials reported are converted to the pH independent reversible hydrogen electrode (RHE) scale.
The electrolytes were prepared by dissolving the selected hydroxides in 18.2 MΩ cm resistive Milli-Q water. $KOH{\cdot}xH_2O$ was obtained from Fluka; TRACEselect ≥99.995% trace metals basis (tmb). The NaOH and LiOH used were from Sigma-Aldrich; both pellets of 99.995% tmb. CsOH H_2O was also obtained from Sigma-Aldrich; 99.95% tmb, and finally KBr was used with a purity of 99.95% tmb, also from Sigma-Aldrich. All gases were of scientific grade (N5.5 or higher).

8.3 Results

8.3.1 Effect of electrode preparation method

To correlate our surfaces to the STM images by Kibler *et al.* [23], we used essentially the same methods of cooling the electrode after flame annealing, with the only difference that we substituted argon for N_2. Pure carbon monoxide (CO) was used, as well as pure hydrogen, to give as large a contrast with cooling in argon and air as possible. CO was adsorbed from solution for the electrodes, with the exception of the CO-cooled crystal, where the carbon monoxide was obviously present on the electrode when transferring to the cell. For the CO cooled crystal, CO stripping was performed with the CO present on the electrode from the cooling gas.
Figure 8.1A shows the blank cyclic voltammetries (CVs) of the same Pt (100) crystal in 0.1M KOH, when cooled in these alternate ways. The two most striking features are the peaks in the positive-going scan at 0.4 V and 0.48 V. In the negative-going scan they are mirrored by peaks at 0.46V and 0.38 V, thereby showing some modest irreversibility. The peak at 0.46V in the reverse scan is significantly smaller than the peak at 0.48V in the positive scan. An interesting observation is the dependence of these peaks on the cooling method. One observes

that the peaks at 0.38V and 0.4V are most pronounced when the electrode is cooled in argon or air; and the peaks at 0.46V and 0.48V are most pronounced when the electrode is cooled in hydrogen or CO. In fact, when the electrode is cooled in air, the pair of peaks at 0.46V and 0.48V completely disappears. The order in size of this peak is CO > H_2 >> Ar > air. A hydrogen-cooled Pt (100) shows a small peak at 0.4V, which is almost absent on the CO-cooled electrode. Furthermore, the current in the potential region from 0.3V to 0.5 V is higher for the H_2 cooled crystal than for the CO cooled crystal. At a potential of 0.3V, features corresponding to hydrogen adsorption on Pt (110) sites are visible for each preparation method. The next noticeable difference in the CVs can be seen at 0.3V in the negative-going scan, where a broad feature is visible when the electrode is cooled in hydrogen or CO, whereas this feature is absent after air or argon cooling. The third significant change is visible at 0.6V, where small peaks are visible for the H_2 and CO cooled electrode, but in the case of argon and air cooling only a broad region remains. Finally, the region negative of all the peaks, with a potential lower than 0.2V, shows a significant increase of current density in the order of CO < H_2 < Ar < air.

When the charge of the CV up to 0.53 V is analyzed, a value of 250 μC $cm_{geom.}^{-2}$ is found. This is 25% more than the charge for a monolayer of hydrogen on a flat Pt surface and can be explained by an excess of Pt atoms on the surface due to the lifting of the reconstruction. The reconstructed hex-phase is about 24% more densely packed than the unreconstructed surface. Upon cooling the crystal after annealing, small islands formed by the excess Pt atoms will arise on the surface due to the lifting of the reconstruction. [23] These islands may in turn increase the charge of the blank CV and explain why the value is higher than for a single monolayer on atomically flat Pt.

The CO stripping curves on the various electrodes are very different as well. Figure 8.1B shows the positive-going scan; and figure 8.1C the subsequent negative-going scan after CO has been stripped off. The shift in stripping peak potential (1B) is very noticeable, and increases in the order air < Ar < H_2 < CO. The charge of the CO stripping is equal for all methods of cooling, except for the air-cooled one, which has a 10% reduced charge. This is a slightly different result from what Rodriguez *et al.* found [37], and can be explained by the fact that their electrode was quenched after cooling in air until it was no longer glowing, and the electrode in our case was cooled in air to room temperature, thereby increasing the likelihood of contamination to adsorb on the electrode. Also, their method of quenching increases the amount of defects, which may explain their increased CO stripping charge. For all other methods of cooling described here, the CO stripping charge is

comparable to the results of Rodriguez *et al.* [37]. The second consecutive scan for all electrodes (shown in figure 8.1A as blanks) shows no sign of CO, indicating a clean, CO-free electrolyte. The negative-going scan, visible in 1C, is slightly different from the negative-going scan in the consecutive sweep (1A). At a potential of 0.27V, a large reductive peak is visible when the electrode is cooled in hydrogen or CO. The fact that this peak reduces in size upon cycling, compare for example with the second cycle in figure 8.1A, hints at a surface change. This peak is absent when the electrode is cooled in argon or air. Interestingly, this feature agrees with the (110) peaks mentioned before.

Next, the dependence of the surface state as a function of a hydrogen-argon cooling mixture was investigated. This mixture is commonly used in the flame annealing of single crystal electrodes. The results are depicted in figure 8.2. Similar to figure 8.1, part A of figure 8.2 shows the blank cyclic voltammetry (the second consecutive scan after CO stripping), B shows the CO stripping itself, and C the negative-going scan following the stripping curve. A range of ratios from Ar:H_2 6:1 through 1:2 was measured, though only curves corresponding to three ratios are shown. The black curve represents the electrode cooled in pure argon for comparison, and the green curve shows the pure H_2-cooled crystal. Blue, orange and red show the 5:1, 3:1 and 1:1 ratios of Ar:H_2, respectively. CO was adsorbed from the solution for electrodes cooled in this way, before any blank cyclic voltammetry was measured.

The first thing that is notable is the shift in peak potential of CO stripping, shown in figure 8.2B. The more hydrogen used in cooling, the more positive the CO stripping peak, up to a mixture of about 1:1, which resembles the pure hydrogen cooled electrode. When the blank CVs are compared (2A), three transitions are very distinct. First, the main peak at 0.48V gets smaller with less hydrogen in the cooling stream, and it shifts to lower potentials, becoming more reversible with the negative-going peak at 0.46V. Second, the feature slightly positive of 0.4V shifts negative to coincide in position with the peak observed at 0.4V on the Ar-cooled electrode, and increases slightly in size. And finally, in the negative-going scan, the feature at 0.3V decreases with decreasing hydrogen content in the cooling stream. Less distinct, but definitely noticeable is the decrease in the features at 0.6V with decreasing H_2 content. The reverse scan after CO stripping (2C) has a clear feature at 0.3V, where it can be seen that the pure hydrogen cooled electrode has a single peak, and the 1:1 cooled electrode has a shoulder slightly positive of the peak. When the mixture is made less hydrogen-rich, the feature changes completely to show the (110) peak at 0.27V and a peak at 0.38V that was also observed on air and argon cooled electrodes.

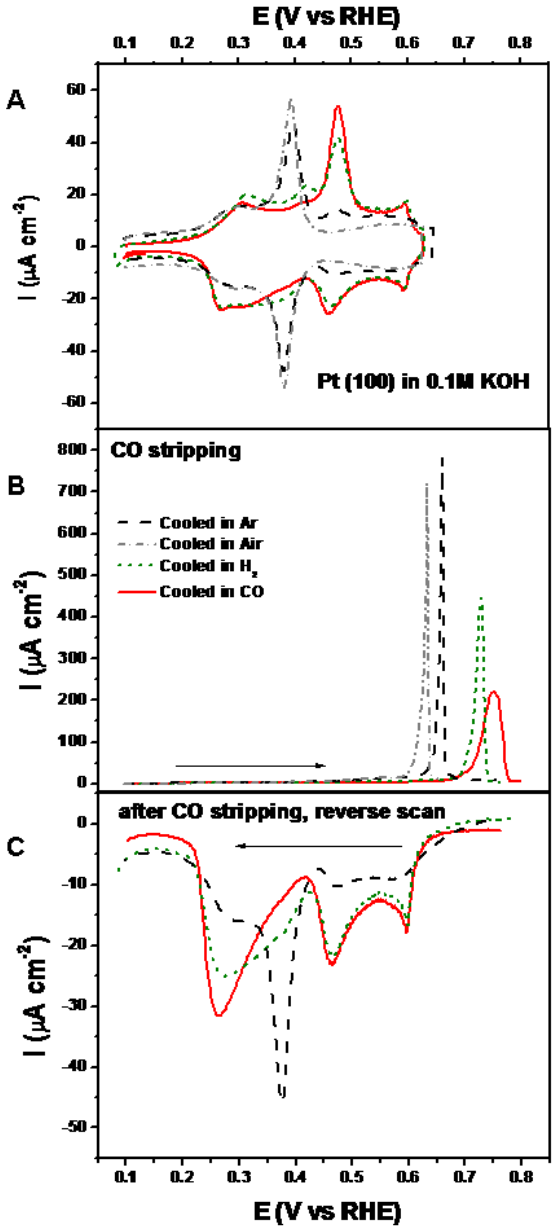

Figure 8.1. A. Blank cyclic voltammetry of Pt (100). The different curves represent Pt (100), cooled in pure Argon (black), pure hydrogen (green), pure CO (red) and air (grey). Part B shows the positive going scan CO stripping curve, and C the negative going scan. All scans were made in 0.1M KOH, with a scan rate of 20 mV s^{-1}.

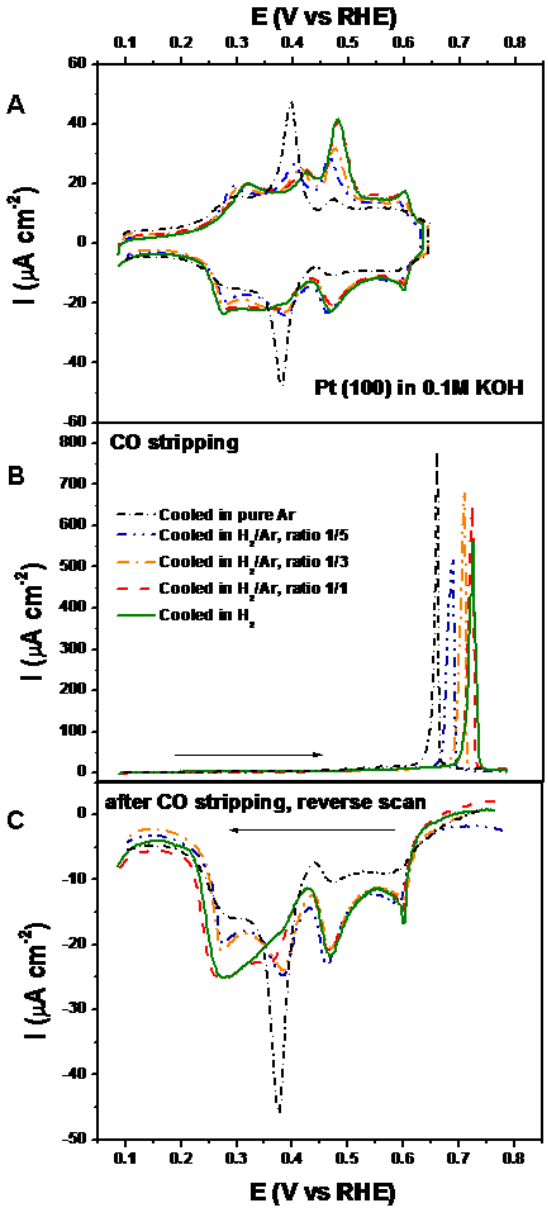

Figure 8.2. Dependence of blank cyclic voltammetry (A) and CO stripping (B in positive going scan, C in negative) on cooling method when using a mixture of Ar/H_2. All scans were made in 0.1 M KOH at 20 mV s^{-1}. The black line and grey line show reference voltammetries of Pt (100) cooled in argon and air, respectively. Blue (1/6), orange (1/3), red(1/1) and green (2/1) curves show an increasing order in (hydrogen/argon) content in the cooling gas flow.

Different CO to Ar ratios were applied as well, but the results (not shown graphically) were less clear-cut than for H_2:Ar cooled crystals. The trend was identical (higher CO stripping potential with increasing CO content in the cooling stream), but the reproducibility was more problematic, causing a wide scattering of peak potentials. This leads to the conclusion that when an electrode is cooled in a CO-containing inert gas stream, the amount of CO present is less critical than when cooled in a H_2:Ar gas stream; a stream containing small amounts of CO could lead to the same surface as when cooled in a high CO-content gas stream. In all CO-cooling experiments, however, one trend was clear: regardless of the CO-content in the cooling stream, the higher the CO stripping peak potential, the bigger, and at lower potential, the feature at around 0.28V in the negative-going scan.

8.3.2 Effect of potential cycling

The reason why CO stripping is performed before recording blank CVs can be deduced from figure 8.3. After cycling the electrode 5 times (orange curve) the peak at 0.48V has shifted slightly negative, and is reduced in height. This trend continues when the electrode is cycled more, as shown by the red curve obtained after 25 blank cycles and the blue curve obtained after 55 blank cycles. The blank cyclic voltammograms, shown in figure 8.3A, show the consecutive cycles after CO stripping, the cycles in-between were made to an upper limit of 0.6V vs. RHE. Simultaneously with the peak decrease at 0.48V, the feature at 0.4V increases with increasing numbers of cycles.

The CO stripping peak potential (figure 8.3B) shifts to lower potentials with increasing numbers of cycles, until it is stable for heavily cycled (more than 50 cycles) Pt (100). Combined with the obvious broadening of the peak, this is a clear indication that the surface morphology has changed. In the negative-going scan, the most negative features are shifting positive with increasing numbers of cycles. The results shown in the figure were made without losing potential control on the electrode, and in the same electrolyte. To exclude the effects of carbonate, formed while saturating the electrode with CO and subsequent oxidation, a series of blank cyclic voltammograms was also made without intermittent CO-stripping. These CVs show the same trend as the ones shown in figure 8.3A. Furthermore, scanning the electrode at lower scan rate, for example at 5 mV s^{-1}, will have a similar effect as many cycles at higher scan rate.

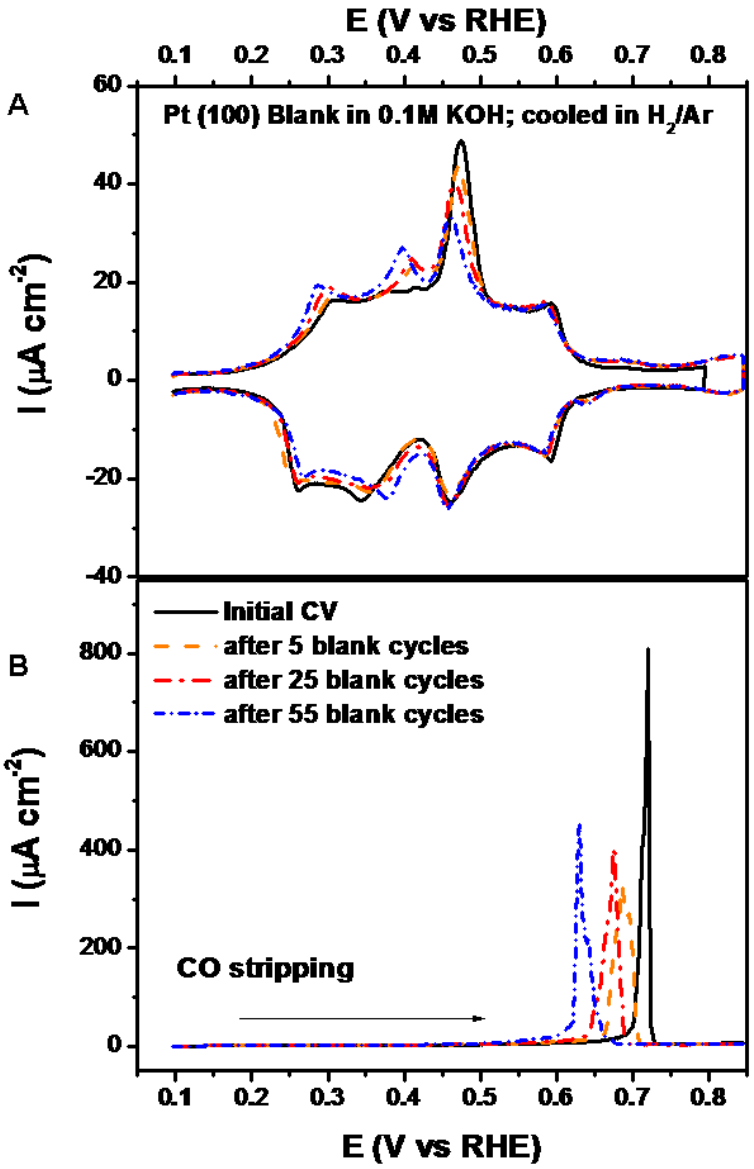

Figure 8.3. The effect of cycling in argon-purged solution up to a potential of 0.6V vs. RHE. In part A, the black graph shows the initial blank CV of H_2/Ar (1/3) cooled Pt (100), orange (5 cycles), red (25 cycles) and blue (55 cycles) show the voltammetries after their respective CO stripping (shown in part B). The electrode was cycled up to 0.6V in between the CO stripping curves. All scans were made in 0.1 M KOH at 20 mV s^{-1}.

8.3.3 Cation and Anion effects

Finally, the effects of cations and anions on the blank CV and CO stripping on Pt (100) were investigated. The results are shown in figure 8.4 (cation effect) and figure 8.5 (bromide effect). The blank cyclic voltammograms for the different metal hydroxide electrolytes (figure 8.4A) show three interesting trends. First of all, the most obvious of the three, is the influence on the pair of peaks with the highest potential of 0.6V. This peak sharpens when the cation is changed from Cs → K → Na → Li. In LiOH this gives what we interpret as a very small double-layer region between H desorption and OH adsorption, which normally is not observed on Pt (100). The second and third effects are coupled. The main peak at 0.48V, as well as the feature in the negative going scan at 0.28V, decreases in intensity when the cation is changed from Li to Cs. The feature at 0.28V is even more pronounced with the smaller cations in the negative-going scan after CO stripping (figure 8.4C). For lithium hydroxide this peak remains nearly identical in the consecutive blank scan (shown in part A). The CO stripping peak shows the trend that the peak potential decreases in the order $K \approx Cs > Na > Li$; the inset in figure 8.4B shows the peak potentials plotted for the various cations, with their standard deviations over 4 independent measurements.

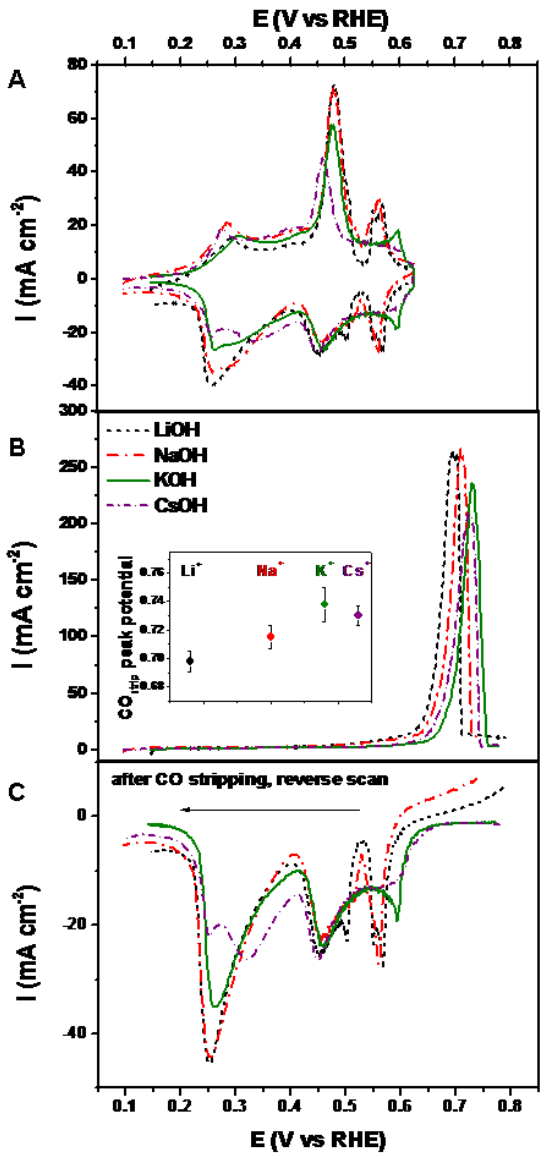

Figure 8.4. Effect of the alkali-metal cation. Part A shows the blank cyclic voltammetries, and B and C show CO stripping in positive, and negative-going scan, respectively. The inset in part B shows the peak potential as function of the cation, with the error bars representing the standard deviation in 4 independent measurements. All scans were made with the electrode cooled in 1:1 CO:Ar, then transferred to 0.1M MOH with M = Li (black) Na (red), K (green) and Cs (purple). Scans were made with 20 mV s^{-1}.

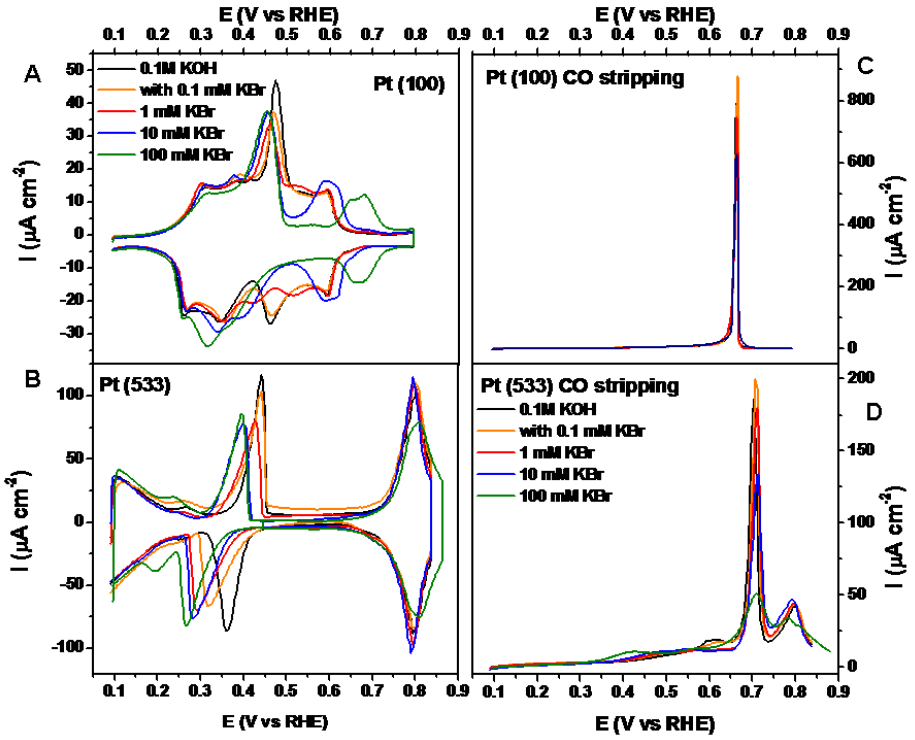

Figure 8.5. Effect of bromide on Pt (100) (A and C) and Pt (533) (B and D) A and B show the blank cyclic voltammetry, C and D illustrate CO stripping. The black line represents the blank CV in 0.1M KOH; orange, red, blue and green show the curves with an order of magnitude increase in bromide concentration each, starting at $1 \cdot 10^{-4}$ M. Blank scans were made with a scan rate of 50 mV s^{-1}, CO stripping was performed at 20 mV s^{-1}. The electrodes were cooled in 3:1 Ar:H_2 after annealing.

The effect of anions (bromide) on the blank CV is shown in figure 8.5. Part A shows the effect on H_2:Ar cooled Pt (100). The most striking effect is the change in OH adsorption features (peak at 0.6V). For less than 1 mM KBr, this peak remains essentially unaffected, but when the concentration is consecutively increased it shifts to much more positive potentials, giving rise to an extended "double-layer" region in which we assume the electrode to be covered with a Br-adlayer. In the negative-going scan, the peak at 0.46V seems to split. This is best visible in the 1 mM voltammetry, where two peaks are evident at 0.42V and 0.52V instead of a single one. For higher concentrations of bromide, these two peaks seem to shift even further apart; the more positive one coinciding with the OH peak, the most negative one visible as a shoulder on the peak at about 0.32V. The other feature in the negative-going scan at 0.35V is that it shifts steadily more negative with

increasing anion concentration. This is coupled to the positive-going scan, where the main peak at 0.48V also shifts negative with increasing bromide concentration. This trend is mirrored in figure 8.5B on Pt (533) (which has 4 atom wide (111) terraces and (100)-steps), where the features of hydrogen adsorption associated with the (100) step sites shift steadily negative when the bromide concentration is increased. This shows that these features are most definitely connected to hydrogen ads- and desorption. In contrast to Pt (100), the change on the OH adsorption on (111) terraces on Pt (533) is minimal, most likely due to the lower affinity of anions to (111) sites in alkaline media (see also [39]), causing the OH adsorption on (111) sites to be less influenced by anion coadsorption.

The effect of anions on CO stripping is illustrated in figure 8.5C and D for Pt (100) and Pt (533) respectively. For Pt (100) the only effect is that the stripping peak current gets lower, and that the whole feature broadens slightly. The total charge of CO stripping remains equal for all concentrations of bromide. On Pt (533) the effect is slightly more pronounced. The pre-oxidation wave (0.35-0.65V) starts at lower potentials for increased bromide concentration, while the main peak increases slightly in potential. The total CO stripping charge remains constant at about 340 μC cm^{-2} until the concentration bromide exceeds 10 mM; then it diminishes to about 310μC cm^{-2} for the Br^- concentration of 0.1M. This is likely due to competitive adsorption between Br^- and CO. As a reference, the CO stripping curves in bromide containing electrolyte for Pt (111) are shown in figure 8.6. Here can be seen that the bromide has little influence on the main peak potential. The onset of the pre-oxidation peaks remains the same for increased concentrations of bromide, but the charge of the pre-oxidation features decreases significantly. This once again shows that in alkaline media, bromide competes for the lower coordinated sites, but not for the (111) terraces.

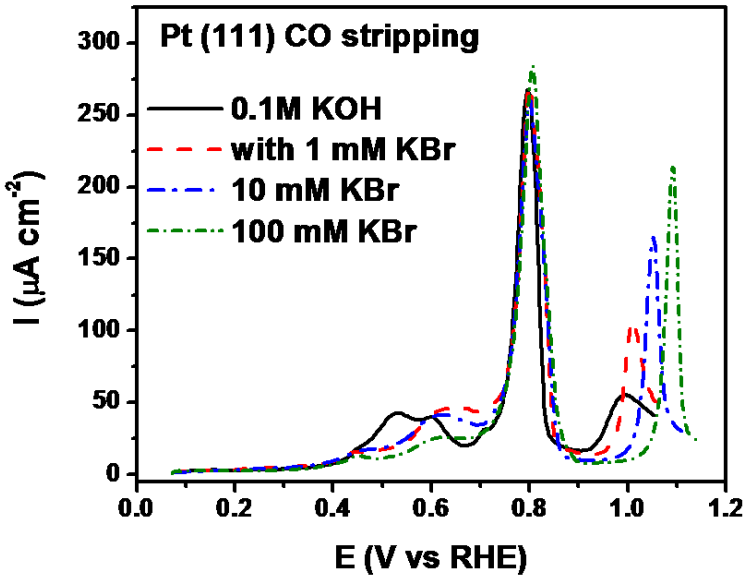

Figure 8.6. CO stripping on Pt (111) (with defects) in 0.1M KOH with increasing concentrations of bromide. The black line shows the CO stripping without bromides, the red, blue and green lines with 1 mM, 10 mM and 0.1 M KBr, respectively. Scan rate 50 mVs^{-1}. The electrode was cooled in 3:1 Ar:H_2 after annealing.

8.4 Discussion

In this section we will summarize our interpretation of the influence of surface preparation on the cyclic voltammetry and CO stripping. The pair of peaks at the lowest potentials (0.3 V) has been attributed to Pt (110)-type defects, due to their position which agrees with the hydrogen adsorption features on Pt (110). [4, 26] The next pair of peaks at 0.38V and 0.4V is most pronounced when the electrode is cooled without CO or hydrogen present (figure 8.1), and can be attributed to a mixture of defect sites and low-range order (100) sites. This is evident from the observation that these peaks grow when cooled in air, which is known to increase defects [23], and that they increase on the unreconstructed surfaces, vicinal to Pt (100) [4, 34]. Interestingly, these peaks also seem to be most pronounced for the argon-cooled surface, which was shown to be reconstructed in the electrolyte [23]. Regardless of their exact structural origin, they clearly do not represent long-range Pt (100) terraces.

Such long-range (100) terraces exhibit hydrogen adsorption/desorption features in two large peaks, which are separated significantly. In the positive-going scan, the main peak at 0.48V can be seen to diminish during cycling, and with less perfect cooling methods, thereby indicating its relationship to terraces of long-range order. This is coupled with the peak at 0.28V in the negative-going scan, which diminishes when the main peak at 0.48V grows smaller. There are two possible explanations for the diminishing of these peaks during cycling. First of all, it has been shown in figure 8.3 that cycling introduces defects, resulting in a reduction of long-range order. Secondly, hydrogen adsorption processes have been shown to lift a reconstructed surface [24, 25]. In our case, however, the features change most for CO and H_2 cooled surfaces, which were shown to be unreconstructed in the first place. [7] This reinforces our belief that the features at 0.48V in the positive-going scan and at 0.28V in the negative-going are very sensitive to the long-range Pt (100) order, and that both cooling in a non-reductive atmosphere and potential-cycling in an electrochemical cell reduce significantly the long-range order of a Pt (100) crystal.

We believe the nature of the processes that give rise to these features is ads- and desorption of hydrogen, combined with cation-stabilized adsorption of OH, similar to the model in [38]. As can be seen in figures 5A and 6A, the two features are dependent on the nature of the cation, as well as the bromide concentration, which is a clear indication that there is an anionic contribution to both features. The irreversibility that can be seen in the blank CV is most likely caused by the stability of the adsorbed anions and OH on the well-ordered surface. On less well-ordered surfaces (such as after many blank cycles, see figure 3), the interaction of these anionic species may be weaker, causing the CV to become more reversible with decreasing long-range order.

The final set of peaks that is visible in the blank cyclic voltammetry, centered at about 0.55-0.6V, can be attributed to OH adsorption. The fact that they shift positive when bromide adsorption is blocking the surface for OH_{ads} (figure 8.5), and that they sharpen when a more OH-interacting cation is used (figure 8.4) supports this conclusion. This peak-sharpening in itself can be explained by the model in [38], when one considers the (hydrated) metal cation to be quasi-specifically adsorbed through the OH_{ads} on the surface. Lithium, which has the strongest interaction with OH_{ads}, shows the sharpest peak, and cesium, which has the weakest interaction with OH_{ads}, exhibits the broadest feature.

Our results illustrate that it is important to prepare the crystal in a correct way. As figure 8.1B and figure 8.2B show, the preparation method can influence catalytic

properties dramatically . When cooling the crystal in a mixture of hydrogen and argon, as is usual in electrochemistry, a higher concentration of hydrogen (at least 50% hydrogen content in the cooling stream) is preferred to prepare a surface consisting of large well-ordered Pt (100) terraces. Better yet for long-range order is the inclusion of carbon monoxide in the cooling stream. Furthermore, as is evident from figure 8.3, making blank CVs is detrimental to the long-range order, and worse still, it will introduce defects as visible from the CO stripping in figure 8.3B. CO stripping in alkaline media is a structure-sensitive process [40], and defect sites have been shown to have the lowest peak potential for CO stripping. Therefore, when the peak potential reduces, and the peak broadens, as in figure 8.3B, it illustrates the formation of defects on the surface. Interestingly, the CO stripping peak potential after cycling the electrode for a long time is nearly identical to the CO stripping peak potential for the air-cooled electrode (figure 8.1B), reinforcing previous findings on the highly defected nature of the air-cooled crystal [23].

The cation effect on CO stripping is very clear: in the sequence Li < Na < K = Cs the stripping peak potential increases. The stronger the interaction of the metal-cation with OH, the stronger it will quasi-specifically adsorb on the surface. This also means that the stronger the M-OH interaction, the sooner it will be able to initiate the CO electro-oxidation through the Langmuir-Hinshelwood mechanism. The M-OH interaction increasing in the range Cs < K < Na < Li is exactly opposite of the CO stripping peak trend, which supports our conclusion of a higher affinity for CO stripping with increasing M-OH interaction. It is interesting to note that in a previous result on Pt (111) [38], the onset of methanol oxidation showed the same trend as the CO stripping in this work. The same result was obtained in our group for CO stripping from a Pt (111) surface. [41] Bromide seems to have little influence on the catalytic activity of Pt (100) towards CO stripping, but does have a profound effect on the adsorption processes which are visible in the blank cyclic voltammetry. Bromide competitively adsorbs with protons, shifting the adsorption features due to H_{upd} to slightly more negative potentials. Higher concentrations of bromide also delay surface oxidation, shifting the OH_{ad} feature of the (100) terraces more positive. In order to more accurately assign the peaks in the blank CV, Pt (533) was measured as well. The negative shift of the (100) step-related H_{upd} peak is mirrored on that surface, but anions do not have the same effect on the reversible OH_{ad} peak of the (111) terraces at 0.8V. This clearly shows the stronger interaction of bromides in alkaline media with the Pt (100) surface compared to Pt (111). For the catalytic activity towards the electro-oxidative stripping of CO the effect is minimal. It is interesting to note that when there are fewer (100) sites available,

such as on Pt (533), there is a bigger difference in CO stripping for the different Br^- concentrations. Likely Br^- is competing with active sites for the oxidation of adsorbed CO, which is more evident when fewer sites are available. On Pt (111), there is no difference in CO stripping main peak potential or charge with increasing bromide concentrations, but a significant effect on the pre-oxidation wave due to lower-coordinated defect sites. This indicates strongly that the difference in CO stripping main peak potential observed on Pt (533) must be due to the (100) sites present.

8.5 Conclusion

The mixture of gases in which the Pt (100) crystal is cooled after flame-annealing is critical to the quality of the surface structure. Blank cyclic voltammetry in alkaline media is very sensitive to the manner of surface preparation. Cooling in air and argon causes the surface to have far less long-range 1x1 order. Cooling in hydrogen-containing argon will give a much better surface, but the amount of hydrogen is important. The more hydrogen (up to 50%) present, the better the surface. The best preparation method to obtain long-range (100) islands is by cooling in a mixture of carbon monoxide and argon.

Differences in the literature on the blank cyclic voltammetry of Pt (100) are caused by a combination of this annealing methodology, the influence of cycling, as well as the difference in cation used. The OH_{ads} features of Pt (100) become sharper with increasing M-OH interaction in the order Cs < K < Na < Li. The CO stripping onset and peak position shifts in exactly the opposite order, with CO stripping in lithium having the lowest onset and peak potential.

Finally, the addition of bromides has the effect on the blank cyclic voltammetry that the peaks attributed to hydrogen adsorption and desorption shift to lower potentials with increasing bromide concentration, and the OH-peaks shift positive. At concentrations of $1 \cdot 10^{-4}$ M and higher, a “double-layer” becomes visible, where the H_{ads} and OH_{ads} processes are clearly separated by a region on which bromide is adsorbed on the electrode. There appears to be competition of bromide adsorption with CO oxidation for (100) sites, which is evident from the difference in CO stripping curves on Pt (533). This effect is not observed on Pt (100), most likely due to the increased availability of these sites. Anion adsorption on Pt (111) in alkaline media is weak, and there such a competition is not observed.

References

[1] K. Itaya, Progress in Surface Science. 58 (1998) 121.
[2] G. Jerkiewicz, Solid-Liquid Electrochemical Interfaces. 656 (1997) 1.
[3] A. A. Gewirth and B. K. Niece, Chemical Reviews. 97 (1997) 1129.
[4] F. J. Vidal-Iglesias, N. Garcia-Araez, V. Montiel, J. M. Feliu, and A. Aldaz, Electrochemistry Communications. 5 (2003) 22.
[5] V. Rosca, G. L. Beltramo, and M. T. M. Koper, Journal of Physical Chemistry B. 108 (2004) 8294.
[6] L. Vattuone, L. Savio, and M. Rocca, Surface Science Reports. 63 (2008) 101.
[7] M. Brandt, G. Zagatta, N. Bowering, and U. Heinzmann, Surface Science. 385 (1997) 346.
[8] H. P. Bonzel, G. Broden, and G. Pirug, Journal of Catalysis. 53 (1978) 96.
[9] W. K. Offermans, A. P. J. Jansen, R. A. van Santen, G. Novell-Leruth, J. M. Ricart, and J. Perez-Ramirez, Journal of Physical Chemistry C. 111 (2007) 17551.
[10] T. J. Schmidt, P. N. Ross, and N. M. Markovic, Journal of Physical Chemistry B. 105 (2001) 12082.
[11] R. A. Van Santen, Accounts of Chemical Research. 42 (2008) 57.
[12] V. Rosca and M. T. M. Koper, Physical Chemistry Chemical Physics. 8 (2006) 2513.
[13] M. A. Vanhove, R. J. Koestner, P. C. Stair, J. P. Biberian, L. L. Kesmodel, I. Bartos, and G. A. Somorjai, Surface Science. 103 (1981) 189.
[14] M. A. Vanhove, R. J. Koestner, P. C. Stair, J. P. Biberian, L. L. Kesmodel, I. Bartos, and G. A. Somorjai, Surface Science. 103 (1981) 218.
[15] D. L. Abernathy, D. Gibbs, G. Grubel, K. G. Huang, S. G. J. Mochrie, A. R. Sandy, and D. M. Zehner, Surface Science. 283 (1993) 260.
[16] D. L. Abernathy, S. G. J. Mochrie, D. M. Zehner, G. Grubel, and D. Gibbs, Physical Review Letters. 69 (1992) 941.
[17] D. L. Abernathy, S. G. J. Mochrie, D. M. Zehner, G. Grubel, and D. Gibbs, Physical Review B. 45 (1992) 9272.
[18] D. Gibbs, G. Grubel, D. M. Zehner, D. L. Abernathy, and S. G. J. Mochrie, Physical Review Letters. 67 (1991) 3117.
[19] P. Heilmann, K. Heinz, and K. Muller, Surface Science. 83 (1979) 487.
[20] J. Clavilier, R. Durand, G. Guinet, and R. Faure, Journal of Electroanalytical Chemistry. 127 (1981) 281.
[21] G. Broden, G. Pirug, and H. P. Bonzel, Surface Science. 72 (1978) 45.
[22] J. Radnik, F. Gitmans, B. Pennemann, K. Oster, and K. Wandelt, Surface Science. 287 (1993) 330.
[23] L. A. Kibler, A. Cuesta, M. Kleinert, and D. M. Kolb, Journal of Electroanalytical Chemistry. 484 (2000) 73.
[24] A. Al-Akl, G. A. Attard, R. Price, and B. Timothy, Journal of Electroanalytical Chemistry. 467 (1999) 60.
[25] K. Wu and M. S. Zei, Surface Science. 415 (1998) 212.
[26] N. M. Markovic, H. A. Gasteiger, and P. N. Ross, Journal of Physical Chemistry. 100 (1996) 6715.
[27] A. V. Tripkovic, K. D. Popovic, J. D. Momcilovic, and D. M. Drazic, Journal of Electroanalytical Chemistry. 448 (1998) 173.
[28] N. Furuya and M. Shibata, Journal of Electroanalytical Chemistry. 467 (1999) 85.

[29] T. J. Schmidt, P. N. Ross, and N. M. Markovic, Journal of Electroanalytical Chemistry. 524-525 (2002) 252.
[30] A. Rodes, V. Climent, J. M. Orts, J. M. Perez, and A. Aldaz, Electrochimica Acta. 44 (1998) 1077.
[31] E. Morallon, J. L. Vazquez, and A. Aldaz, Journal of Electroanalytical Chemistry. 288 (1990) 217.
[32] J. H. Barber and B. E. Conway, Journal of Electroanalytical Chemistry. 461 (1999) 80.
[33] F. J. Vidal-Iglesias, J. Solla-Gullon, V. Montiel, J. M. Feliu, and A. Aldaz, Journal of Physical Chemistry B. 109 (2005) 12914.
[34] N. Garcia-Araez, V. Climent, E. Herrero, and J. M. Feliu, Surface Science. 560 (2004) 269.
[35] N. P. Lebedeva, M. T. M. Koper, J. M. Feliu, and R. A. van Santen, Electrochemistry Communications. 2 (2000) 487.
[36] G. Garcia, P. Rodriguez, V. Rosca, and M. T. M. Koper, Langmuir. 25 (2009) 13661.
[37] P. Rodriguez, G. Garcia, E. Herrero, J. M. Feliu, and M. T. M. Koper, in preparation, to be submitted. (2010).
[38] D. Strmcnik, K. Kodama, D. van der Vliet, J. Greeley, V. R. Stamenkovic, and N. M. Markovic, Nature Chemistry. 1 (2009) 466.
[39] R. Gisbert, G. García, and M. T. M. Koper, Electrochimica Acta. In Press, Corrected Proof.
[40] G. Garcia and M. T. M. Koper, Physical Chemistry Chemical Physics. 10 (2008) 3802.
[41] C. Stoffelsma and M. T. M. Koper, In preparation.

Summary

Work for this thesis started at Argonne National Laboratory (ANL), and in the final year the assembling of this thesis has been performed at Leiden University.
Relevant processes for fuel cells such as the oxygen reduction reaction (ORR) and CO electro-oxidation are studied and described in this thesis. The goal of this research was to find the origin of catalytic activity of Pt-alloys for these reactions, and specifically to use this knowledge to develop new active catalysts for the ORR. In order to effectively pursue this goal, it was necessary to improve the reliability of the comparison between model rotating disk electrode (RDE) experiments and *in-situ* membrane electrode assembly (MEA) testing. Improvement of the RDE method will allow for faster catalyst screening, thereby decreasing the development time. The outcome is extremely useful in the development of fuel cells and reducing the dependence on fossil fuels, while at the same time reducing harmful emissions.
In order to facilitate these goals, several techniques have been applied. First of all, basic electrochemical methods such as cyclic voltammetry (CV) and impedance spectroscopy have been used to study adsorption and reactions on the electrode, as well as the effect of electrolyte resistance. The previously mentioned RDE measurements allowed for effectively reducing the influence of diffusion so that the kinetic activity towards the ORR could be screened for various catalysts. In addition, non-electrochemical supplementary techniques have been applied to confirm catalyst structures. These techniques include *ex-situ* electron microscopy, such as scanning tunneling miscroscopy (STM), scanning electrode microscopy (SEM) and transmission electron microscopy (TEM). Added to this was elemental mapping by high angle annular dark field scanning transmission electron microscopy (HAADF-STEM) and Energy-dispersive X-ray scattering (EDX). X-ray diffraction (XRD) was applied as well to observe nanoparticle size, composition and crystallinity.
Theory was used by cooperating groups to support our experimental findings and explain observed trends. Density functional theaory (DFT) calculations were performed by J. Greeley at the center for nanoscale materials at ANL, and Monte Carlo simulation by G.Wang at Purdue University.

The thesis opens in Chapter 2 with a detailed investigation of an intrinsic problem of working with electrically conducting electrolyte: electrolyte resistance. This resistance causes a deviation of the actual potential at the electrode from the applied potential by the potentiostat at higher currents; for example when currents are high due to a reduction in diffusion limitation in a RDE measurement. As this resistance is very different in magnitude from that observed in a MEA, this may lead to differences in interpretation. The chapter further deals with the influence of adsorption processes on the electrode during the ORR in the RDE experiments, another deviation from the steady-state operation of the MEA. As resistance and superimposed adsorption currents are relatively easy to compensate for, after proper compansation has been applied, the RDE method will be more accurate when comparing the data in the following chapters with MEA measurements in the literature.

The oxygen reduction reaction (ORR) on platinum-containing nanoparticles (NPs) is reported in detail in chapters 3-7. Pt_3Co nanocatalysts were synthesized and characterized (chapters 3 and 4), with special care taken of the pretreatment and its effect on particle size and corresponding ORR activity. A volcano-shaped dependence of mass activity depending on particle size was found, due to the opposite trends that for increasing particle size the kinetic current density increases, but the specific surface area per unit mass decreases. The optimal particle size of these Pt_3Co particles is shown to be 4.5 nm.
Novel core-shell particles, dispersed on carbon, are discussed in chapter 5. These particles have a gold core and Pt_3Fe shell and are shown to have not only increased activity for the ORR, but also increased stability due to their lower rate of agglomeration.
Non-carbon supported nanostructured thin film (NSTF) catalysts are discussed in chapters 6 and 7. Chapter 6 deals with the determination of the optimal catalyst loading and determination of ORR activities of non-modified NSTF catalysts, as received from 3M. From the most active catalyst of these results, PtNi NSTF, PtNi nanotubes were created and are shown in chapter 7. This nanotube catalyst has the highest kinetic activity of any nanoparticle catalyst and even though they are of larger size, they have a higher mass activity than small carbon supported high surface area catalysts as well. Added to this increase in catalytic activity is the increased stability, which comes through the lack of carbon support (no support corrosion or particle dissolution) and larger particle size (lower particle agglomeration).

From chapters 3-7 it is clear that the increase in catalytic activity for the ORR comes with a reduced affinity for surface oxidation. This leads to the belief that the observed activity for these highly active catalysts is due to their ability to keep the surface clean from strongly adsorbed oxide-containing species.

The final chapter of this thesis gives an insight on the electrochemical behavior of Pt (100) in alkaline electrolyte. The pretreatment of this reactive surface is the key in the surface structure and the catalytic activity that it displays, just as the pretreatment of the nanoparticle catalysts in chapters 4 and 7 influences their structure and catalytic behavior as well. In contrast to acidic electrolyte, in alkaline media the surface state is more obvious from the adsorption processes that can be seen in the blank cyclic voltammetry. Furthermore, alkali-metal cations are shown to have a significant impact on both adsorption processes on Pt(100) and the catalytic activity for the oxidative stripping of adsorbed carbon monoxide.

Nedelandse Samenvatting

Het werk dat heeft geleid tot dit proefschrift is begonnen in Argonne National Laboratory, bij Chicago in Illinois, USA. In het laatste jaar van het traject is dit proefschrift tot stand gekomen aan de Universiteit Leiden.

Relevante processen zoals de zuurstofreductie en koolmonoxide elektro-oxidatie zijn bestudeerd en beschreven in dit proefschrift. Het doel van het onderzoek was de oorsprong van de katalytische activiteit van platina legeringen voor deze reacties te vinden en in het specifiek om deze kennis toe te passen in de ontwikkeling van nieuwe, aktieve katalysatoren voor de zuurstofreduktie. Om dit doel effectief te kunnen bereiken was het nodig om de betrouwbaarheid van de vergelijking tussen modelreacties met de roterende schijf elektrode (RDE) en *in situ* metingen met de brandstofcel (MEA) te verbeteren. Verbetering van de RDE methode kan zorgen voor snellere vergelijkende metingen tussen katalysatoren, hierbij effectief de ontwikkelingstijd voor nieuwe katalysatoren verminderend. Het resultaat is uiterst nuttig voor de ontwikkeling van brandstofcellen en het reduceren van ons aller afhankelijkheid van fossiele brandstoffen, terwijl ook de hoeveelheid schadelijke uitlaatgassen wordt ingeperkt.

Meerdere technieken zijn toegepast om aan deze doelen te kunnen voldoen. Allereerst zijn standaard elektrochemische methoden zoals cyclische voltammetrie (CV) en impedantie spectroscopie toegepast om adsorptie en reactie aan het oppervlak van de electrode, evenals de elektrolytweerstand te kunnen volgen. De zojuist genoemde RDE metingen maken het mogelijk om de invloed van diffusie op de metingen te verminderen, zodat de kinetische aktiviteit voor de zuurstofreductie kan worden bepaald voor de verschillende katalysatoren. Verder zijn er meerdere niet-elektrochemische technieken toegepast om de structuur van de katalysatoren te toetsen. Onder deze technieken bevinden zich *ex situ* elektronen microscopie, zoals scanning tunneling microscopie (STM), scanning elektronen microscopie (SEM) en transmissie elektronen microscopie (TEM). Vervolgens is hier elementen detectie aan toegevoegd door middel van high-angle annular dark field-scanning tunneling electron microscopy (HAADF-STEM) en energy dispersive X-ray scattering (EDX). Boviendien was ook Röntgendiffracte (XRD) toegepast om de nanodeeltjesgrootte, compositie en kristallijniteit te detecteren.

Tot besluit zijn er door meewerkende groepen theoretische berekeningen ingebracht om geobserveerde trends en experimentele uitkomsten te kunnen verklaren. Density functional theory (DFT) berekeningen zijn uitgevoerd door J. Greely in het centrum

voor nanomaterialen in ANL en Monte Carlo simulaties zijn gedaan door G. Wang in Purdue University.

Het proefschrift opent in hoofdstuk 2 met een uitgebreid onderzoek van een intrinsiek probleem bij het werken met een elektrisch geleidend elektrolyt: de elektrolytweerstand. Deze weerstand zorgt ervoor dat bij significante stromen de potentiaal van de elektrode verschilt van de potentiaal die door de potentiostaat wordt opgelegd; bijvoorbeeld wanneer de stroom hoog is door de opheffing van diffusie in een RDE meting. Verder wordt er in het hoofdstuk ingegaan op de invloed van adsorptieprocessen aan de elektrode gedurende de zuurstofreduktie, wederom een verschil in de meting ter vergelijking met het steady-state opereren van een MEA. Aangezien het compenseren voor weerstand en stroom ten gevolge van adsorptieprocessen relatief eenvoudig is, zal de RDE methode na toepassing van de juiste compensatie accurater zijn wanneer de verkregen data in de volgende hoofdstukken wordt vergeleken met MEA metingen in de literatuur.

De zuurstofreduktie aan platina bevattende nanodeeltjes is beschreven in de hoofdstukken 3 tot en met 7. Pt_3Co nanodeeltjes zijn gesynthetiseerd en gekarakteriseerd (hoofdstukken 3 en 4), uitgebreid rekening houdende met de pre-experimentele behandeling van de deeltjes en het effect hiervan op de deeltjesgrootte en activiteit voor de zuurstofreductie. Een “vulkaanvormige” afhankelijkheid is gevonden van massa activiteit ten opzichte van de deeltjesgrootte, dankzij de tegenovergestelde trends dat de kinetische activiteit stijgt met grotere deeltjes, maar de grootte van het oppervlak per massaeenheid tegelijkertijd daalt. De optimale deeltjesgrootte voor de vervaardigde Pt_3Co deeltjes is bepaald op ongeveer 4.5 nm.
Nieuwe kern-omhulsel (“core-shell”) deeltjes op een koolstof ondergrond zijn beschreven in hoofdstuk 5. Deze deeltjes hebben een kern van goud, terwijl het omhulsel bestaat uit een legering van Pt_3Fe. Niet alleen zijn deze deeltjes actiever voor de zuurstofreductie dan monometallisch platina, tevens zijn zij stabieler doordat zij minder snel agglomereren.
Nanogestructureerde dunne-film (NSTF) katalysatoren van 3M die niet op koolstof zijn gedragen worden beschreven in hoofdstukken 6 en 7. In hoofdstuk 6 wordt de bepaling van de optimale hoeveelheid van deze katalysator per eenheid oppervlakte van de schijfelektrode behandeld en de activiteit van de niet-behandelde NSTF katalysatoren zoals gekregen van 3M bepaald. Naar aanleiding van de resultaten hierin is gekozen om de meest actieve NSTF, PtNi, te behandelen en hier nanotubes

van te maken, welke beschreven worden in hoofdstuk 7. Deze nanotube katalysator heeft de hoogste kinetische activiteit van alle nanodeeltjes katalysatoren, en hoewel ze groter zijn en dus minder oppervlak per massaeenheid hebben, hebben ze zelfs een hogere massa-activiteit dan kleinere, koolstof-gedragen platina nanodeeltjes. Hieraan toegevoegd is de verbetering in stabiliteit door het ontbreken van de koolstof-drager (geen drager-corrosie of verlies van deeltjes) en grotere deeltjesgrootte (minder invlied van agglomeratie).
Uit hoofdstukken 3 tot 7 is duidelijk dat de verbetering van de activiteit voor de zuurstofreductie gepaard gaat met een kleinere affiniteit voor oppervlakte-oxidatie. Dit leidt tot de veronderstelling dat de hoge activiteit van de katalysatoren die in hoofdstukken 3 to 7 beschreven zijn, voortkomt uit de kracht die deze katalysatoren hebben om het oppervlakte verschoond te houden van sterk geadsorbeerde zuurstofhoudende deeltjes.

Het laatste hoofdstuk van dit proefschrift biedt een inzicht in het elektrochemisch gedrag van Pt(100) in alkalisch elektrolyt. De pre-experimentele behandeling van het krystal is van essentie voor de oppervlaktestructuur en katalytische aktiviteit die dit oppervlak toont, precies zoals de pre-experimentele behandeling van de nanodeeltjeskatalysatoren in hoofdstukken 4 en 7 ook hun structuur en katalytische activiteit beinvloed. In tegenstelling tot zuur elektrolyt is in alkalisch medium de staat van het oppervlak duidelijker zichtbaar in de voltammetry door de bijdrage van adroptieprocessen in de stroom. Bovendien is duidelijk dat het kation in het elektrolyt significant van invloed is op de adsorptieprocessen op Pt (100) en de katalytische activiteit voor de oxidatieve stripping van koolmonoxide van dit oppervlak.

List of Publications

Unique activity of ad-islands in the CO oxidation reaction, D.S. Strmcnik, D.V. Tripkovic, D. van der Vliet, K-C Chang, V. Komanicky, H. You, G. Karapetrov, J.P. Greeley, V.R. Stamenkovic and N.M. Markovič, J. Am. Chem. Soc., 130 (2008) 15332.

Adsorption of hydrogen on Pt(111) and Pt(100) surfaces and its role in the HOR, D. Strmcnik, D. Tripkovic, D. van der Vliet, V. Stamenkovic, N.M. Markovic, Electrochem. Comm., 10 (2008) 1602.

The role of anions in surface electrochemistry, D. Tripkovic, D. Strmcnik, D. van der Vliet, V. Stamenkovic, N.M. Markovic, Faraday Discuss., 140 (2008) 25.

The Role of Noncovalent Interactions in Electrocatalytic Fuel Cell Reactions on Pt, D. Strmcnik, K. Kodama, D. van der Vliet, J. Greeley, V. R. Stamenkovic and N. M. Markovic, Nature Chemistry, 1 (2009) 466.

Monodisperse Pt_3Co Nanoparticles as a Catalyst for the Oxygen Reduction Reaction: Size-Dependent Activity, C. Wang, D. van der Vliet, K-C Chang, H. You, D. Strmcnik, J.A. Schlueter, N. M. Markovic, and V.R. Stamenkovic, J. Phys. Chem. C., 113 (2009) 19365.

Novel Method for Fast Characterization of High-Surface-Area Electrocatalytic Materials Using a Carbon Fiber Microelectrode, D. Strmcnik, N. Hodnik, S. B. Hocevar, D. van der Vliet, M. Zorko, V.R. Stamenkovic, B. Pihlar and N.M. Markovic, J. Phys. Chem. C., 114 (2010) 2640

Monodisperse Pt_3Co nanoparticles as electrocatalysts: the effects of particle size and pretreatment on electrocatalytic reduction of oxygen, C. Wang, G. Wang, D. van der Vliet, K-C Chang, N. M. Markovic and V. R. Stamenkovic, Phys. Chem. Chem. Phys, 12 (2010) 6877

On the Importance of correcting for the uncompensated Ohmic resistance in model experiments of the Oxygen Reduction Reaction, D. van der Vliet, D. S. Strmcnik, C. Wang, V. R. Stamenkovic, N. M. Markovic and M. T. M. Koper, J. Electroanal. Chem., 647 (2010) 29.

Electrochemistry of Pt (100) in Alkaline Media: A Voltammetric Study, D. van der Vliet and M.T.M. Koper, accepted manuscript, Surf. Sci. (2010)

Curriculum Vitae

Dennis Franciscus van der Vliet was born in Tilburg, The Netherlands, on July 3rd 1981. From 1993 through 1999 he attended the Pauluslyceum, where he obtained his Atheneum diploma.

Starting in 1999, Dennis attended the Eindhoven University of Technology, graduating in 2005 and obtaining the degree of Master of Science in Chemical Engineering. In 2003 he was project leader of a multi-disciplinary project with 6 fellow students of different faculties under the supervision of Prof. Dr. Coehoorn and Dr. Willard of Phillips laboratories. His Master's project started in 2004 in the group of Dr. Marc T.M. Koper with the subject of Electrochemistry of Nitric Oxides on Palladium. Before formally graduating in 2006, Dennis performed his internship at Argonne National Lab near Chicago, IL, USA, where he had the opportunity to set up a new electrochemistry lab in the group led by Dr. Nenad Markovic.

Dennis' Ph.D. studies began in August of 2006 with the preordained plan to work in Dr. Markovic's group at Argonne National Lab for the first three years of his Ph.D., and to continue and finish in his last year in the group of Prof. Dr. Koper at Leiden University. The result of this cooperation between these research groups is presented in this Thesis. Parts of his work were presented at various international conferences.

Nawoord

Het promotieonderzoek is afgerond.
Als je het zo klinisch bekijkt doe je alleen geen recht aan de vier jaren van bloed zweet en tranen die het gekost heeft. Meestal was het een erg mooie tijd, want ik heb de kans gehad mijn creativiteit te benutten in het werk. Bovendien was ik in staat een stukje meer van de wereld te zien en vooral te beleven.

When Marc offered me the chance four years ago to start my Ph.D. studies with Nenad in Argonne, I regarded that as a unique opportunity to cooperate and learn from two people who are examples to me in this field. Furthermore, it would enable me to work with wonderful people such as Nenad and Voja, who are very helpful and appreciative; not just work related, but socially as well. I look back with pleasure at my time at Argonne, where Nenad and Voja always made me feel appreciated, and where the cooperation was excellent.

Na drie jaar te hebben doorgebracht in Argonne, ging ik terug naar Leiden voor het laatste jaar onderzoek aan de universiteit. Dit was een erg lastige situatie, want een jaar is een erg korte tijd om een volledig onderzoek te starten en af te ronden. Er waren nogal wat opstartproblemen, maar met Marcs rustige begeleiding en ondersteuning werd het al snel duidelijk dat er iets moois begon te groeien. De snelle en efficiënte feedback is wat ik misschien wel het meeste zal onthouden, het was erg prettig om op deze manier te werken aan mijn proefschrift. Ook de manier waarop Marc ervoor zorgde dat laat in mijn vierde jaar Stanley, Janneke en ik een presentatie mochten houden op de ICEI in Geneva, NY, was een knap staaltje. Ik kreeg in de jaren het gevoel van vertrouwen van Marc in mijn kwaliteiten en een goede afloop van dit hele traject. Leiding geven door zachtjes te sturen, in plaats van een richting opdragen, dat is de manier waarop Marc werkt en welke ik als bijzonder aangenaam heb ervaren.

Thank you Marc, Nenad and Voja, for an excellent and enjoyable cooperation which went beyond mere work. I can say strongly that I learned a lot from you and have grown due to your patient and pleasant guidance.

To the Argonne Bunch:
A big thank you as well to all of my colleagues over the years, without whom my thesis would never have been as it is now. Special thanks goes first of all to Dusan (both of you) for the early cooperation. I learned a lot from working with you initially, during the tough times of setting up a lab to work in. Chao, you were more than just a colleague, driving me around when my cars failed (as they did often in the year you were at Argonne). You helped me so much in the year we worked together and I know that without you this thesis would have looked rather different. Thank you for making the catalysts, and I am looking forward to working again with you very soon! Furthermore, a massive thank you goes to the Argonne Exchange Club people, as well as my Pool teams. You guys made the social life a good one for me, and created an atmosphere where I could unload and relax (usually). Hopefully see you again very soon.

Verder wordt een promotie niets zonder de geweldige steun van vrienden en familie. Allereerst mijn ouders, die mij altijd zijn blijven steunen, zelfs toen ze hoorden dat ik voor meerdere jaren in de Verenigde Staten zou gaan verblijven. Dank je wel pap en mam voor al die jaren die hiernaar toe hebben geleid, waarin jullie alle zorg van de randverschijnselen hebben weggehaald zodat ik me volledig met mijn studie kon bezighouden.
Opa, dank voor de geweldige steun die er altijd voor me was, ooms, tantes, neven en nichten, iedereen bedankt voor de mooie woorden en alle ondersteuning. Van je familie moet je het hebben, en ik prijs me gelukkig dat ik daar dus ook echt veel aan heb gehad. Francis, die er niet meer bij kan zijn om de ontknoping van mijn werk te zien; dank je wel voor alle lieve woorden, en ik heb het gelukspoppetje wat je me al die jaren geleden gaf nog steeds op mijn bureau staan.
Martijn en Jeroen, Sanne en Dorrith, jullie erg bedankt voor het blijven houden van het contact. Het was fijn om in het begin aan de andere kant van de oceaan nog vrienden te hebben om het over van alles en nog wat te hebben. Ik prijs mij erg gelukkig dat het contact met jullie nooit verwaterd is, maar misschien zelfs sterker is geworden dan het al was toen ik nog in Nederland woonde.

I am grateful as well to all my colleagues in the final year in Leiden: Stanley, Janneke, Matteo, Klaas Jan, Para, Steven, Alex, Youngkook, Ludo, Christine, Johan, Ben, Andrey, Björn, Yang, Dima, Gonzalo, Mar, Javi, Qin, José, Thijs, Arban. A significantly larger group than I had at Argonne. It was fun to discuss

science, but even better to talk with all of you about day-to-day stuff. Despite being short, the year in Leiden was made very pleasant by everyone.
Vervolgens een woord van dank aan mijn studenten van de afgelopen maanden. Anouk, Evelien, Corné en Marco, jullie hebben mij de ervaring gegeven om een leraar te zijn, wat niet altijd even eenvoudig ging. Dank jullie voor de geweldige inzet en interesse die jullie toonden in mijn werk.

Finally I would like to thank the most important person in my life for the past 3 years. Kiki, schatje, I owe you so much for being patient with me, supporting me in spirit and in word (thank you for helping me write better). The year we have to spend apart makes all things harder: the planning of our wedding, the apartment situation, furniture and cat. Thank you for taking most of those important things on yourself (and sorry for that) so I could focus on my thesis. Still, despite it being a less than happy year, you were always there for me. I love you and cannot wait to get back to you properly.

In four years you come across many people who contribute to your work. From a word of encouragement by a stranger who heard of my work, to a helpful act by a coworker whose work was unrelated to mine, to friends who helped me relax outside of work, all have helped to bring me to this point. I therefore would like to thank all those people, many of whom I do not have names of, for helping me get this far.

Het was een mooie tijd, maar ook een stressvolle vier jaar. Tijd voor wat rust.